An atomic clock for 10^{-18} timekeeping

by

N. Hinkley

B.S., Michigan Technological University, 2009

A thesis submitted to the

Faculty of the Graduate School of the

University of Colorado in partial fulfillment

of the requirements for the degree of

Doctor of Philosophy

Department of Physics

2016

This thesis entitled:
An atomic clock for 10^{-18} timekeeping
written by N. Hinkley
has been approved for the Department of Physics

_____

Dr. Ana Maria Rey

_____

Dr. Chris Oates

Date _____

The final copy of this thesis has been examined by the signatories, and we find that both the content and the form meet acceptable presentation standards of scholarly work in the above mentioned discipline.

Hinkley, N. (Ph.D., Physics)

An atomic clock for 10^{-18} timekeeping

Thesis directed by Dr. Ana Maria Rey

Oscillators used in timing standards aim to provide a universal, well defined frequency output with minimal random fluctuations. The stability (precision) of an oscillator is highlighted by its quality factor $Q = \nu_0/\delta\nu$, where ν_0 is the output frequency with a frequency linewidth of $\delta\nu$. To achieve a high timekeeping precision, an oscillator can operate at high frequency, allowing each partition of time, defined by one oscillation, to be short in duration and thus highly precise. In a similar fashion, because oscillator linewidth determines resolution of the output frequency, a narrow linewidth will yield a highly precise measure of time or frequency. High quality factors are advantageous for two reasons: i) frequency stability sets a fundamental limit to the consistency a clock can partition units of time and ii) measurement precision aids in the the study of physical effects that shift the clock frequency, leading to improved oscillator output control. In the pursuit of high quality factors, state-of-the-art microwave clocks match microwave oscillators to narrow atomic transitions achieving starting oscillator quality factors approaching $Q \sim 10^{10}$. Exploiting their starting quality factor in tandem with atomic transition properties allows microwave standards to reach a clock frequency uncertainty and precision of a few parts in 10^{16} after a month of averaging. Indeed, with this level of timekeeping, microwave clocks now define the SI second and play central roles in network synchronization, global positioning systems, and tests of fundamental physics.

Naturally, a direct approach to better timekeeping is forming oscillators with higher quality factors, partitioning time into finer intervals. This is realized in the next generation of atomic clocks, based on ultra-narrow *optical* transitions in an atom, capable of reaching quality factors of $Q > 4 \times 10^{15}$. Optical clock quality factors allow operation of frequency standards in a measurement regime unobtainable by microwave standards, promising orders of magnitude improvement in frequency metrology. This thesis describes the design and realization of an optical frequency standard based

on an ensemble of optically trapped, laser-cooled ^{171}Yb atoms. The frequency stability between two ^{171}Yb clock systems is presented here, demonstrating the first realized 10^{-18} level measurement precision reaching 1.6×10^{-18} after 25,000 s of averaging, a 100 fold improvement over state-of-the-art microwave sources. Leveraging a much improved measurement precision allows a detailed investigation of key physical phenomena that shift the atomic transition frequency. An in-depth study of these systematic shifts is discussed in detail here, with a focus on blackbody radiation shift and trap light induced frequency shifts. This study results in a total fractional uncertainty in the ytterbium clock transition frequency of 2.1×10^{-18}. Finally, the robust operation of ^{171}Yb clock systems at the 10^{-18} fractional level is discussed in detail here.

Dedication

To my son Edward Leo Hinkley

Acknowledgements

I would like to express my deepest gratitude to Chris Oates and Andrew Ludlow for taking me under their wing. During my time at NIST they have helped me cultivate a great affection for scientific study. I appreciate their dedication to promoting a laboratory environment that is both professional and educational.

To my colleagues Marco Schioppo, Jeff Sherman, Kyle Beloy, Roger Brown, Nate Phillips and Tai-Hyun Yoon. Thank you for fostering a complimentary and dedicated work environment. I will look back fondly on my time spent with each of you at NIST. I am particularly sentimental about our many conversations and your openness to my questions no matter how obtuse.

I have also enjoyed working with the new ytterbium researchers Will McGrew and Robbie Fasano, their enthusiasm is quite contagious. Many challenges lie ahead, but I am confident they will do a wonderful job. Last but not least, I'd like to thank my parents and my family for always encouraging my inner curiosity.

Contents

Chapter

Tables

Figures

Figure

Chapter 1

The Atomic Clock

Periodic physical systems are the basis we use to establish standards of time and frequency. Our unit of time, both conceptual and realized, provides the foundation for our base International System of Units and plays a central role in network synchronization, global positioning systems, and tests of fundamental physics. The next generation of timekeeping at 1 part in 10^{18} permits new timing applications in relativistic geodesy, enhanced Earth- and space-based navigation, telescopy, and new tests of physics beyond the Standard Model. This thesis details the experimental investigation and operation of two spin 1/2 ytterbium optical lattice clocks with timekeeping ability at the 10^{-18} level. This includes: i) A detailed description of the realized operation of a ytterbium optical lattice clock. ii) An experimental examination of optical clock noise characteristics and measurement precision. iii) A Careful study of all physical mechanisms responsible for systematic shifts of the clock frequency, with an emphasis on blackbody radiation and lattice light shifts.

1.1 Short history of timekeeping

Since antiquity we have incorporated the notion of time to order events in the past, present, and future, and exploited natural bodies to provide fully adequate timekeeping. The beginning of maritime travel represented the first widespread desire for ultra-precise and highly accurate man-made timekeepers [119]. Specifically, a ship's latitude could be obtained from angle referencing celestial objects; however, longitude required knowledge of local 'ship' time relative to starting location time [119]. To push the limits of chronography, clockmakers connected a robust periodic

mechanical oscillating mechanism to a counter, setting the ground work for timing instrument construction and the concept of clock performance. That is, the practical realization of a timing system must adequately divide time (be precise), it must order events into the past, present and future (be accurate) and it must perform the latter measurements promptly so they are of value. Oddly, transportation by sea is responsible for some of the best mechanical oscillators ever created.[1]

The conception of Quantum Mechanics at the onset of the 20th century provided the next great leap in timing innovation. Now the natural properties of atoms could be utilized in man-made timekeeping devices. Atomic transitions are beautifully suited for timekeeping: they "tick" at high and well-defined transition frequencies, they are isolatable, immune to environmental effects, and exist in abundant identical copies. By 1967 the second was redefined in terms of an energy oscillation in the cesium atom rather than the Earth's motion. The second is now: "the duration of $9,192,631,770$ periods of the radiation corresponding to the transition between the two hyperfine levels of the ground state of the caesium-133 atom"[91]. This definition exploits the fast cesium microwave transition oscillation ($\sim$9 billion times a second) and provides a highly precise measure of time or frequency. With over 50 years of development, microwave clocks have provided immense insight into the physical mechanisms that modify transition frequencies in cesium and cesium-like atoms. Uncertainties (accuracies) of state of the art cesium standards now reach a few parts in 10^{16} [53]. Derivatives of this effort include: Timekeeping and timing transfer at the 10^{-16} level, International Atomic Time (TAI), Coordinated Universal Time (UTC), direct verification of general relativity, GPS navigation, definition of geoid potential, the leap second, etc.[77, 78, 128, 25]

A natural progression to higher timekeeping performance is the use of higher frequency (optical) transition oscillators. Indeed the finer we divide time, the more precisely we can order events. Consequently, the invention of the laser in 1960 represents an important milestone shaping time-

---

[1] This was serious business as incorrect perception of ship location could mean life or death on an open body of water.

keeping today [110]. Still under development, laser technology in the visible spectrum is providing gains in frequency metrology, laser cooling, ultra-narrow atomic spectroscopy, quantum manipulation of atoms, and frequency comb metrology [107, 120, 65, 14, 137]. As optical technology matures, the next generation of timekeepers based on optical oscillators matched to atomic transitions will subdivide the second into quadrillions of pieces giving an even more precise measure of time. The ability for an optical clock to measure mHz shifts in its optical frequency or 1 part in 10^{18}, ushers in the next generation of timing, enabling new and exciting applications for precision measurements.

1.2   Oscillator measurement precision and accuracy

As described above, two qualities determine the nature of a frequency standard: timing accuracy and timing precision. The former results from a combination of systematic uncertainty (effects that alter the standard's periodicity from its natural, unperturbed state), and statistical uncertainty from repeated measures. The latter describes our ability to subdivide time set by oscillator instability or how the ticking fluctuates over a measurement period.[2] To illustrate these essential properties, imagine a pendulum clock. The periodicity of the pendulum swing provides the clock timebase. With ample measurements, the correct value of period or frequency is determined by the pendulum design, with deviations resulting from systematics (e.g., slow changes in temperature and air pressure which affect the pendulum clock). How the pendulum period or frequency changes over time limits the consistency we can partition units of time, setting the measurement precision.

Oscillator instability and uncertainty form a symbiotic relationship: we use instability to study systematic effects, and knowledge and control of systematic effects gives better oscillator instability. However, no time or frequency standard can make a timing measurement better than the statistical precision set by its instability. Further, the systematic uncertainty of an oscillator's frequency is often constrained by its long term instability. Therefore, although accuracy is essential for completely characterizing a frequency oscillator, the instability may be the most important (and

---

[2] This will also have a statistical uncertainty set by the measurement taken.

limiting) property of an atomic standard.

1.3   Optical atomic quantum oscillators

In the pursuit of exquisite timekeeping, we turn our attention to optical quantum oscillators, exploiting ultra-fast optical transition oscillations as a periodic pendulum. An optical atomic clock in its most basic sense is a local oscillator (laser) whose frequency is stabilized relative to an atomic transition, usually in a collection of neutral atoms or a single trapped ion. Ticking $\sim 10^5$ times faster than microwave systems, optical clocks divide the second into finer intervals, allowing a more precise measure of time. To illustrate this, we consider the starting stability (precision) of a frequency standard, given by the product of the resonance quality factor, Q, and the measurement signal-to-noise ratio (S/N). For an optical source, Q is determined by the transition frequency divided by the transition linewidth, typically 10^{14}. In many optical atomic clocks, the clock transition is detected using an electron shelving technique with a typical S/N of up to ~ 100. Therefore, with a single clock measurement (about 1 s) a fractional precision of 10^{-16} can be achieved; a level of precision reached by cesium microwave frequency standards only after a month of operation [53].

To enjoy the potential stability of a universal optical quantum oscillator we must account for all systematics that modify the natural transition frequency. Exploiting high optical measurement stability to characterize systematics can produce optical clocks with uncertainties superior to those of the best microwave atomic clocks. Of course, further reduction and control of a system's uncertainties will likely offer improved instability. Consequently, both oscillator stability and uncertainty play a role in realizing the true potential of a high frequency quantum oscillator, thereby unlocking measurements unobtainable by microwave standards: timekeeping at 10^{-18} and beyond.

1.4   Alkaline earth and alkaline earth-like atoms

Ideal quantum oscillators in an atomic clock would possess a means to achieve high S/N measure of an optical transition, easy quantum control, ultra-narrow atomic resonance (giving

a high Q value), and limited sensitivity to systematic effects. Fortunately alkaline earth and alkaline earth-like atoms, which are characterized by an atomic structure with two outer electrons, have these qualities freely provided by nature through the interaction of two valence electrons and internuclear structure. These atoms have ground state electrons in the S orbital and optical transitions to a low lying P orbital. The combination of two spin $1/2$ particles divides the electronic spin structure, S, into a singlet spin state (electronic spin configuration $S = 0$) and triplet spin states (electronic spin configuration $S = 1$). Considering only the dipole interactions, transitions would be forbidden between spin singlet and spin triplet states [116]. As a consequence, ^3P_j triplet manifold lifetimes can be extremely long (few thousand years), that is to say, they can posses a vanishingly narrow atomic transition linewidth (Q that is effectively infinity). However, beautiful atomic structure develops when these two electron systems are naturally or artificially perturbed from the ideal.[3]   In the perturbed case the ^3P_j manifold lifetimes become quenched, broadening their transition linewidths and shortening state lifetimes. This can produce a quantum system adaptable for collection, cooling, and spin-polarizing of atoms [101]. States with limited angular momentum grant reduced sensitivity to light field polarization effects [64]. Strong dipole transitions out of the $^1S_0$ ground state facilitate fast photon scattering for high S/N detection of long lived, ultra-narrow atomic transitions. The combined properties of alkaline earth and alkaline earth-like atoms provide quantum systems favorable for a high-performance clock: adaptability for the collection and isolation of atoms, high S/N detection, high but realistic Qs, and potentially low sensitivity to external environments.

1.5   Ytterbium characteristics

Ytterbium, an alkaline earth-like atom from the lanthanide series, offers seven stable isotopes from which one can select the perfect quantum oscillator specimen. Of particular interest is the fermionic isotope ^{171}Yb because it enjoys hyperfine interaction from its simple nuclear spin $(I = 1/2)$

---

[3] From LS coupling, a nonzero nuclear spin, and an external magnetic fields

and possesses the qualities described above for a high-performance clock [136]. The hyperfine interaction mixes a small amount of the $^1P_1$ and $^3P_1$ states into $^3P_0$. The result is an ultra-narrow, laser accessible, limited sensitivity, transition at 578 nm with a natural linewidth of $\Delta\nu \approx 10$ mHz. The hyperfine interaction with a $J=0 \rightarrow J=0$ states produces two energy levels, $\pm 1/2 m_F$ in the ground and excited sates with opposite magnetic sensitivity that can be averaged to eliminate first order magnetic effects shifting the clock frequency. Furthermore, the $^1S_0$-$^1P_1$ and $^1S_0$-$^3P_1$ transitions provide a way to cool and collect ^{171}Yb, first using the strong dipole transition at 399 nm ($\Delta\nu \approx 30$ MHz) and then the weaker intercombination transition at 556 nm ($\Delta\nu \approx 180$ kHz), respectively. Atomic population can be shuffled to one of the $m_F = \pm 1/2$ ground states by applying circularly polarized light, resonant with $^3P_1$. Additionally, because the $^1S_0$-$^1P_1$ transition has a fast scattering rate, it can be used for a high S/N detection of ground state atom population. Combined, the properties of ^{171}Yb make this atom an ideal optical quantum oscillator: high S/N detection, a high (but realistic) Q with limited magnetic sensitivity ($J=0$), straight forward laser cooling systems, and quantum control on the $^1S_0$-$^3P_1$ transition. Moreover, the ^3P_j manifold transitions are easily accessible with robust laser systems, advantageous for continuous clock operation. An energy level diagram and relevant electronic states of ^{171}Yb are given in Figure 1.1.

1.6   Interrogation of free space atoms

To this point we have only considered ideal quantum oscillators free from motion. However, in nature a collection of gaseous atoms will have a characteristic temperature, with a corresponding velocity distribution given by the Maxwell-Boltzmann law. Additionally, a single atom moving in a laser field will experience a detuned field frequency relative to an atom at rest of

$$\omega = \omega_0 \left(1 \mp \frac{v}{c}\right) \qquad (1.1)$$
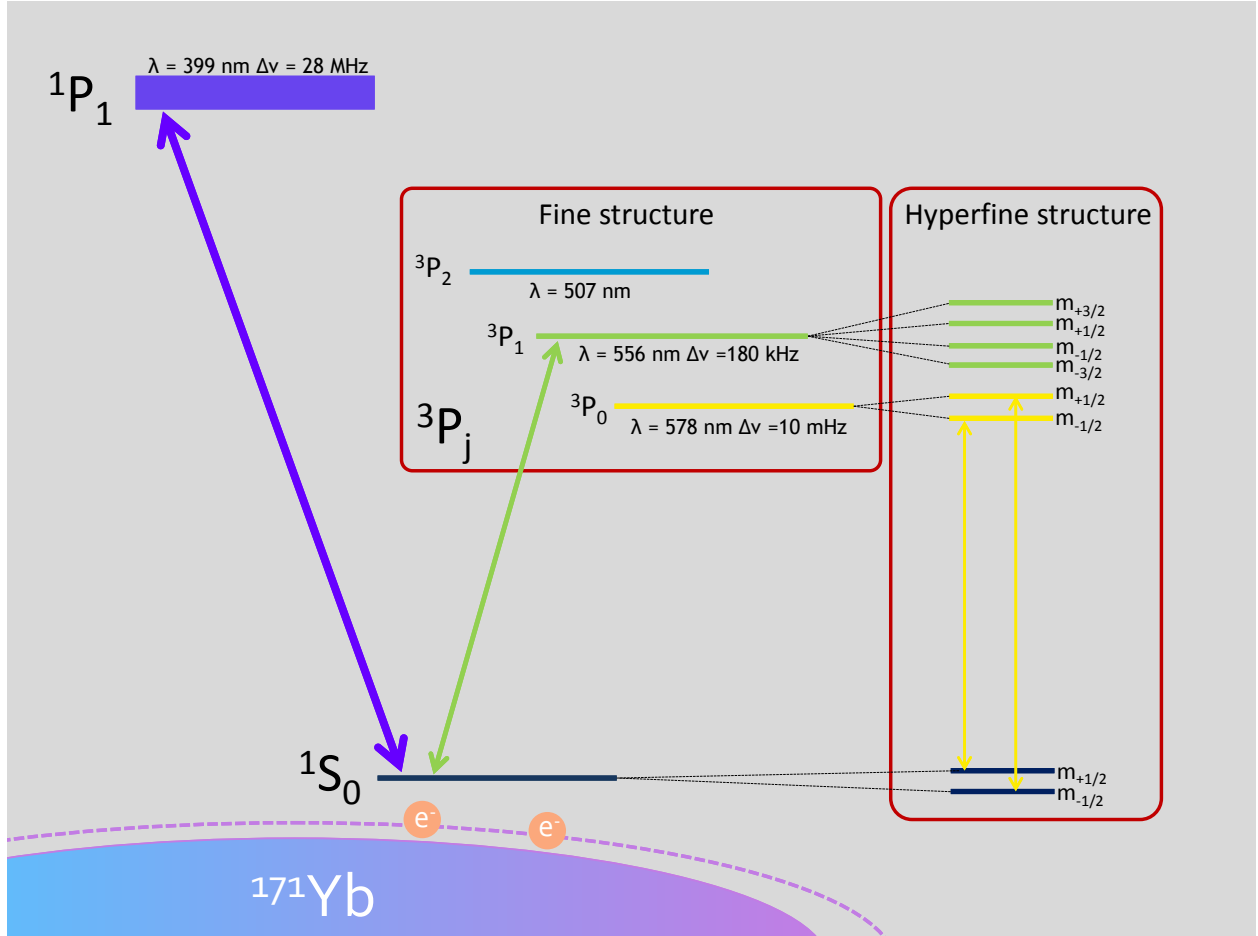
Figure 1.1: Relevant Yb atomic energy levels and transitions, including laser cooling transitions (399 and 556 nm), and the clock transition (578 nm). Resonant 556 nm circularly polarized light moves atomic population to one of the ground m_F states through the $^3P_1$ hyperfine manifold, spin polarizing the atomic sample. The two clock transitions are averaged, exploiting opposite magnetic sensitivity of $m_F = +1/2$ vs. $m_F = -1/2$. $^1P_1$ provides a closed, fast, cycling transition for high S/N detection of ground state occupation.

8

where v is the velocity component parallel to the source, ω is the transition frequency (in radians per second), and c is the speed of light [23].[4] This phenomenon is commonly known as the Doppler effect. At finite temperature, T, our collection of clock atoms will have a Gaussian distribution of velocities with a cumulative effect of broadening a transition spectrum beyond the natural linewidth, with full width at half maximum (FWHM) of

$$\Delta\nu_{FWHM} = \sqrt{\frac{8k_B T \ln(2)}{mc^2}}\nu_0 \tag{1.3}$$

where k_B is Boltzmann's constant, ν_0 is the natural transition frequency (in Hz), and m is the mass of the atom [23]. Consequently, the Doppler width of our clock transition at room temperature is $\sim$488 MHz or 9.5×10^{-7} in fractional frequency ($\Delta\nu/\nu_0$). Indeed the most direct way to limit $\Delta\nu_{FWHM}$ is reducing the gas temperature. Commonly this is done via Doppler cooling, where red detuned lasers cool the atomic sample by exploiting the presence of a Doppler shift to preferentially absorb a photon momentum opposite the motion of an atom [30, 97]. Excited atoms spontaneously decay, re-emitting photons in all directions, resulting in net kinetic energy removal from the ytterbium gas, lowering its characteristic temperature. As this process requires the repeated preferential photon absorption (cooling) followed by re-emission in all directions (heating), atom-photon momentum exchange reaches thermal equilibrium with final atomic temperature on the order of

$$T_{Doppler} = \frac{\hbar}{2}\frac{\Gamma}{k_B}. \tag{1.4}$$

where Γ is the natural linewidth of the resonance (in radians per second) [86]. In our ytterbium system we cool atoms on the $^1S_0$-$^3P_1$ intercombination transition at 556 nm, with a linewidth of ~ 180 kHz, reaching temperatures of several micro-Kelvin. Assuming a final atomic temperature

---

[4] This Doppler shift equation is only accurate to first order in v/c. Expanding the relativistic Doppler formula as a power series in v/c will give

$$\omega = \omega_0\left(\mp\frac{v}{c} + \frac{1}{2}\frac{v^2}{c^2}\cdots\right) \tag{1.2}$$

where the linear term is the first order Doppler effect and the quadratic term yields the second order Doppler effect. See chapter 6 for more details.

of 6 μK, the Doppler broadening is limited to $\sim$70 kHz or 1.3×10^{-10} fractionally, some 8 orders of magnitude above our desired level of performance.

Finally, even considering an ideal case of a single photon absorbed by a stationary atom, conservation of momentum and energy requires the atom to recoil, shifting the perceived transition frequency. Although this recoil energy is small, it has the consequence of an emitted photon (from a stationary atom) having incorrect energy for absorption for the exact same transition by another identical motionless atom. If our clock uncertainty was limited by the recoil energy of the emitted photon,

$$\Delta\nu_{recoil} = \frac{h}{2m\lambda^2},$$ (1.5)

that would correspond to a linewidth of $\sim$3.5 kHz or 6.7×10^{-12} fractionally. Consequently, Doppler-free, and recoil free techniques are required if performance reaching microwave standards and beyond is desired.

1.7   Spectroscopy of ultra-narrow optical transitions at the Hz level

An atom interrogated in free-space requires the conservation of both energy and momentum giving rise to recoil and Doppler effects. However, a quantum oscillator confined to a dimension less than a transition wavelength (known as the Lamb-Dicke regime) experiences no Doppler or recoil shifts, rather, its motional characteristics are dictated by the trapping potential [36]. We can explain this behavior semi-classically by considering an atom confined to a quantum harmonic potential, submerged in a large (relative to harmonic confinement) electromagnetic wave. As the atom oscillates within the trap, it experiences a corresponding phase oscillation of the electromagnetic wave at the trap frequency. Because the phase oscillation amplitude is $< 2\pi$ and sinusoidal, the atom enjoys a time averaged atomic velocity of zero, with sideband features at the motional frequency. Additionally, in the limit of tight atomic confinement in the harmonic potential, the recoil shift is absent as well because the net momentum change relative to the trapping energy is minimal. The light momentum is not lost, but simply transfers to the atom-harmonic potential

'structure' with minimal system momentum change.

To eliminate Doppler related broadening using the Lamb-Dicke suppression, we engineer an off resonant, conservative dipole light trap, or optical lattice, spatially confining our ytterbium atoms in a harmonic oscillator-like potential. The extent of confinement is quantified by the Lamb-Dicke parameter, η, which gives the relative spacial confinement of the atomic wave function, Δx, to the clock transition laser wavelength,

$$\eta \equiv k\Delta x = k\sqrt{\frac{\hbar}{2m\omega_0}} = \sqrt{\frac{\omega_r}{\omega_0}} \tag{1.6}$$

where ω_0 is vibrational frequency of the harmonic potential, and ω_r is the recoil shift (in radians per second). Operating in the Lamb-Dicke regime ($\eta \ll 1$), we can make two types of transitions: carrier transitions where the internal quantum state changes but not the atomic motion and sideband transitions when the atomic motional state is changed along with its quantum state. The Hamiltonian of the combined atom- and quantum harmonic oscillator- system interacting with a electromagnetic plane wave has solutions to the time-dependent Schrodinger equation analogous to the Rabi flopping solution of a two level system. The Rabi flopping frequencies between ground and excited states in motional state, n, can be expressed as [134, 72]:

$$\begin{aligned} \Omega_{n,n-1} &\cong \eta\sqrt{n}\Omega_0 \\ \Omega_{n,n} &\cong \Omega_0 \\ \Omega_{n,n+1} &\cong \eta\sqrt{n+1}\Omega_0 \end{aligned} \tag{1.7}$$

where $\Omega_{n,n-1}$, $\Omega_{n,n}$, and $\Omega_{n,n+1}$ are the Rabi rates for the first order red sideband, carrier, and first order blue sideband respectively, and Ω_0 is the Rabi flopping frequency of the atom-electromagnetic wave interaction. The relative strength of sideband transitions to the carrier is proportional to η^2, consequently as $\eta \to 0$, red and blue sideband intensities become greatly reduced [72]. This has added effects of suppressing sideband line pulling of the (natural) carrier frequency and promoting homogenous excitation of the clock transition in large atomic populations as the dominant Rabi rate, $\Omega_{n,n}$, remains independent from motional state occupation.

The optical lattice is generated by interfering counter-propagating laser beams of the same frequency that result in an optical standing wave with periodic electric field potentials every $\lambda/2$. Using a Gaussian beam, counter-propagating wave interference creates a spatially periodic array of 2-D pancake shaped potentials, confined radially by the Gaussian parameters. Atom trapping is a consequence of the atomic electronic polarizability interacting with the spatial gradients of the electric field. Additional laser beam interference can create multi-dimensional (1-D, 2-D and 3-D) confinement of arbitrary construction. Ultimately we can adjust four components when engineering an optical lattice: laser frequency, polarization, electric field intensity (potential depth), and optical wave interference via laser alignment.

Aligning the clock interrogation laser along the direction of tight lattice confinement eliminates Doppler and motional effects while probing the ultra-narrowband electronic 'clock' transition. With the clock transition well resolved, we match our optical local oscillator to the atomic frequency, creating our clock timebase. Although the optical lattice induces a Stark shift on the atoms' electronic states, the net effect can be nearly canceled by operation at the so-called 'magic' wavelength, λ_m, where both electronic states of the clock transition are shifted equally [64]. A key advantage of the optical lattice is that many (10^3 to 10^6) atoms are isolated and confined in the lattice potential. All of these atoms are interrogated simultaneously, thereby improving the atomic detection signal-to-noise and thus the instability beyond that of a single quantum oscillator. Assuming a starting ytterbium transition of ~ 1 Hz, and a S/N of 100, we find our beginning fractional measurement precision at 1 s to (theoretically) be $\sim 2\times10^{-17}$,[5] where atomic noise properties allow enhancement of measurement precision via averaging of frequency information. As lattice clocks combine high S/N with an ultra-narrow optical transition, many have anticipated these clocks realizing the goal of 10^{-18} fractional time and frequency measurement precision and accuracy.

---

[5] See Chapter 3 for more detail. At the time of this writing, clock performance at this level has yet to be achieved for times < 10 s.

1.8   Applications of atomic clocks at the 10^{-18} level

A measurement at 1 part in 10^{18} is equivalent to specifying the age of the known universe to a precision of less than one second or Earth's diameter to less than the width of an atom. To illustrate the power of this measurement capability, we first consider the gravitational redshift, a consequence of general relativity dictating that clocks 'tick' more slowly in gravitational fields. This phenomenon has long been accounted for when remotely comparing atomic clocks with gravitational elevations differing by many meters or km. A clock measurement at the 10^{-18} fractional level can be used to resolve spatial and temporal fluctuations in Earth's gravitational field equivalent to 1 cm of elevation, offering a new tool for geodesy, hydrology, geology, or perhaps even climate change studies [112, 29, 66, 113]. Space-based implementations can probe alternative gravitational theories, e.g., by measuring red-shift deviations from general relativity with a precision that is three orders of magnitude higher than the present level [113]. Additionally, although present-day temporal and spatial variation of fundamental constants is known to be small, 10^{-18}-level clock measurements offer up to two orders of magnitude tighter constraint on these variations, the theories predicting them, and may provide insight into dark mater [43]. Finally, timekeeping improvements directly benefit navigation systems, telescope array synchronization (e.g., very-long-baseline interferometry), secure communication, quantum control of atomic systems, interferometry, and likely lead to redefining the SI second [68, 15, 43].

1.9   Thesis overview and perspective

With the realization of the first optical clocks around 2000, there was great excitement over the potential high strides atomic clocks were poised to make. One of the first optical clock proposals, even speculated that with a continued effort, frequency metrology at 1 part in 10^{18} could be possible [64]. In a field where historically $\sqrt{2}$ improvement was an immense achievement, we now where faced with opportunities to advance our timekeeping abilities by 100x, 1000x, or more. Indeed, over

the past 15 years, such strides have been realized, with each milestone opening new applications and measurement possibilities. In this thesis I describe the first experimental realization of atomic clocks operating at the proposed 10^{-18} level. These results require the understanding and control of multiple key physical effects, which will be described in detail here. As a result, we demonstrate clocks that not only reached 10^{-18} in terms of fractional frequency measurement precision but also in terms of uncertainty relative to the natural ytterbium 'clock' transition frequency.

The experiments done to complete this study used two complex apparatus, each formally referred to here as a 'ytterbium optical lattice clock'. The complete study was a result of a dedicated research team effort, however, I was involved in virtually all aspects of the measurements performed here. In particular, my efforts focused on the ytterbium apparatuses, primarily the first ytterbium system, which I operated independently for multiple years. Our goal as a team was simple: demonstrate the best measurement performance possible, then use this capability to study physical effects altering the natural ytterbium clock transition. My efforts originally concentrated on the construction and stabilization of laser systems used to control and manipulate ytterbium atoms. In parallel I began working with Jeff Sherman, Nathan Lemke, and Andrew Ludlow on measuring the differential static polarizability of the ytterbium clock transition (Chapter 4). We continued our efforts with Kyle Beloy to measure the dynamic correction factor needed to describe blackbody radiation interaction with ytterbium. At this time, Jeff, Andrew, Nathan, and I worked on construction of a second ytterbium system. After completing the second ytterbium clock apparatus we began investigations of our measurement performance. This resulted in the first demonstration of atomic clocks operating at the 10^{-18} level, and my first author publication of our stability result in Science in 2013 [55].

After this effort I continued to work with Andrew Ludlow and Kyle Beloy on the construction of a blackbody radiation shield as we preceded with the second part of our group goal. With the help of Nate Phillips running the second ytterbium system we directly observed a blackbody radiation shift in our ytterbium clock. After a long, and dedicated effort, we completed our study of the

blackbody radiation shift at the 10^{-18} fractional level (Chapter 4 of this thesis) and resulted in my second author publication in Physical Review Letters.

Then I started to work with Nate Phillips on the first lattice light shift measurements on the second ytterbium clock system (Chapter 5). Work progressed to a point where lattice light shift measurements could continue with a single system, and I began to measure other systematics on the first ytterbium system. At this time, a visiting professor from University of Korea, Tai-Hyun Yoon, spent a sabbatical year working in our group. With my lead, Tai and I measured a host of systematic effects for the ytterbium optical lattice clock (Chapter 6), notably the DC stark shift and Zeeman shift (joined later by Will McGrew on the Zeeman measurements). At this time, a postdoc, Marco Schioppo, was making improvements to the clock laser. Marco Schioppo, Will McGrew, and I continued to study Doppler related light shifts, and phase chirps that can develop from delivering stabilized clock light to the ytterbium atoms.

Parallel to this investigation, I began forming a new lattice laser system to be used by both ytterbium apparatus. This included providing an interface with the existing second ytterbium lattice system, and constructing a new optical system around the first ytterbium apparatus to accommodate trapping ytterbium in a vertically oriented lattice with density shifts in the 10^{-18} level, able to be characterized to the 10^{-19} level. This began our efforts to quantify lattice light shifts for different lattice sources on both ytterbium systems, and complete the study of lattice light shifts, an effort headed by a postdoc Roger Brown. With Marco Schioppo's dedicated efforts on the clock laser, combined efforts to characterize clock derived systematic shifts, and my vertically oriented lattice that could transfer stabilized clock light to the atom reference frame, our group demonstrated a clock construction with near elimination of Dick noise using Ramsey spectroscopy, with a potential, four clock stability of $6 \times 10^{-17}/\sqrt{\tau}$ with τ in seconds of averaging [114]. My final work involved a second investigation of the background gas shift headed by Will McGrew. We investigated two atomic background gasses (ytterbium and hydrogen) and the measurement and control of these shifts at the 10^{-19} level. This completed the last systematic study needed for 10^{-18}

level clock uncertainty relative to the natural ytterbium 'clock' transition frequency.

<center>Chapter 2</center>

<center>Experimental Operation of the NIST Ytterbium Clock</center>

Ytterbium is a metallic element with a bulk property appearance similar to the mineral iron pyrite, more commonly known as fool's gold. Realization of an atomic clock based on this quantum oscillator requires performing high resolution spectroscopy on a single isotope of ytterbium and matching the frequency of an optical local oscillator to its electronic resonance. Here we detail the procedure transforming metallic ytterbium to an optical frequency timekeeper. This includes the trapping of ^{171}Yb, formation of a specially designed optical lattice, constructing a high quality local oscillator for spectroscopy on the $^1S_0$-$^3P_0$ clock transition, and a control system linking each clock component for autonomous operation.

2.1   Laser cooling and trapping of ytterbium atoms

Our two clock apparatus, referred to here as Yb-1 and Yb-2, independently heat a solid nugget of ytterbium in an effusive Knudsen cell (atomic oven) housed in a high vacuum (10^{-7} Torr) enclosure. When heated (~ 800 K) the oven produces a thermal beam of ytterbium atoms that propagates along the axis of the vacuum chamber through a differential pumping area to a separate ultra-high vacuum (10^{-9} Torr) section constructed to have optical axis for laser cooling and trapping. In the ultra-high vacuum section, Yb-1 and Yb-2 cool and collect 10 - 50 million ^{171}Yb atoms from the thermal beam utilizing the strong, closed $^1S_0$-$^1P_1$ dipole-allowed transition at 399 nm. First, a counter-propagating 10 mW, 399 nm, laser beam detuned ~ 120 MHz below

resonance slows ^{171}Yb atoms from the thermal beam as they approach the trapping volume.[1] Then, the slowed atoms are confined and laser-cooled in a blue magneto optical trap (MOT) consisting of three nearly-orthogonal, retro-reflected 1 mW, 399 nm beams detuned 15 MHz below resonance and a magnetic field gradient of ~ 3 mT/cm, generated by a pair of anti-Helmholtz coils [104]. The fast decay rate of the $^1S_0$-$^1P_1$ transition ultimately limits the temperature of the 399 nm MOT to ~ 1 mK from random photon scattering. Trap loading times can rage from 30 ms to 1 s depending on desired MOT population.

A second stage of laser cooling using the weaker $^1S_0$-$^3P_1$ intercombination transition at 556 nm forms a green MOT, which further reduces the atomic temperature to the μK level. We step the magnetic field gradient and apply increasingly resonant 556 nm light in three stages to efficiently transfer atoms from the blue MOT into the green MOT, while preparing the atomic sample for the lattice. Typical transfer efficiencies from 399 nm MOT to 556 nm MOT are $> 90\%$, largely dependent on initial green MOT parameters. The first stage of green MOT cooling, initiated during the blue MOT, applies 300 μW of 556 nm laser light red detuned by 2 MHz for $\sim$17 ms after the blue MOT cooling. In the second stage we step the 556 nm frequency closer to resonance by 1 MHz, doubling the first stage green MOT field gradient to ~ 2 mT/cm, which compresses the atomic cloud and ensures a better overlap with the optical lattice potential. Third-stage green MOT detuning and optical power are reduced to $<$500 kHz and $<$30 μW respectively, both tuned to regulate the final atomic atom number, and temperature between 4-25 μK, with a minimum largely defined by the Doppler-cooling limit. Second- and third-stage green MOT cooling times last 20 ms and up to 50 ms respectively, depending on desired ensemble temperature. At the tens of μK level, our final atomic sample of several million ytterbium atoms is sufficiently cold to be trapped in our lattice potential.

---

[1] No Zeeman slower is employed

2.2   The optical lattice

The lattice light trap is an electromagnetic standing wave formed by interfering two counter propagating laser beams, generally of the same frequency and polarization. The lattice wavelength is fixed at $\lambda_m \sim 759$ nm where the $^1S_0$ and $^3P_0$ states in ytterbium have equal Stark shifts [73]. We employ a red-detuned lattice where the polarizability of ^{171}Yb enables dipole traps in areas of high laser field intensity.[2] In this way, atoms are localized to a volume less then a transition wavelength and normally large ac-Stark shifts cancel, preserving the natural $^1S_0$ to $^3P_0$ transition frequency. Consequently, special attention is given to lattice characteristics (spectral purity, frequency, formed dipole trap...) so this potentially highly perturbative effect can be well controlled.

2.2.1   Lattice light source

The optical lattice potential must be sufficiently deep to trap atom ensemble temperatures determined by the final green MOT. Additionally, high spectral purity is required for exactly matching the ac-Stark shifts of $^1S_0$ and $^3P_0$. Fortunately the common Titanium Sapphire laser (Ti:S) offers excellent power and spectral purity at the desired lattice wavelength λ_m. Each Yb system's lattice is derived from a distinct (Ti:S) laser; one is built with all intracavity elements tuned to operate at 759 nm (Yb-1), and the other is injection locked by an external cavity diode laser near 759 nm (Yb-2). Power output can range from 2 W-5 W depending on operation parameters with a typical line-width of 50 kHz. The Ti:S output power spectrum is further filtered by an interference Bragg grating ($\Delta\lambda = 0.05$ nm) eliminating amplified spontaneous emission away from λ_m. For additional frequency stabilization, a small fraction of the output from ether lattice system can be sent via polarization-maintaining (PM) optical fiber to a reference optical cavity, fixing the lattice frequency.[3] Feedback to an intra-cavity piezoelectric transducer (PZT) stabilizes the Ti:S

---

[2] $^1S_0$ and $^3P_0$ Stark shift can be matched in a blue-detuned lattice where atoms are trapped in regions of low electric field intensity

[3] Reference cavity drift is ≤ 100 kHz/day

lattice laser frequency to a reference cavity resonance.[4] A small fraction of lattice light is sent to a frequency comb for an absolute frequency measurement.

2.2.2   Lattice frequency, amplitude, and polarization control

Each Ti:S output is frequency controlled by a unique acousto-optic modulator (AOM) that shifts its respective output laser frequency to 394,798,271.1(5) MHz for confinement of ytterbium atoms near λ_m. The laser frequency difference between the Ti:S of Yb-1 and that of Yb-2 can be directly detected in a heterodyne optical interferometer. This heterodyne beat is stabilized to 162 MHz using an radio frequency (RF) delay line interferometer, with Yb-1's laser frequency chosen higher than that of Yb-2. An AOM downshifts Yb-1's laser frequency by 82 MHz, where another AOM upshifts Yb-2's frequency by 80.0 MHz, ultimately leading both to 394,798,271.1(5) MHz, before the light is sent via PM fiber to the atomic systems. We efficiently transfer up to $\sim$2 W of optical power to the vacuum system for our lattice configurations. Feedback to AOM RF power is used to intensity stabilize light delivered from each lattice system. For additional intensity control at higher bandwidth, we employ an electro-optic amplitude modulator. A polarization cube assures pure linear lattice polarization before the vacuum chamber. Additional $\lambda/2$, $\lambda/4$ waveplates following the polarization cube are tuned to minimize birefringence induced ellipticity from fused silica vacuum viewports.

2.2.3   Optical lattice potential

Yb-1 and Yb-2 are designed to accommodate multiple lattice configurations. We adopt two techniques that generate lattice standing waves: a simple retro-reflected lattice beam, and an optical buildup cavity. For the retro-reflection technique, incoming light is focused and retro-reflected from the opposite side of the vacuum chamber and mode-matched to the incoming beam, thereby forming trap at the focus. Alternatively, we generate standing waves by locking the lattice

---

[4] Lattice frequency control at the MHz level is routine.

laser output to an optical buildup cavity overlapped with our green MOT atoms. The enhancement cavity exploits lattice power buildup to form a large lattice mode volume providing greater transfer efficiency (higher atom number) from the green MOT while limiting atom-atom interaction effects and allows for deep trap depths.

Both Yb-1 and Yb-2 enjoy a horizontally-oriented retro-reflected lattice. In this simple and robust technique, 500 mW to 1 W of laser power is focused to 60 μm ($1/e^2$ intensity diameter) allowing for trap depths of ~600 E_r, routinely trapping 25,000 atoms. (recoil energy $E_r/k_B = 100$ nK) In later experiments, Yb-1 employed a retro-reflection lattice with different lattice parameters in the vertical direction. This vertical lattice possesses 400 mW to 2 W focused to 120 μm ($1/e^2$ intensity diameter) for trap depths of ~ 400 E_r, regularly trapping 100,000 atoms. Yb-2 employs an optical buildup cavity in the vertical direction by locking ~ 200 mW of laser power into a Fabry-Perot buildup cavity by means of the Pound-Drever-Hall (PDH) technique [37]. The lattice enhancement cavity has a finesse ~ 200, which increases the lattice power by ~ 70x and allows trap depths of ~ 2000 E_r for a focus of 320 μm. With this large trap mode volume, the Yb-2 vertical lattice routinely traps ~ 1 million or more ytterbium atoms. Light transmitted through the cavity is intensity stabilized, preventing heating of atoms from amplitude fluctuations. In general, vertical lattice potential configurations also include potential energy differences between lattice sites due to the presence of Earth's gravitational field.[5] The above lattice configurations allow trapped atoms to range in number from several hundred to 1 million depending on final atomic temperature and original blue MOT population.

2.3   Optical local oscillator

To approach the natural Q factor of the ytterbium clock transition, it is necessary to provide additional stabilization of the stable laser source used as the optical local oscillator (LO) before performing spectroscopy on the lattice trapped atoms. Standard practice is to pre-stabilize the clock

---

[5] see Chapter 5

laser to an isolated, high-finesse Fabry-Perot interferometer (optical cavity), thereby transforming the problem of *frequency* stability to one of *length* stability. Current state-of-the-art optical cavity performance achieves a length stability limited by thermal mechanical fluctuations of the mirror surfaces corresponding to a thermal noise floor limited fractional frequency of $\sim 1 \times 10^{-16}$ [90, 130, 61].[6] A well-designed optical cavity will have well defined and fixed frequency resonances (high finesse, high S/N, and limited length deviations), and be insensitive to the outside environment (temperature, vibrations, electronic noise etc.). Current state-of-the-art optical clocks are still limited by optical cavity noise, with notable performance advances resulting from more advanced and higher performing optical cavities [62, 55, 89, 50, 4].

Our local oscillator starts as a tapered amplified quantum dot laser operating at 1156 nm with a free running linewidth of 30 kHz. Using the PDH technique, we servo-lock its frequency to a resonating mode of an isolated high-finesse, Fabry-Perot optical cavity to reduce the clock laser linewidth from 30 kHz to $\leq$ 100 mHz for ultra-high resolution spectroscopy [37, 61]. To control the thermal expansion (i.e. the frequency) we chose ultra-low expansion (ULE) glass as the cavity spacer material with a thermal expansion zero crossing slightly elevated from room temperature. To minimize and control the linear drift of the ULE spacer, we use a passive thermal isolation system. The cavity is housed in box shaped vacuum enclose at $\sim 10^{-8}$ Torr. Inside of the vacuum there are 3 nested layers of box shaped polished aluminum radiation shields providing passive thermal isolation. The vacuum enclosure has an estimated thermal time constant of 4 days, providing 7 orders of magnitude thermal low-pass attenuation to 1 h time-scale temperature fluctuations. To regulate the external vacuum enclosure surface temperature, there are 6 in-loop and 6 out-of-loop thermistors (1 for each side) with corresponding resistive heaters. The temperature is set slightly elevated from room temperature and servo-locked to the thermal expansion zero crossing of the ULE cavity spacer. Five additional layers of silica aerogel cover the heater elements to provide thermal insulation, decoupling the temperature servo control from the surrounding environment.

---

[6] For perspective, usual length fluctuations in high performance optical cavities are less than the width of an atom.

After ensuring stable temperature operation at the thermal expansion zero crossing, we implement a vibration insensitive cavity construction [130, 129]. Acceleration induced deformation of the ULE along the direction of gravity is reduced by suspending the cavity about points where outer cavity mass slump matches inner cavity suspension contraction, preserving net cavity length. Resting the cavity on four hemispherical Viton supports placed symmetrically about the cavity center of mass reduces vibration insensitivity in the horizontal plane [130, 129]. With the optical cavity now insensitive to both temperature fluctuations and mechanical vibrations we can reach the fundamental Brownian thermal noise limit. To push the Brownian limit we employ several room temperature strategies: (1) long ULE cavity (30 cm), (2) large beam size to average thermal mechanical fluctuations of the mirror surfaces, and (3) mirror coatings and mirror substrates with high mechanical quality factors [61, 50]. We also obtain several advantages from operating in the near-infrared including low-loss dielectric mirrors, a more convenient wavelength for interfacing with frequency combs, and the potential use of crystalline mirror coatings. The stabilized 1156 nm light is sent to a periodically polled lithium niobate (PPLN) waveguide crystal that produces 20 mW of 578 nm light via second harmonic generation with a conversion efficiency of $\sim 20\%$ at a phase matching temperature of ~ 36.4 C. Optical elements used in the clock laser system are held on a breadboard suspended on an actively canceled vibration isolation platform providing 30-40 dB of isolation from noise ranging 5 Hz-100 Hz. The 578 nm light is distributed to Yb1 and Yb2 through fiber-noise-canceled optical fibers, and matched to $^1S_0$-$^3P_0$ clock transition by independently controlled AOMs. (See the Chapter 6 section of 'Doppler shift, 1st and 2nd order' for more detail)

2.4   Spectroscopy of the ytterbium clock transition

In the lattice, the ytterbium atoms are confined to the sub-wavelength level (also known as the Lamb-Dicke regime), thereby eliminating Doppler effects in the direction of the clock laser propagation, allowing high resolution spectroscopy of the ultra-narrow $^3P_0$ triplet transition. Atoms
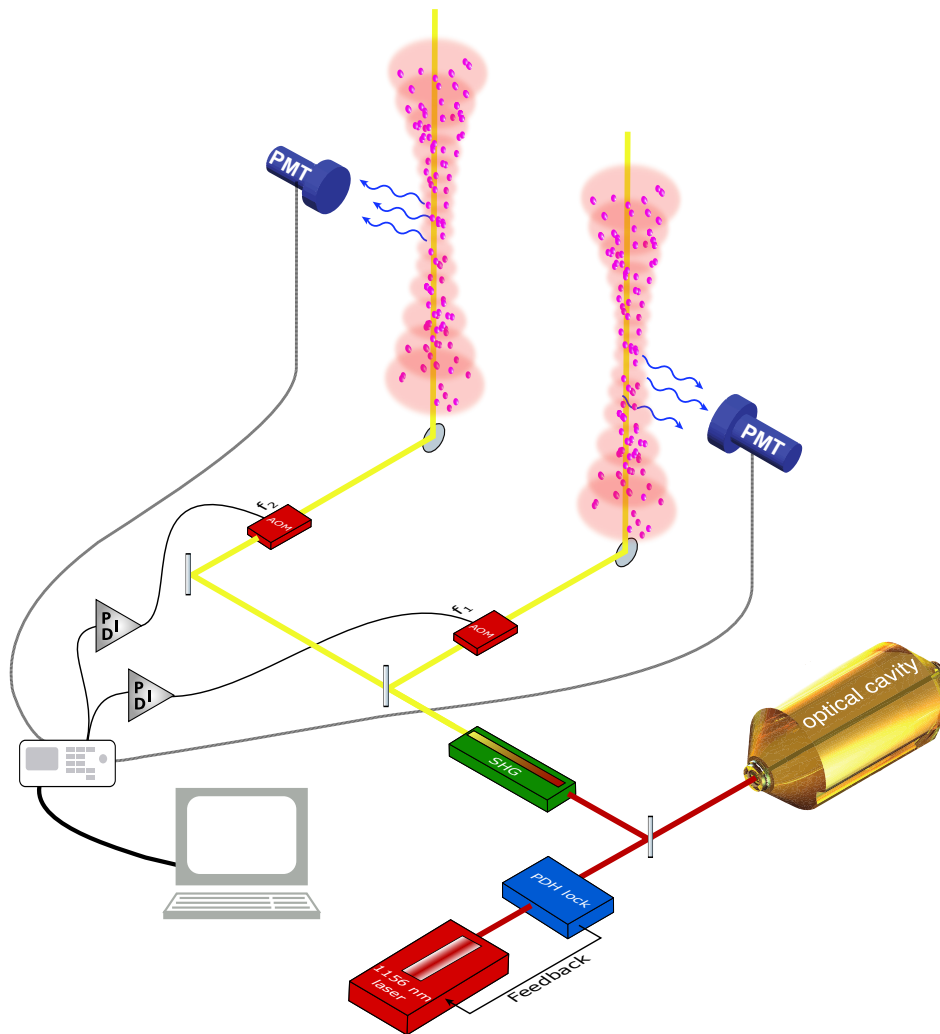
Figure 2.1: Schematic of the NIST ytterbium optical lattice clock. All laser beams are fiber coupled to the clock vacuum chamber platform. Not shown are the slowing, trapping and cooling 399 nm and 556 nm laser beams, probe laser, repump 1388 nm laser, vacuum chamber structure, and optical cavity isolation.

captured by the lattice are optically pumped to one of the $m_F = \pm 1/2$ ground states using the $^1S_0$-$^3P_1$ transition, which leaves the ytterbium sample ready for clock spectroscopy. After state preparation, we employ a simple Rabi spectroscopy scheme to excite atoms to the $^3P_0$ upper clock state. Applying a 560 ms long π-pulse of 578 nm light resonant with $^1S_0$-$^3P_0$ clock transition yields the spectroscopic line shape shown in Figure 2.2 with a Fourier-limited line width of $\sim$2 Hz.[7] Experimental clock cycles alternately interrogate the two m_F spin states, and then averages their frequency. To obtain a high S/N readout of the electronic population in the long lived upper clock state, we use a normalized electron shelving technique to detect excitation. Normalized electron shelving works as follows: we apply a series of resonant 'probe' pulses of 399 nm light to count the atomic population in the ground state - $|1\rangle$, background - B, and excited state - $|2\rangle$, via scattered fluorescence from $^1S_0$-$^1P_1$. We probe the atomic sample until all atoms that are scattering 399 nm photons are laser heated out of the lattice, while collecting the florescence signal on a photo-multiplier tube (PMT). The first readout in the sequence measures ground state population, recorded as $P_1 = |1\rangle + B$. Following this, a second identical pulse generates an integrated signal $P_2 = B$, quantifying background noise. Then, application of resonant 1388 nm light optically pumps nearly all ($>90\%$) trapped atoms from the $^3P_0$ clock state to the $^1S_0$ ground state through a quickly decaying, nearby, $^3D_1$ state. Finally, a third identical 399 nm probe pulse yields the integrated signal $P_3 = |2\rangle + B$. We compute an atomic excitation fraction, normalized against total atom number and suppressing background effects, from the three records $P_{1;2;3}$:

$$\Psi \equiv \frac{|2\rangle}{|1\rangle + |2\rangle} \approx \frac{P_3 - P_2}{P_1 + P_3 - 2P_2} \tag{2.1}$$

In order to cleanly implement the atomic state detection, the 399 nm laser is: (1) frequency stabilized to the $^1S_0$-$^1P_1$ transition using a modulation transfer spectrometer [51, 117], (2) intensity stabilized, (3) polarization filtered, and (4) sufficiently intense to drive the $^1S_0$-$^1P_1$ transition into saturation. The total photon collection efficiency from our atomic sample is $< 1\%$, due to small

---

[7] Rabi π-pulse duration is optimized for desired application. Rabi pulse times can range from 140 ms-1500 ms, limited by optical LO coherence time.
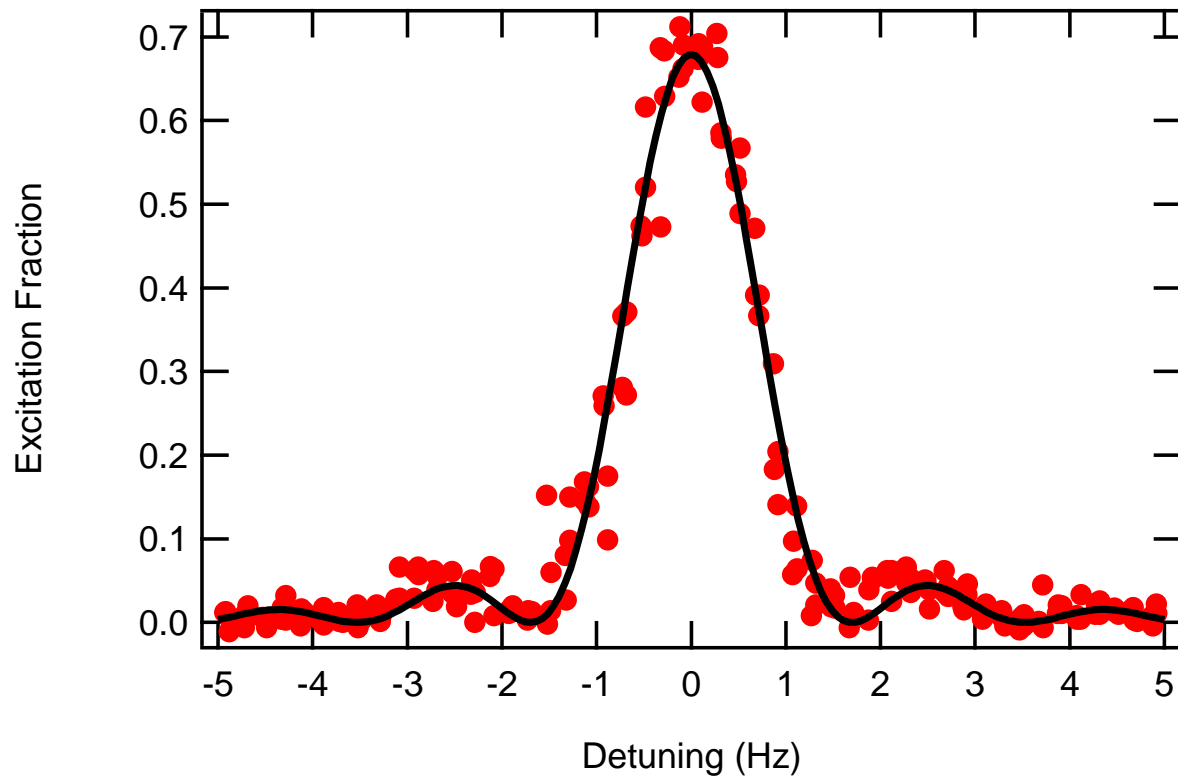
Figure 2.2: Normalized excitation spectrum of $^1S_0$-$^3P_0$ clock transition at 578 nm in ytterbium with 560 ms Rabi Spectroscopy time. The black line is a free-parameter sinc^2 function fit.

observational solid angle, PMT quantum efficiency, and transmission efficiency of a 399 nm band pass filter. However, by retroreflecting the probe light to improve the balance of optical forces, each atom scatters $> 10^3$ 399 nm photons before being laser-heated out of lattice confinement. To avoid standing wave effects, forward going and retroreflected probe beams have orthogonal polarization.

Unfortunately, excited state detection via decay from $^3D_1$ is not perfectly efficient, as atoms excited to $^3D_1$ can decay to any state in the ^3P_j manifold. We compute the branching fractions to $^3P_0$, $^3P_1$, and $^3P_2$ from matrix elements (assuming perfect LS coupling) and energy level separations, to be 0.64, 0.35, and 0.01 respectively, with $\sim 10\%$ uncertainty. Application of resonant 1388 nm light is sufficiently long to drive atom population out of $^3P_0$, forcing decay through $^3P_1$ or $^3P_2$. Even with a small branching ratio to $^3P_2$, repeated cycling from $^3D_1$ to $^3P_0$ during optical pumping can force a small fraction of atoms to the long lived $^3P_2$ state, degrading the normalization process. A separate test to improve Ψ beyond 90% by applying 776 nm light resonant with the closest $^3P_2$-$^3S_1$ transition, exciting atoms out of $^3P_2$ back to $^1S_0$ during normalization, gave no observable advantage to detection efficiency.

2.5   Autonomous clock operation and control

Continued operation is essential for measurements beyond the starting instability set by the LO as it allows averaging of frequency information derived from the atomic ensemble. Moreover, a control system links each clock component forming a working timekeeper. Yb-1 and Yb-2 atomic systems have independent but similar (in design) autonomous operating control. Each component in the atomic clock is governed by 5 V Transistor-Transistor Logic (TTL). Timing control is done with a 64 channel, field programmable gate array (FPGA) that sends TTL pulses in the desired order and duration on a designated digital output TTL channel. The FPGA is programed for each individual channel TTL output and to repeat its timing sequence for autonomous operation.[8]   Additionally, each ytterbium system has an independent atomic servo consisting of a micro-controller unit (MCU)

---

[8] The FPGA can be programed to repeat a timing sequence indefinitely.

updating a direct-digital synthesizer (DDS). When the MCU receives a TTL pulse, it applies a correction signal $f_{1;2}$ derived from the respective atomic excitation fraction signal - Ψ, with necessary frequency control for locking to $m_F = \pm 1/2$ transitions. After clock spectroscopy, the MCU records the probe pulse signals, $P_{1;2;3}$, computes a new Ψ', and new correction signal $f'_{1;2}$. The FPGA timing sequence shown in Figure 2.3 is repeated with a characteristic cycle time T_c. Yb-1 and Yb-2 atomic servos apply discrete corrections $f_n(t(n)_i)$ at unsynchronized times $t(n)_i$. Independent computers record and timestamp each correction $f_n(t(n)_i)$ from the MCUs. If a comparison between Yb1-Yb2 is needed, we employ a piecewise-cubic Hermite interpolating polynomial during post-processing to establish f_1 and f_2 on a common set of timestamps separated by the average of the two systems cycle durations, $T_{12} = \frac{1}{2}(T_1 + T_2)$ and generate a difference frequency $\Delta f = f_1 - f_2$.

By design, Yb-1 and Yb-2 atomic systems are largely independent of each other. If systematic variations of each atomic frequency existed and they were positively correlated, then these variations would reduce the frequency difference and fluctuations giving false operating performance. Their most significant shared attribute is co-location in the same laboratory. While local heat loads independently influence each atomic apparatus, the ambient laboratory temperature can drive temperature correlations that equally influence the blackbody Stark shift for each system. However, most technical systematic effects, like stark shifts, Zeeman shifts, and lattice light shifts are independent for each system.

Time (ms)	40	20	17	20	30	20	7	10	8	25	25	230	25	1	6	7	5	1	7	4	1	1	7	3
Blue Slowing/Trapping Shutters	█	█																						█
Blue Slow AOM	█	█																						
Blue Trap AOM	█	█																						
Blue Probe Shutter															█	█	█	█	█	█	█	█	█	█
Blue Probe AOM																█			█				█	
Green MOT Shutter	█	█	█	█	█																			
1st Green MOT AOM	█	█	█																					
2nd Green MOT AOM				█																				
3rd Green MOT AOM					█																			
Green Optical Pumping Shutter						█	█	█	█															
Green Optical Pumping AOM								█	█															
Blue Quad Coil	█	█																						
Green Quad Coil 1			█																					
Green Quad Coil 2				█	█																			
Re-pump AOM																				█				
Re-pump Shutter																				█	█			
Yellow AOM										█	█	█	█											
Yellow Intensity servo											█	█	█											
Yellow Optical Fiber Switch								█	█	█	█	█	█											
Magnetic Bias Coil 1 (Optical Pumping)								█	█															
Magnetic Bias Coil 2 (Yb Spectroscopy)										█	█	█	█											
Atomic Beam Shutter	█	█	█	█	█	█																		█

█ TTL: +5 Volts

▮ TTL: 0 Volts

Figure 2.3: An example of the Field Programmable Gate Array (FPGA) TTL output timing sequence used by both ytterbium systems. Total FPGA output can accommodate 64 digital TTL channels with 50 ns resolution.

Chapter 3

Atomic Clock Instability

The instability of a time or frequency standard is a fundamental property defined by variations in its periodicity over different timescales. Essential first steps for timing metrology are characterizing the statistical measurement precision of the clock oscillator and exploring noise processes which govern the timekeeper operation. Here we study the fundamental instability limitations of atomic clock oscillators and review the history of instability performance of lattice clocks, leading to the observed 1.6×10^{-18} measurement precision of our Yb atomic systems. Finally, we discus further improvements to enable routine measurements at 10^{-18} precision and beyond.

3.1   Instability of a clock oscillator

An *ideal* oscillator would emit an exact oscillation of its design, producing the correct phase and frequency. To construct such an ideal device is impossible, therefore we must account for errors and fluctuations the emitted oscillation will exhibit. If we consider a real oscillator with output frequency, f_0, we can define the oscillator noise as fluctuations in the instantaneous output frequency about f_0. In the most elementary case, the instability of a frequency standard, scales with the product of its signal to noise ratio, S/N, and quality factor, $f_0/\delta f$ (fractional instability, σ, as the inverse). However, this simple representation only quantifies the initial oscillator instability. Looking at the spectrum of frequencies that form the fluctuations, typically reported as a *noise power spectral density*, we can deduce the character of noise governing the oscillator [5]. Impor-

tantly, if the noise is favorable, averaging frequency information can achieve improved measurement precision.

The noise power spectral density for every object is unique, however, most man-made oscillators (e.g. optical cavities, quartz crystal oscillators...) have 'flicker' noise characteristics [10, 90]. Flicker noise processes produce a power spectral density that scales as $f^{-\alpha}$ for $\alpha \geq 1$, often referred to as a 'pink' noise spectral density. Unfortunately, flicker noise yields no benefit from averaging frequency information. Conversely, general quantum systems (e.g. atoms) have distinct energy (frequency) eigenstates that can be repeatedly observed in a statistically uncorrelated way, producing white noise frequency statistics. White noise processes produce a constant power spectral density over the frequency spectrum and benefit from averaging frequency noise information. We aim to transfer this favorable atomic noise characteristic to our constructed oscillators, suppressing the flicker-type noises inherent to man-made systems.

One way to transfer a quantum oscillator's inherent stability to an optical oscillator is to allow the oscillator output to perturb the quantum oscillator (atom). As the atom experiences the harmonic, resonant, perturbation from the oscillator's electric field, the transition amplitude begins to oscillate sinusoidally, a phenomenon commonly known as Rabi flopping [116, 23]. The probability of provoking a transition in such an ideal perturbation can be written as

$$P_{|1\rangle \to |2\rangle}(t) \propto \sin^2(\omega_r t/2) \tag{3.1}$$

where ω_r is the Rabi flopping frequency [23]. By applying servo feedback to the oscillator frequency output to excite a transition with a desired probability fraction (e.g. $P_{|1\rangle \to |2\rangle} = 50\%$), we tune the oscillator frequency relative to an atomic transition probability. In this way, the probabilistic nature of the atom's electronic wave function is written on the oscillator's frequency output, producing a net oscillator output governed by 'white' frequency noise. Furthermore, in a clock with N atoms, this process takes place for each atom, implying the total uncertainty in measurement of the transition frequency reduces by $\sqrt{N}$ for a single quantum measurement.

As an atomic clock attempts to servo an oscillator to an atomic sample, any reduction in atomic sensitivity to oscillator noise components will degrade this transfer process, limiting clock performance. Let us consider the case of a non-ideal oscillator, where δP is the change in a transition's probability of occurrence due to oscillator output fluctuations $\delta \omega(t)$. We can write this interaction as

$$\delta P = \frac{1}{2} \int g(t) \delta \omega(t) dt \tag{3.2}$$

where $g(t)$ is the atomic sensitivity function to deviations in the frequency of the perturbative laser field [109]. For an atomic clock, $g(t)$ is determined by the type and duration of spectroscopy executed on the clock transition and is generally a time-varying function over atomic interrogation [109]. Furthermore, because radiation-absorption-type clocks (e.g. the optical lattice clock) operate in an intrinsically pulsed mode, where some duration of the clock cycle is spent preparing the atomic sample, $g(t)$ is identically zero for a fraction of the clock cycle. A 'dynamic' $g(t)$ is fundamental to sequentially operated frequency standards and is commonly the root cause in degradation of an atomic oscillator's frequency stability. A time-varying $g(t)$ results in a technical noise source known as the Dick effect, which arises when an oscillator is periodically observed [109, 35]. Higher frequency Fourier noise components that are near harmonics of the clock cycle are aliased by the stroboscopic nature of clock operation. From the atom's perspective, these aliased noise components appear as low frequency noise on the oscillator output, indistinguishable from the oscillator's natural low frequency noise. The atomic servo corrects for both aliased noise and low frequency noise, introducing extra instability into the oscillator frequency output; setting a fundamental 'Dick noise' limit to oscillator instability. We can write instability limit due to Dick effect as [109]

$$\sigma_{Dick} = \sqrt{\frac{1}{\tau} \sum_{m=1}^{\infty} \left(\left(\frac{g_m^{cos}}{g_0} \right)^2 + \left(\frac{g_m^{sin}}{g_0} \right)^2 \right) S(m/T_c)} \tag{3.3}$$

where $S(m/T_c)$ is the single-sided power spectral density of the free running oscillator frequency fluctuations at Fourier frequencies m/T_c, T_c is the clock cycle time, and the parameters g_0, g_m^{cos},

and g_m^{sin} are defined as [109]:

$$g_0 = \frac{1}{T_c} \int_0^{T_c} g(x)dx \tag{3.4}$$

$$g_m^{cos} = \frac{1}{T_c} \int_0^{T_c} g(x)\cos(2\pi\frac{m}{T_c}x)dx \tag{3.5}$$

$$g_m^{sin} = \frac{1}{T_c} \int_0^{T_c} g(x)\sin(2\pi\frac{m}{T_c}x)dx. \tag{3.6}$$

The most direct way to reduce the Dick effect is to build a better oscillator, where noise overall, and pink noise components are simply suppressed. Other techniques to construct uniform, and continuous $g(t)$ functions are currently under study, however, at the time of this writing, state-of-the-art atomic clocks are still limited by the Dick effect.

The measure of frequency stability in clocks and oscillators is quantified by the Allan Variance or the Allan deviation (square root of Allan variance) [5]. The Allan deviation, $\sigma_y(\tau)$, describes instability of an oscillator for various averaging intervals τ. The slope of $\sigma_y(\tau)$ reveals the nature of frequency noise exhibited by the system. Notably, flicker frequency noise results in a τ-independent Allan deviation and white frequency noise has a functional form of $\sigma_y(\tau) \propto \tau^{-1/2}$, yielding a linear slope of -1/2 on a traditional log-log Allan deviation plot. Also, since long-term instability is typically limited by drifts in systematic effects we can use the Allan deviation to investigate systematic frequency errors in the oscillator. Finally, the Allan deviation is insensitive to absolute frequency offset, and only sensitive to *changes* of frequency.

3.2   Lattice clock instability

An optical lattice clock typically employs a destructive measurement to detect atomic excitation fraction each clock cycle. This quantum measurement procedure includes random processes that produce fundamental noise sources affecting the clock instability. We can write the total instability of a many atom clock system as

$$\sigma_y(\tau) = \frac{1}{\pi}\frac{\delta f}{f_0}\sqrt{\frac{T_c}{\tau}}\left(\frac{1}{N} + \frac{1}{Nn_{ph}} + \frac{2\sigma_N^2}{N^2} + \gamma\right)^{1/2} \tag{3.7}$$

where N is the number of atoms, T_c is the experimental cycle time, n_{ph} is the average number of collected photons from each quantum oscillator, σ_N is the uncorrelated RMS atom number fluctuation, and γ accounts for frequency noise from a periodically observed optical oscillator [81]. Each term can be attributed to a unique noise source in the lattice clock's operation, and be divided into two classes: detection noise and local oscillator noise. The first three terms in Equation 3.7 represent detection noise and incorporate all sources of instability originated from atomic state measurement. The remaining term represents noise originating from the local oscillator. Importantly, noise processes in Equation 3.7 only affect the clock instability magnitude but do not change the white frequency character of the atomic timekeeper.

3.2.1   Atomic detection noise

The first term in Equation 3.7 gives the quantum projection noise of the atomic population of trapped atoms in the optical lattice. This term represents a fundamental 'atom shot noise' limit set by quantum mechanics for independent atoms when measuring our transition probability. To illustrate, consider a single two level system with eigenstates $|1\rangle$, $|2\rangle$. Starting with the system in the ground state, $|1\rangle$, we attempt to change eigenstates by perturbing our system with a laser field. After extinguishing the laser field, we leave the quantum system in a superposition state, $\alpha|1\rangle + \beta|2\rangle$. Then by measuring the state population, we collapse the wave function to a single eigen state, $|1\rangle$ or $|2\rangle$. Each measurement result is either $|\beta|^2 = 0$ (no excitation) or $|\beta|^2 = 1$ (successful excitation). In particular, we are interested if the system is in state $|2\rangle$, indicating atomic radiation absorption. While repeated measurements, or simultaneous measurements of identically prepared atoms, would produce an average value of $|\beta|^2$, individual measurements are susceptible to discrete fluctuations, a phenomenon called quantum projection noise [59]. The instability resulting from quantum projection noise can be calculated from Equation 3.7 after measuring the number of lattice trapped atoms, typically through $^1S_0$-$^1P_1$ laser-induced-fluorescence electron shelving detection. In an optical lattice clock there are 10^3-10^6 atoms acting as single two level systems performing the

above quantum experiment with the cumulative effect of dramatically reducing quantum projection noise. Combining large number of atoms with the typical narrow band electronic transition linewidths ($\frac{\delta f}{f} << 10^{-14}$) enables optical lattice clocks to have a potential quantum projection noise limited fractional measurement precision of $\sigma_y(1\ s) \sim 1 \times 10^{-17}$ or better.

The second term Equation 3.7 accounts for photon shot noise associated with the laser-induced-florescence detection method. Because the $^3P_0$ clock state is long lived, we utilize florescence from $^1P_1$-$^1S_0$ for state detection.[1] Photons entering the photo multiplier tube detector are susceptible to detection signal shot noise. Each atom in $^1S_0$ scatters $> 10^3$ photons before being heated out of the lattice potential, so even with our small collection solid angle, we expect $n_{ph} >> 1$ in Equation 3.7. This term is easily calculated from knowledge of the collection solid angle, atomic scattering rate, and photo multiplier tube detection efficiency. In our experimental setup we have a combined collection efficiency (captured solid angle and PMT efficiency) of $\sim 1\%$ and we saturate the $^1P_1$-$^1S_0$ transition (saturation parameter > 1, linewidth ~ 30 MHz). In the most pessimistic case, assuming 10^3 photons are scattered, $n_{ph} \approx 10$, implying photon shot noise is well below the atomic quantum projection noise limit.

The third term in Equation 3.7 results from fluctuations in atom number between periodic load/probe cycles and the normalized electron shelving technique. We load a new atomic sample each clock cycle, and expect some fluctuations in atom number between cycles as well as inefficiencies in our normalization method. Unfortunately, the clock servo error signal cannot distinguish excited state atom number fluctuations and changes in excitation probability due to changes in detuning. Because both types of changes are corrected in the clock servo, the clock stability degrades. Shot-to-shot atom number fluctuations on our system are $\sim 30\%$ but the effects from this fluctuation are strongly suppressed by the normalization scheme where the excited state is measured as a fraction of the total atom number.[2] Although the normalized atomic excitation

---

[1] See Chapter 2
[2] See Chapter 2 for more details.

signal greatly reduces our sensitivity to σ_N, inefficiencies in the normalization process technique (e.g. imperfect electron shelving, finite lattice trap lifetime, etc.) increase uncertainty in $|1\rangle$ and $|2\rangle$ populations. To measure the atom fluctuation term, we Fourier-broaden the clock transition and record our normalized atom signal for several minutes on resonance. We measure an RMS normalized fluctuation, σ_n/N, of $\sim 2\%$, implying a fractional frequency instability of $\sigma_y(1\ s) = 2 \times 10^{-17}$ due to residual technical noise.[3]

3.2.2 Local oscillator noise

The final instability term in Equation 3.7 originates from the local oscillator. This instability term can be calculated from the local oscillator cavity noise and atomic sensitivity function, $g(t)$. We measured our optical cavity noise by utilizing the atomic transition as an independent frequency discriminator. We found a flicker frequency instability of $\sigma_{LO} \sim 1.5 \times 10^{-16}$ for averaging intervals of 1 s to 1000 s. This measurement also includes atomic detection noise, however, we note that these noise components are approximately an order of magnitude below the expected cavity thermal noise floor. We evaluate the resulting Dick instability from Equation 3.3 by calculating the atomic sensitivity function for our given spectroscopy configuration and the correct noise power spectral density evaluated at m/T_c yielding [109, 105]:

$$\sigma^2_{Dick} = \frac{\sigma^2_{LO}}{2\ln(2)} \frac{T_c}{\tau} \sum_{m=1}^{\infty} \left(\frac{g_m^{cos} + g_m^{sin}}{g_0} \right)^2 \frac{1}{m} \tag{3.8}$$

where g_0, g_m^{cos}, and g_m^{sin}, are given by Equations 3.4, 3.5, 3.6, $S(f) = \frac{1}{2\ln(2)}\sigma^2_{LO}\frac{1}{f}$ is the noise power spectral density of flicker frequency modulation [105], and σ_{LO} is the thermal noise limited cavity stability. With a state-of-the-art thermal noise limited cavity and typical operating conditions, we find a Dick instability limit of $\sigma_{Dick}(1\ s) \sim 5 \times 10^{-17}$ and $\sigma_{Dick}(1\ s) \sim 3 \times 10^{-17}$ for Rabi and Ramsey spectroscopy, respectively. Unfortunately these instability limits are still above the lattice clock potential of $10^{-17}/\sqrt{\tau}$ or better, set by the quantum projection noise. Additional

---

[3] Assuming a clock cycle time of 0.3 s
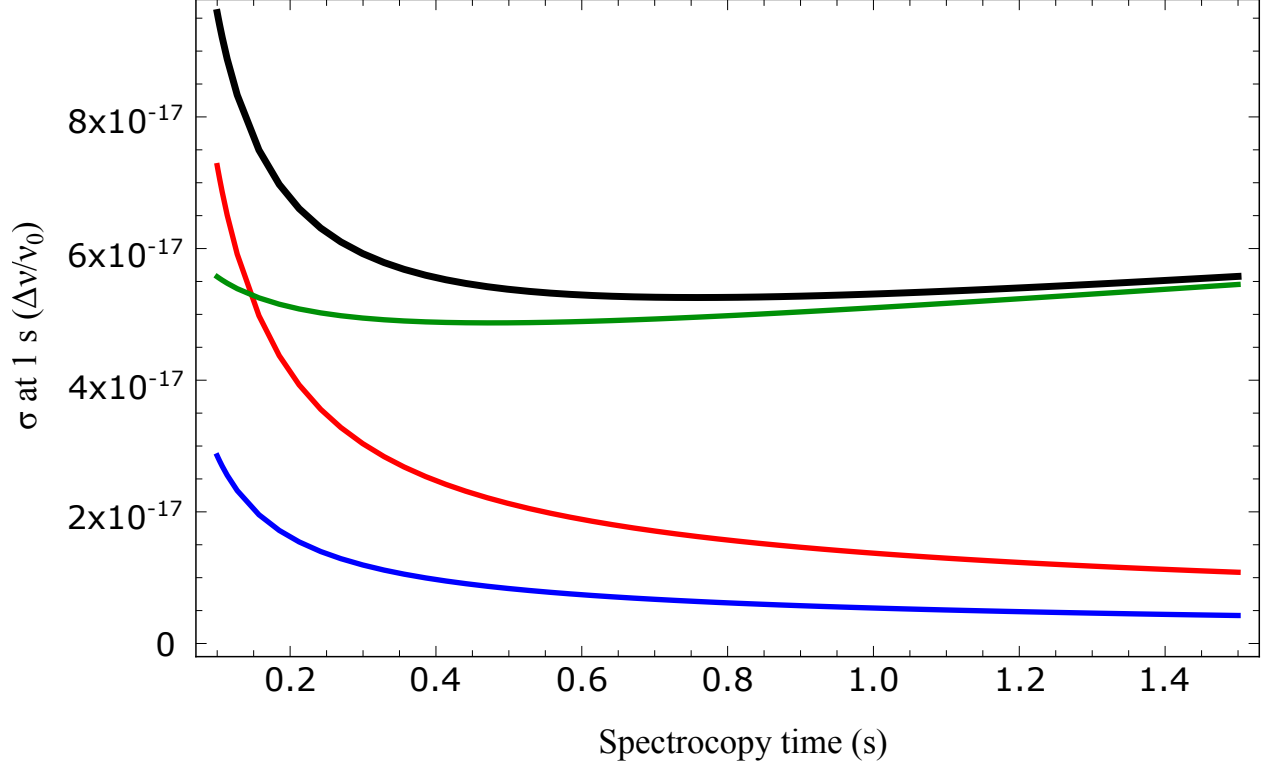
Figure 3.1: Relevant noise processes limiting fractional instability of a hypothetical atomic frequency standard with 10^4 atoms and an optical oscillator thermal noise floor of 1.0×10^{-16}. For normalized oscillator comparison, total clock instability is evaluated at $\tau = 1$ s for an ensemble perpetration time of ~ 0.200 ms preceding Rabi spectroscopy. We assume n_{ph} to be ~ 700 and rms fluctuations in the normalized atom number signal to be 1.8%. The blue, red, and green curves represent the calculated quantum projection noise, combined atomic detection noise, and the Dick instability limit respectively. The black curve is the calculated total instability of the clock system.

techniques attempt to lower the Dick limit by maximizing $g(t)$ by employing Ramsey instead of Rabi spectroscopy, non-destructive state detection, synchronous interrogation, and interleaved atomic clocks [132, 126, 55]. Unfortunately, the Dick effect continues to limit the measurement precision of many optical lattice clocks. A summary of each noise component and corresponding instability contribution for a typical clock operation under Rabi spectroscopy is given in Figure 3.1.

3.3   History of optical atomic clock instability

The first lattice clocks constructed achieved 10^{-14} to 10^{-15} level instability performance simply by taking advantage of high optical transition frequencies, and work has since progressed rapidly worldwide [82, 69, 123]. An important milestone was achieved with the demonstration of lattice clock performance with short-term (1 s) frequency instability in the low 10^{-15} levels, which averaged to low 10^{-16} levels at many hundreds of seconds [83]. This level of performance far exceeded the best cesium standards and was competitive with the most accurate (at that time) optical clocks, which were based on single trapped ions [93]. However, demonstration of the lattice clocks' full potential was still hindered by the Dick effect [109, 35]. One approach to overcoming this limitation was improving the ultra-stabilized laser used to interrogate the clock transition. Typical limits to laser stability stemmed from acceleration-induced cavity length fluctuations, and Brownian thermal mechanical fluctuations of cavity components. Efforts to push laser stabilization led to acceleration insensitive cavities and cavity designed with reduced thermal noise. These techniques demonstrated clock instability well below 10^{-15} at short times with a thermal noise limited laser at a fractional frequency instability of $\sim 4 \times 10^{-16}$ from 1 s to 10 s [62]. Alternatively, synchronized interrogation of two lattice clocks with the same stabilized laser exploited rejection of the Dick effect in common mode to probe performance beyond the Dick limit. This technique produced a correlated measurement instability of 4×10^{-16} at short times, approaching 1×10^{-17} for averaging times greater than 1,000 s [126]. However, this stability is only representative of clock lasers that share a common local oscillator. A few years later, an uncorrelated comparison

of two independent strontium lattice clocks revealed clock instability of 3×10^{-16} at short times, averaging down to 1×10^{-17} in 1,000 s or, in another case, reaching the 10^{-17} level in 20,000 s [88, 68]. Interestingly, even with a relatively quick averaging time of 1000 s, clock stability never broke the 10^{-17} barrier, indicating that additional control of systematic shifts was required for measurement precision extending to the 10^{-18} level. Work detailed here compares two independent ^{171}Yb optical lattice clocks, demonstrating an uncorrelated measurement precision of 1.6×10^{-18} in 25,000 s, a key milestone for applications that have long sought this level of performance.

3.4   Comparison of spin-$1/2$ ytterbium systems

As described in the experimental section, the two ytterbium lattice clock systems, referred to here as Yb-1 and Yb-2, cool and collect ^{171}Yb atoms from a thermal beam into magneto-optical traps. Two stages of laser cooling, first on the strong $^1S_0$-$^1P_1$ cycling transition at 399 nm, followed by the weaker $^1S_0$-$^3P_1$ intercombination transition at 556 nm, reduce the atomic temperature from 800 K to 10 μK. The three green MOT stages, lasting 30 ms, 30 ms, and 20 ms respectively for both systems, use increasingly resonant 556 nm light and a smaller but varying magnetic field gradient to further cool and compress the atomic cloud. Each cold atom sample is then loaded into an optical lattice with $\sim$300 E_r trap depth (recoil energy $E_r/k_B = 100$ nK) formed by retro-reflecting approximately 600 mW of laser power, fixed at the magic wavelength, λ_m, by a reference cavity. The frequency difference between the lattice lasers of Yb-1 and Yb-2 is directly detected in a heterodyne optical interferometer with separate AOMs shifting their frequency to a fixed 1 MHz offset at the atoms. After extinguishing the green MOT beams, we apply a $\sim$0.5 mT magnetic field and spin polarize trapped atoms by optical pumping on $^1S_0$-$^3P_1$. For the measurements described here, about 5,000 atoms, captured by each lattice, are pumped to a single ground state magnetic sub-level with a fidelity exceeding 95%. After this state preparation, another $\sim$0.1 mT field lifts the Zeeman degeneracy during 578 nm clock spectroscopy [73]. Applying a 140 ms long π-pulse of 578 nm light resonant with the $^1S_0$-$^3P_0$ clock transition yields a sinc^2 spectroscopic line shape,

with a Fourier-limited linewidth of 6 Hz, for a starting measurement precision of 3×10^{-16}. Rabi spectroscopy with a 140 ms pulse time provides a convenient combination of narrow lineshape, short clock cycle, and reliability when locking to the clock transition.

The optical local oscillator (LO) is servo-locked to a high-finesse optical cavity and is shared by both Yb systems [62]. Experimental clock cycles alternately interrogate both m_F spin states canceling first order Zeeman and vector Stark shifts [73]. Light is frequency-shifted into resonance with the clock transition of each atomic system by independent acousto-optic modulators (AOMs) following the 578 nm fiber system.[4] During spectroscopy, all resonant laser beams are extinguished when appropriate by both AOMs and shutters, with the exception of 578 nm light. The optical lattice beam is continuously applied with actively stabilized intensity. To suppress phase chirps on the clock light from AOM switching, we drive AOMs with < 10 mW of radio-frequency power. By measuring the normalized excitation while modulating the clock laser frequency by ± 3 Hz, an error signal is computed for each Yb system. Subsequently, independent microprocessors provide a digital frequency correction $f_{1;2}(t)$ to their respective AOMs, thereby maintaining resonance on the line center. In this way, though derived from the same LO, the individual laser frequencies for Yb-1 and Yb-2 are decoupled, and are instead determined by their respective atomic samples (for all but the shortest time scales).

During operation of the clock systems, special attention is paid to eliminating residual Stark shifts stemming from amplified spontaneous emission of the lattice lasers, to eliminating residual Doppler effects from mechanical vibrations of the apparatus correlated with the experimental cycle, and to controlling the cold collision shift due to atomic interactions within each lattice site. Computers record the frequency correction signals $f_{1;2}(t)$ for the full comparison time. Because the experimental cycles for each clock system are not synchronized and have different durations, the recorded correction frequencies are interpolated to a common time base and then subtracted

---

[4] This technique was modified after this measurement to reach an overall systematic clock uncertainty at the 10^{-18} level, see Chapter 6 for details.

to compute the frequency difference between Yb-1 and Yb-2.

To evaluate the Allan Deviation for these clock systems measurements such as these were repeated several times for intervals of $\sim$15,000 s, demonstrating a clock instability reaching 4×10^{-18} at 7,500 s. While collecting data over a continuous 90,000 s interval, we observed the instability curve in Figure 3.2, shown here as the total Allan deviation for a single Yb clock. Prior to data analysis, approximately 25% of the attempted measurement time was excluded due to laser unlocks and auxiliary servo failures. Each servo used to stabilize the laser to the clock transition had an attack time of a few seconds, evidenced by the instability bump near 3 s. At $\tau = 1 - 5$ s, the instability is comparable to previous measurements of the free-running laser system, and at longer times the instability averages like white frequency noise as $3.2 \times 10^{-16}/\sqrt{\tau}$ (for averaging times τ in seconds), reaching the instability of 1.6×10^{-18} at 25,000 seconds. For all measurements described here, the mean frequency difference $f_2(t) - f_1(t)$ were within the Yb-1 Yb-2 uncertainty of 10^{-16} at the time of operation. Also shown in Figure 3.2 is an estimate of the combined instability contribution (blue dashed) from the Dick effect and quantum projection noise (QPN), with the shaded region denoting the uncertainty in these estimates. As can be seen, the observed instability lies close to the combined contributions. We anticipate that significant reductions are possible in the QPN limit by simply using higher atom numbers and longer interrogation times. However, despite earlier reductions in the Dick effect from improved local oscillators, Dick noise continues to limit the performance of this clock.

3.5   Frequency measurement at 10^{-18} and beyond

For future measurements to be practical, the Dick effect must be reduced so that 10^{-18} measurement instability can be realized in 100 seconds or less. Further stabilization of the optical LO will continue to reduce the Dick limit, both by lowering the laser frequency noise (which is down-converted in the Dick process) and by allowing increased spectroscopy times and thus higher duty cycles. Such laser systems will use optical cavities exhibiting reduced Brownian thermal-mechanical
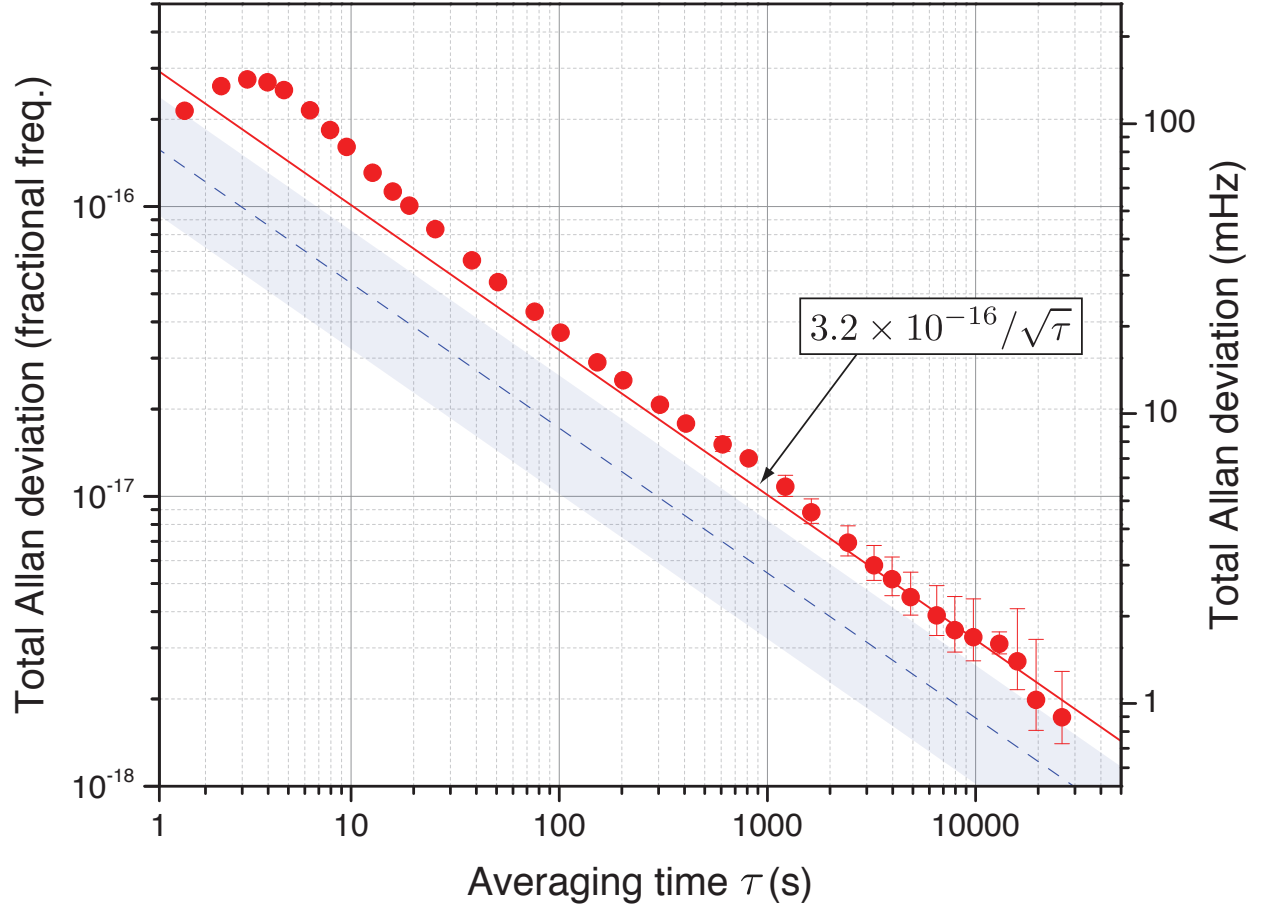
Figure 3.2: Total Allan deviation of a single Yb clock, $(f_2(t) - f_1(t))/\sqrt{2}$ (red circles), and its white-frequency-noise asymptote of $3.2 \times 10^{-16}/\sqrt{\tau}$ (red solid line). The blue dashed line represents the estimated combined instability contribution from the Dick effect $(1.4 \times 10^{-16}/\sqrt{\tau})$ and QPN $(1 \times 10^{-16}/\sqrt{\tau})$, with the shaded region denoting uncertainty in these estimates.

noise by exploiting cryogenic operation, crystalline optical coatings, longer cavities, or other techniques [65, 62, 31]. Figure 3.3 demonstrates the benefit of using an optical LO improved over that used in this work, with four times less laser frequency noise and with four times longer interrogation time (corresponding to a short-term laser instability 5×10^{-17}). The red dotted line gives the Dick instability, while the black dashed line indicates the QPN limit with the same interrogation time, assuming a moderate atomic population of 50,000. Noting that the calculated Dick effect remains several times higher than the QPN limit, we consider an alternative idea first proposed for microwave ion clocks: interleaved interrogation of two atomic systems [35]. By monitoring the LO laser frequency at all times through the use of two interleaved atomic systems, the aliasing problem at the heart of the Dick effect can be highly suppressed. The solid blue line in Figure 3.3 illustrates the potential of a simple interleaved-clock interrogation using basic Ramsey spectroscopy. Even with LO noise levels unimproved from the present work, the Dick effect lies well below a much improved QPN limit (black dashed line). In this case, spin squeezing of the atomic sample could reduce the final instability beyond the standard quantum limit set by QPN (e.g., [115]). The two-system, interleaved technique requires spectroscopy on each atomic system to last one half or more of the total experimental cycle. By extending the clock spectroscopy time to ≥ 250 ms, we have achieved a 50% duty cycle for each Yb system, demonstrating the feasibility of this technique. Duty cycles of 50% can also be realized with the aid of nondestructive state detection [132].

With current instability performance, we can efficiently explore systematic effects on each system at the 10^{-18}-level uncertainty. Conversely, because long-term instability is typically limited by systematic drifts, further reduction and control of our systems uncertainties will likely offer improved instability. With continued progress, we envision that 10^{-18} instability at 100 s and long-term instability well below 10^{-18} can be achieved.
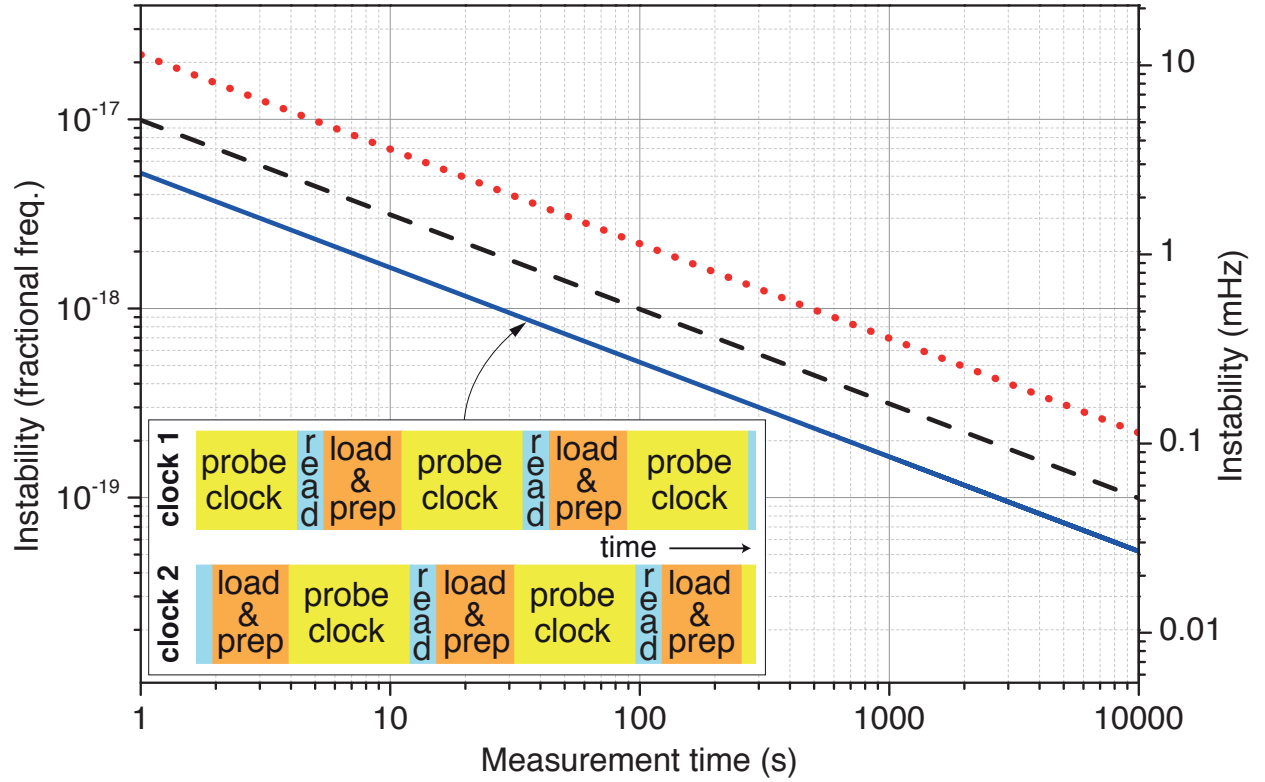
Figure 3.3: Calculated instability limits for an improved lattice clock towards the goal of 1×10^{-18} in 100 s. The Dick limit (red dotted) is reduced by using a LO which is four times as stable as that used in this work. The QPN limit is also shown under the same conditions (black dashed) with a total atom number of 50,000. The inset illustration represents an interleaved interrogation of two atomic systems, allowing continuous monitoring of the LO for suppression of the Dick effect. Dead times from atomic preparation or readout in one system are synchronized with clock interrogation in the second system. The solid blue line indicates the suppressed Dick instability in the interleaved-interrogation scheme of two atomic systems using Ramsey spectroscopy with an unimproved LO.

3.6   Elimination of Dick noise in an optical clock

Key to realizing the full performance of an optical lattice clock is the reduction or elimination of Dick noise from the optical local oscillator. A multi-clock architecture is the most direct way to eliminate noise arising from the local oscillator. When merged together, the ensemble of clocks remains sensitive to an atom sample at all times, allowing continuous frequency corrections and therefore extreme suppression of Dick noise. As mentioned above, we directly realized an asynchronous two clock system with improved atom sensitivity by extending our clock duty cycles beyond 50%. While a direct instability measurement of such a system is impossible because we lack two pairs of atomic clocks, we can evaluate the potential stability of a four clock architecture through comparisons between two atomic clocks in a synchronized interrogation scheme [126]. In such a configuration the Dick noise is correlated and common-mode rejected from the two clocks. Recent comparisons between our two Yb systems employing Ramsey synchronized scheme found a measurement stability of $8 \times 10^{-17}/\sqrt{\tau}$. Assuming each clock in an ensemble performs identically, the clock ensemble would be $\sqrt{2}$ more stable than the synchronized measurement because it accumulates atomic measurements and local oscillator corrections twice as quickly. This would yield an single clock instability of $6 \times 10^{-17}/\sqrt{\tau}$ with a Dick instability limit of $< 3 \times 10^{-18}/\sqrt{\tau}$, or a 1×10^{-18} frequency measurement in a mere few thousand seconds. Further reduction of the Dick effect could likley be realized by constructing even more uniform composite $g(t)$ functions from additional atomic systems or adjustment of the spectroscopy parameters.

Alternatively, two systems can be combined so that one uses short interrogation periods on one atomic system to pre-stabilize the optical local oscillator for increased interrogation time on a second atomic system [67, 19]. The longer interrogation time improves the clock quality factor, reducing the detection noise processes in the atomic state measurement. Unfortunately, a simple two-clock configuration of this technique would still suffer reduced stability performance in dead times of the longer interrogation clock, implying the need for an architecture with more atomic

clocks.

Chapter 4

Blackbody Radiation Shift

Ytterbium clocks are remarkably insensitive to environmental effects. However, striving for 10^{-18} level performance, requires accounting for even miniscule perturbations to the clock frequency. Perhaps the most important clock perturbation results from the emission of electromagnetic radiation by all bulk matter with a non-zero temperature. As a consequence, the ytterbium atoms in our apparatus experience an ocean of thermal photons from the surrounding environment. This radiation stretches the electronic cloud, shifting the natural transition frequencies. Not surprisingly, this effect contributes the biggest source of uncertainty in many atomic clocks including cesium fountains, single ions, and optical lattice clocks [60, 84, 41]. Here we dissect the thermal radiation systematic by studying the ytterbium atom response to static and dynamic electric fields. Then we construct a well-defined thermal environment, controlling the shift at 1 part in 10^{18} [11]. Finally we heat our system to induce a thermal shift, directly testing our treatment of this effect.

4.1 Blackbody radiation and the ytterbium atom

In thermal equilibrium, electromagnetic energy is absorbed and re-emitted by all bulk matter in a constant photon exchange. Characterizing a system on a photon-to-photon basis would be a cripplingly complex undertaking. To this end, we approximate the thermal exchange between matter: (1) we envision an idealized 'blackbody' that absorbs all incident electromagnetic radiation, regardless of frequency or angle of incidence, and (2) this blackbody emits energy at a particular

rate according to its surface area and temperature. The power (photons per unit time) emitted by a blackbody is given by the Stefan-Boltzmann law, simply energy radiation per unit area per unit time is proportional to a blackbody's temperature to the fourth power:

$$P = \sigma T^4 \tag{4.1}$$

where σ is the Stefan-Boltzmann constant. Furthermore, we describe the spectral radiance at frequency ω emitted by a blackbody in terms of temperature T with Planck's Law:[1]

$$u_\omega(\omega, T) = \frac{\hbar}{4\pi^3 c^2} \frac{\omega^3}{e^{\frac{\hbar\omega}{k_B T}} - 1} \tag{4.2}$$

Planck's law and the Stefan-Boltzmann law provide a foundation for our investigation of ytterbium's interaction with thermal photons or blackbody radiation (BBR). In general, the energy shift on a electronic state n from dipole coupling to an electric field wave of angular frequency, ω, is given by

$$\Delta E_n = -2\pi \int_0^\infty u_\omega(\omega, T)\alpha_n(\omega)d\omega \tag{4.3}$$

where $\alpha_n(\omega)$ is the frequency dependent atomic polarizability,

$$\alpha_n(\omega) = \frac{2}{3} \sum_{n' \neq n} \left|\langle n' \|\mathbf{D}\| n \rangle\right|^2 \frac{\omega_{n'n}}{\omega_{n'n}^2 - \omega^2} \tag{4.4}$$

Qualitatively speaking, the above integral is a calculation of the cumulative extent that BBR energy overlaps with the polarizability of an atom. In Figure 4.1 we see the spectral radiance of a room temperature blackbody as predicted by Planck's law overlapped with relevant ytterbium polarizability. Fortunately near room temperature the radiation density is firmly peaked around 9.6 μm, far red-detuned from any strong electronic transitions in ytterbium (i.e. low atomic elasticity). Consequently, the polarizing effect of BBR is reduced and largely mimics that of a static electric field. In this far detuned limit, $\alpha_n(\omega)$ can be expressed as a static polarizability where the evaluation of Equation 4.3 only yields a small dynamic correction to the overall BBR shift of the clock transition. The frequency shift due to BBR can thus be expressed as:

$$\Delta\nu_{BBR} = \Delta E_{|2\rangle} - \Delta E_{|1\rangle} \cong -\frac{1}{2}\frac{\alpha_{clock}}{h} \left\langle E^2 \right\rangle_T [1 + \eta_{clock}(T)] \tag{4.5}$$

---

[1] Net radiated flux per unit solid angle, per unit projected area, per unit frequency. $(\mathrm{W} \cdot \mathrm{m}^{-2} \cdot \mathrm{sr}^{-1} \cdot \mathrm{Hz}^{-1})$

where $\alpha_{clock} \equiv \alpha_e(0) - \alpha_g(0)$ is the differential *static* polarizability between the two clock states $^3P_0$ and $^1S_0$, h is Planck's constant, $\langle E^2 \rangle_T$ is the mean-squared time-averaged electric field intensity in a BBR environment of absolute temperature T, and $\eta_{clock}(T) \cong \eta_1(T/300K)^2 + \eta_2(T/300K)^4$ is a small dynamic correction to account for frequency dependence of atomic state polarizabilities across the BBR spectrum [7, 102]. Ultimately quantifying the BBR shift in our ytterbium lattice clock requires: (1) knowledge of the static atomic polarizability, (2) knowledge of the dynamic correction factor, and (3) knowledge of the physical BBR environment, given by absolute temperature T.

4.2 Ytterbium atomic polarizability

The shifting and splitting of spectral lines in atomic spectra due to the influence of an external electric field, $\vec{E}$, was one of the first investigations in atomic physics. Formally this interaction is known as the Stark effect. Generally, atomic energies of the lowest-lying electronic quantum states reduce in an electric field by $\frac{1}{2}\alpha_n \langle \vec{E} \rangle^2$ where α_n is defined as the state's static polarizability. The scaling is second order in $\vec{E}$, because $\vec{E}$ is responsible for inducing, as well as interacting with, an atomic dipole moment.

Our first investigation of the BBR shift focused on quantifying the net *static* Stark effect on the clock states in ytterbium. This originally represented the largest uncertainty in the BBR shift because previous knowledge of $\alpha_{|2\rangle}, \alpha_{|1\rangle}$ for ytterbium's clock states was only theoretical and limited to 10% uncertainty due to its many electron complexity [102, 39, 100]. Specifically, we are interested in the differential static polarizability $\alpha_{clock} = \alpha_{|2\rangle} - \alpha_{|1\rangle}$, because any common mode shift due to BBR in $^1S_0$ and $^3P_0$ states can be neglected. The procedure for measuring α_{clock} is straight forward: apply a well defined $\vec{E}$ and measure the change in clock frequency, $\Delta\nu$, shifted by $\frac{1}{2}\alpha_{clock} \langle \vec{E} \rangle^2$. For a direct measurement, we constructed an in-vacuum parallel plate capacitor around our lattice-trapped ytterbium atoms in the existing experimental system [58]. In the parallel plate capacitor limit, applying a voltage, V, creates a well defined, uniform electric field ($\vec{E} = \frac{V}{d}$, where d is electrode separation). The capacitor electrodes were composed of rigidly spaced,
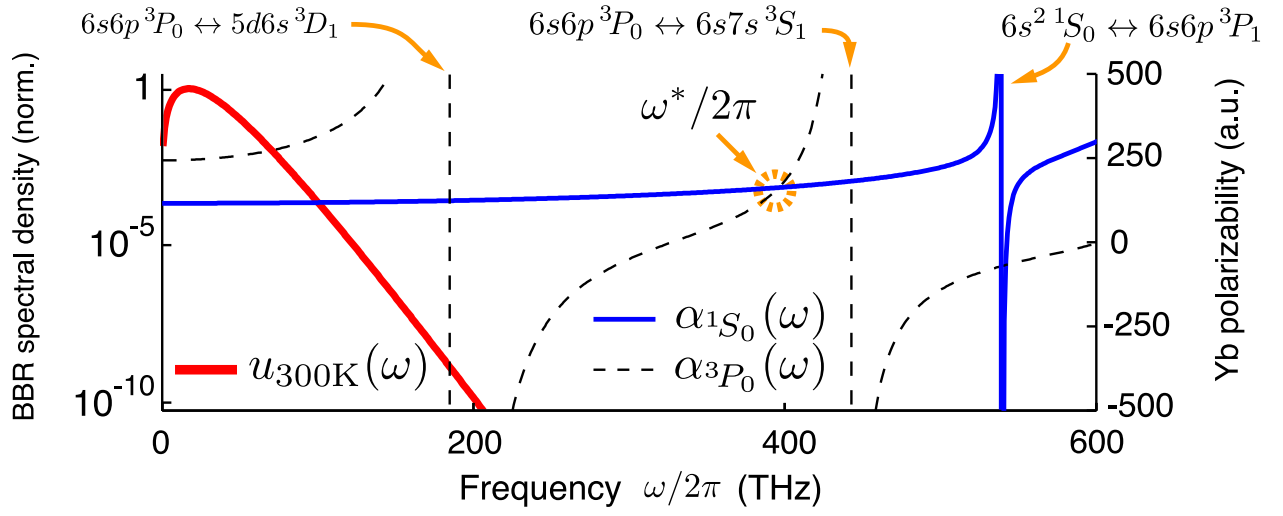
Figure 4.1: Blackbody spectral energy density as a function of radiation frequency (solid red). Also shown are the ${}^3P_0$ (back dash) and ${}^1S_0$ (solid blue) state polarizabilities. The magic wavelength used by our optical lattice dipole trap, where ${}^1S_0$ and ${}^3P_0$ match, is at frequency ω^*.

parallel fused-silica cylindrical plates [101.6(1) mm in diameter, with better than $\lambda/10$ flatness] with a transparent indium-tin-oxide (ITO) conductive coating on the inner surfaces [58]. The electrode separation, $d = 15.03686(8)$ mm, was determined interferometrically by measuring the real time free spectral range (fsr) of four planar etalons formed between the inner silica plates by off axis, 90% reflective metallic pads (33 nm gold on 2 nm chromium) deposited over the inner electrode faces. Specially separated measurements of d constrained electrode parallelism to $\theta_{wedge} < 7$ μrad. Additional numerical modeling of the electrodes confirmed that electric field deviations from the infinite-parallel plane capacitor model were bounded at the 10^{-6} (1 ppm) level by designing a large electrode diameter-to-spacing ratio, ensuring a high degree of parallelism, and centering the atoms radially within the electrodes. Perturbations due to dielectric and conducting mounting structure contribute similar amounts of field uncertainty.

To apply a voltage we constructed a regulated source producing 100 V-1050 V with 1×10^{-6} instability over 1 s - 1000 s with a measurement uncertainty at the 16 ppm level [56]. A 100 ms π-pulse of 578 nm light excites atoms from $^1S_0$ to $^3P_0$ with Fourier-limited clock linewidth of ~ 10 Hz. We record the clock transition frequency relative to our optical local oscillator (LO) in three independently locked interleaved voltage conditions: $\Delta\nu_A$ - Both plates grounded, $\Delta\nu_B$ - Top plate high voltage, Bottom plated grounded, $\Delta\nu_C$ - Top plated grounded bottom plated high voltage. The quadratic Stark shift is then given by

$$\Delta\nu = \frac{1}{2}(\Delta\nu_B + \Delta\nu_C) - \Delta\nu_A \tag{4.6}$$

Reversing $\vec{E}_a$, the applied electric field, reveals information about stray electric fields, $\vec{E}_s$, parallel to $\vec{E}_a$. The difference $\Delta\nu_B - \Delta\nu_C = 2\alpha_{clock}\vec{E}_a \cdot \vec{E}_s$ was measured to be $\vec{E}_s \approx 0.1$ V/cm. However, truly static $\vec{E}_s$ fields subtract completely in Equation 4.6. Varied voltage 'relaxing time' yielded no time dependance on $\vec{E}_s$ over relevant applied fields. Figure 4.2 shows the observed quadratic clock frequency shift as a function of $\vec{E}_a$. Fitting the data to a polynomial we found no quartic, cubic, linear, or offset terms, consistent with an ideal Stark shift in nondegenerate perturbation theory.
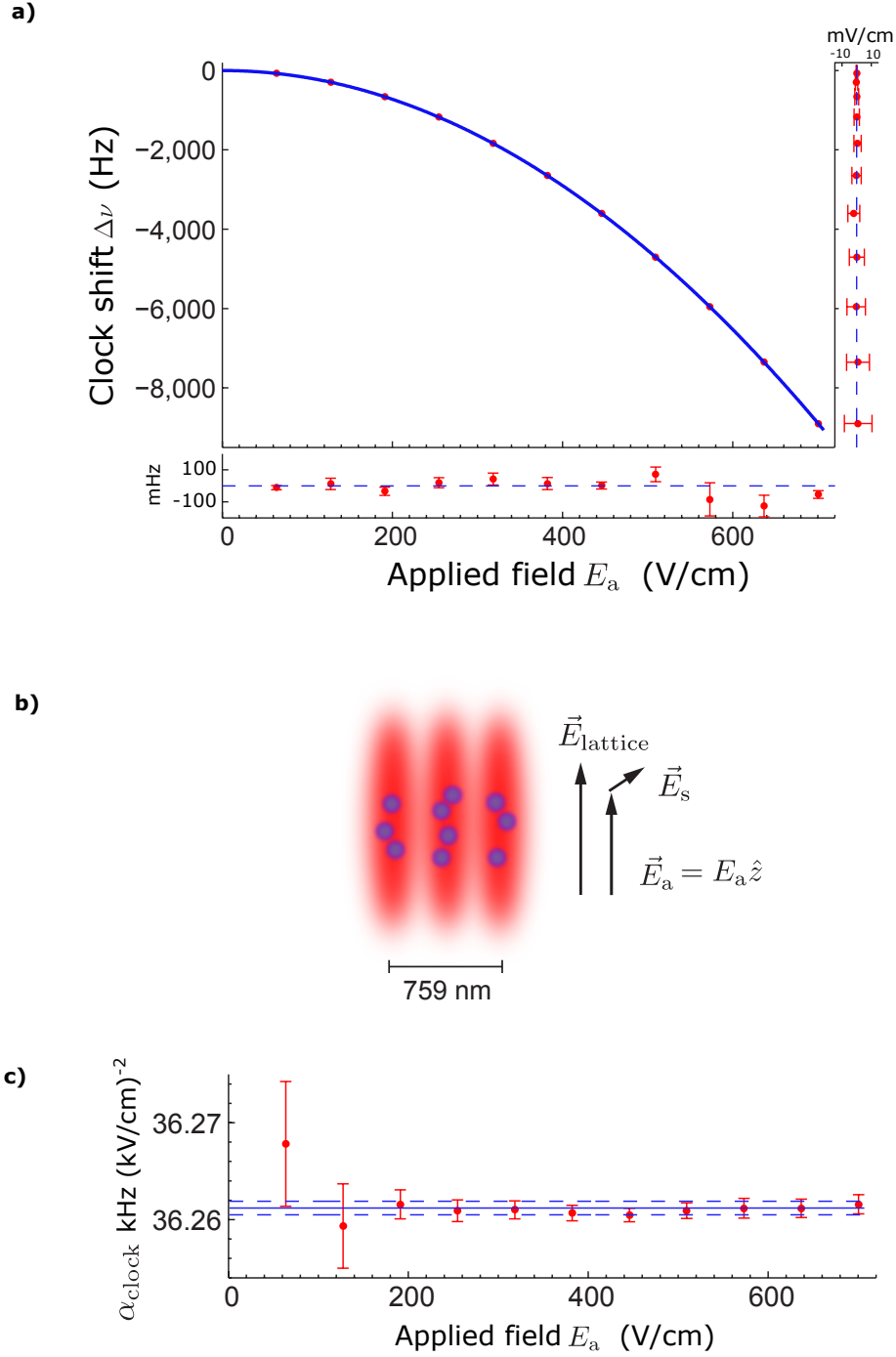
Figure 4.2: (a) Shift in ytterbium clock frequency, $\Delta\nu$, with applied electric field. Residuals of a quadratic fit $\Delta\nu = -\frac{1}{2}\alpha_{clock}\vec{E}^2$ in $\Delta\nu$ (below) and E_a (right). (b) Depicts the relative orientations of $\vec{E}_{lattice}$, $\vec{E}_a$, and hypothetical static stray field $\vec{E}_s$ relative to lattice trapped atoms. (c) Displays the computed α_{clock} at each $\vec{E}$. Error bars represent combined statistic an systematic uncertainties. Solid line shows a finial waited average α_{clock} with dashed lines indicating standard error.

Figure 4.2 also plots the polarizability inferred at each $\vec{E}_a$. Taking the mean of all measurements, weighted by the total standard errors, we determine $\alpha_{clock} = 36.2612(7)$ kHz(kV/cm)$^{-2}$, in good agreement with previous theoretical results. No inhomogeneous line broadening was observed with increased shift, so the statistical uncertainty was reduced with increasing $\Delta\nu$. However, the uncertainty of the applied voltage (the dominant systematic uncertainty) was limited by the performance of available commercial voltmeters.[2] We ensured that our systematics were well controlled with

Table 4.1: Uncertainty budget for α_{clock} measurement. Errors on E_a contribute twice the uncertainty and is included in the tabulation below. Total uncertainty in α_{clock} is from the quadrature sum.

Uncertainty Source	$\times 10^{-6}$	Notes
Clock frequency errors:		
Shift statistical error	8.3	$\Delta\nu = $ -3603.77(3) Hz (1800 s averaging
Higher-order Stark shifts	0.01	
Electric field (E_a) errors:		E_a= 445.836(4) V/cm
Voltmeter systematic	16.4	Regulated 670.3966(55) V
R_{leak} voltage division	0.1	I_{leak}=2.1 nA; 20 kΩ leads
Finite electrode size	1	Atoms centered $\pm$10 mm
Electrode parallelism	4	$\theta_{wedge} < 7$ μrad
Electrode deformation	0.8	Warping of fused silica by gravity
Dielectric spacers	2	Perturbation of ideal field due to three fused silica posts
Spacing d (statistical)	1.6	$N_f > 17000$ fringes spanned
Spacing d (systematic)	9	Fringe centering, wave meter accuracy, stray etalons, stability
Etalon probe tilt, ϕ	0.3	(1-$\cos\theta$) error, $\phi \ll 0.5$ mrad; retro-coupling single-mode fiber
Yb thermal beam	0.06	Dielectric ($\epsilon_r - 1) \sim 8 \times 10^{-9}$
Stray fields, static	0.04	Uncertainty in $\vec{E}_a$ reversal
Stray fields dynamic	2	$\Delta\nu$ correlation with τ_ν
Total uncertainty in α_{clock}	21	

the application of $\vec{E}_a$. No systematic effect resulted from varying the lattice intensity or polarization. Contamination from higher third order and fourth order effects due to mixing of $\vec{E}_a$ with the optical lattice appear at the 10^{-9} fractional error in α_{clock} at high $\vec{E}_a$ [106]. Vector and tensor

---

[2] Voltmeter measurement uncertainty increases at high voltages

Stark shifts are absent as BBR has no net polarization and our clock transition has limited total angular momentum ($I = \frac{1}{2}$). We ensured constant atomic density with application of $\vec{E}_a$ preventing contamination α_{clock} from the cold collision shift. By alternate interrogation of $m_F = \pm\frac{1}{2}$ spin states we observed no magnetic field dependance on $\vec{E}_a$. Finally, to test for stray charge buildup we recorded $\Delta\nu$ while varying the electrodes between grounded and floating configurations, measuring a null result. Table I lists the sources of measurement uncertainty for α_{clock}. The differential static polarizability component in the BBR shift was determined to a 5×10^{-20} fractional clock uncertainty, four orders of magnitude improved over previous theoretical values.

4.3   Dynamic blackbody correction factor

The polarizing effect of BBR largely mimics that of a static electric field due to the low frequency nature of BBR relative to optical transitions in ytterbium. However, accurate knowledge BBR radiation requires understanding of ytterbium's response to time varying BBR, represented by $\eta_{clock}(T)$ in Equation 4.5.[3] Recalling Figure 4.1, the strongest overlap of BBR spectral density is with a single electronic dipole transition, 6s6p$^3P_0$-5d6s$^3D_1$. Indeed, over 90% of $\eta_{clock}(T)$ depends on the electronic dipole coupling between $^3P_0$ and neighboring $^3D_1$ [102]. As a result, the relatively complex problem of computing Equation 4.3 largely reduces to determining a single electronic dipole matrix element, $D \equiv \left| \langle 6s6p^3P_0 | \mathbf{D} | 5d6s^3D_1 \rangle \right|$. In an effort to compute $\eta_{clock}(T)$, we take a fluorescence radiative lifetime measurement of $^3D_1$ via the cascade decay 5d6s $^3D_1 \rightarrow$ 6s6p $^3P_1 \rightarrow$ 6s^2 $^1S_0$ (see Figure 4.3). Applying the Wigner-Eckart theorem to a closed two level system we can write atomic spontaneous emission in terms of Clebsch-Gordan coefficients and the reduced matrix element, $\langle g, J | \mathbf{D} | e, J' \rangle$ as [24]

$$\frac{1}{\tau} = \frac{\omega_0^3}{3\pi\epsilon_0\hbar c^3} \frac{|\langle g, J | \mathbf{D} | e, J' \rangle|^2}{2J' + 1} \tag{4.7}$$

---

[3] $\eta_{clock}(300K) < 0.02$

where J' is the total orbital angular momentum of the excited state and $\omega_0/2\pi$ is the radiated frequency. Rewriting for multiple state decay, given by the branching fraction ζ_0, and solving for our electronic dipole matrix element we find

$$D^2 = 3\pi\epsilon_0\hbar c^3 \zeta_0 \frac{(2J+1)}{(\omega_0^3 \tau_a)}. \tag{4.8}$$

We compute the excited state branching fractions from matrix elements (assuming perfect LS coupling) and energy level separations, yielding a $^3D_1 \to\, ^3P_1$ branching factor of $\zeta_0 = 0.638(10)$. Atoms excited to $^3D_1$ emit an infrared photon followed by a 556 nm photon producing a florescence signal flowing the double exponential decay:

$$y(t) = A \times \Theta(t-t_0) \left[e^{-(t-t_0)/\tau_a} - e^{-(t-t_0)/\tau_b} \right] + y_0 \tag{4.9}$$

where τ_a is the radiative lifetime of $^3D_1$, τ_b is the radiative lifetime of $^3P_1$ ($\tau_b > \tau_a$), A is a normalization scaling factor, y_0 is an offset term, and $\Theta(t-t_0)$ is the Heaviside unit-step function accounting for rapid atom excitation to $^3D_1$ at t_0 [20, 24]. Collecting scattered photon decay then fitting the fluorescence data to Equation 4.9 will give τ_a and ultimately D. Other states populated by decay ($^3P_0$ and $^3P_2$) are long lived compared to our florescence decay times, limiting unwanted ^3P_j florescence. We note that $^3D_1$ state depletion via different decay channels only effects normalization of Equation 4.9, *not* measured τ_a.

To populate atoms in $^3D_1$, we operate our clock in the normal sequence, exciting atoms to the long-lived $^3P_0$ with a resonant 'π-pulse' of 578 nm light. Then, a brief (25 ns) resonant pulse of 1388 nm light excites > 50% of $^3P_0$ atoms to $^3D_1$. Because 556 nm photons are technically easier to detect, we employ a dichroic filter in our normal collection system to extract the decay florescence, sending radiated 556 nm photons to an additional photo-multiplier tube (PMT). An event counter accumulates the arrival times of PMT signals corresponding to single 556 nm photons into 5 ns bins. Typically we observe $N_{atoms} \times (1.5 \times 10^{-5})$ green photons per excitation (assuming $\sim 0.1\%$ collection efficiency). Low photon count allows single emission detection and negligible saturation
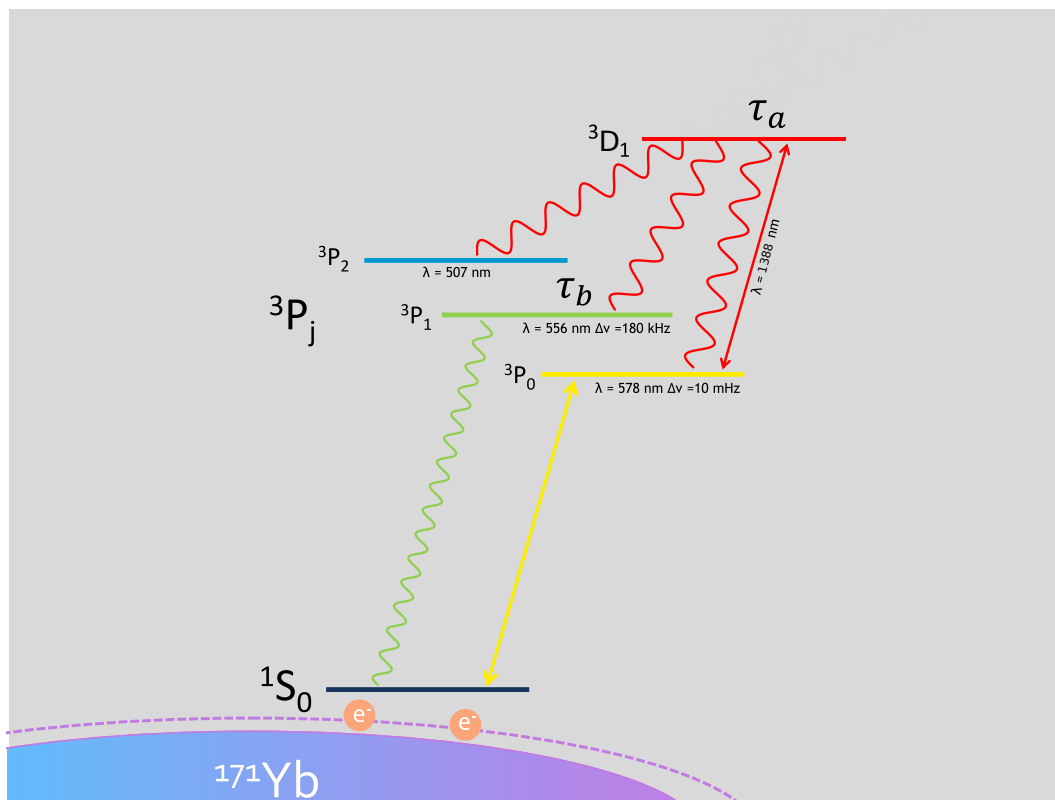
Figure 4.3: Relevant Yb atomic energy levels for the $^3D_1$ lifetime measurement. A florescent radiative lifetime measurement of $^3D_1$ was measured via the cascade decay 5d6s $^3D_1 \rightarrow$ 6s6p $^3P_1 \rightarrow$ 6s^2 $^1S_0$
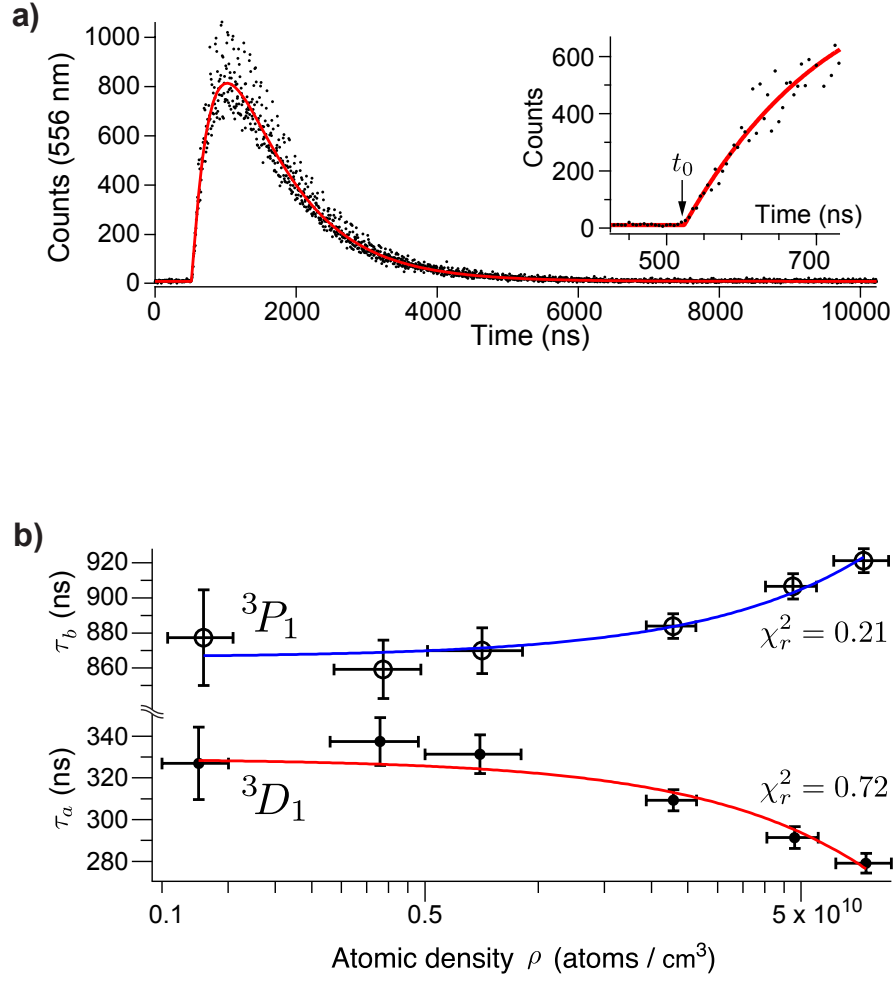
Figure 4.4: (a) Typical 556 nm florescence data from ytterbium atoms excited to $^3D_1$ following the double exponential decay 5d6s $^3D_1 \rightarrow$ 6s6p $^3P_1 \rightarrow$ 6s^2 $^1S_0$. (b) Observed lifetimes vary with atomic density, ρ. Curves are are linear regression fits. Error bars represent one sigma uncertainties.

of high resolution event counter binning. After ~ 1 ms the decay process is complete and we repeat the excitation process. Atoms are excited approximately 200 times before we reload the atomic sample, limited by photon scattering, background gas collisions, and accumulation of atoms to $^3P_2$. After data collection, we fit our fluorescence signal to Equation 4.9. With sufficiently high counts per bin covariance between A, τ_a, and τ_b is negligible. By varying atomic density ρ excited to $^3D_1$, we investigate atomic interaction induced effects on τ_a and τ_b. At high ρ we find that τ_a *decreases* and τ_b *increases*, requiring extrapolation to zero ρ for natural decay times. As quenching of τ_a due to cold collisions and lattice scattering was negligible, we suspect the presence of some other atomic interaction physics such as collective emission (super radiance, sub radiance) or radiation trapping. Further investigation is warranted but beyond the scope of the BBR investigation. We find the radiated lifetimes $\tau_a = 329.3 \pm 7.1$ ns and $\tau_b = 866.1 \pm 7.4$ ns. Table 4.2 gives the measurement uncertainties of τ_a and τ_b.

Table 4.2: Uncertainty budget for lifetimes τ_a, τ_b. Uncertainty from atomic interaction is statistically limited by extrapolations to zero atomic density. Covariance fit biases and distortions due to Zeeman oscillations are estimated from Monte-Carlo simulations. Uncertainties due to 1388 nm pulse duration and stray light are statistically limited. Total uncertainty is given as the quadrature sum.

Uncertainty Source	τ_a (ns)	τ_b (ns)
Atomic interactions	4.3	3.3
Fit biases	0.9	1.5
Zeeman quantum beats	3.0	3.0
1388 nm finite excitation	3.3	4.3
1388 nm stray light	3.4	4.6
Event counter timing	0.2	0.4
Total uncertainty	7.1	7.4

To this point, we have only described the dominant electric dipole (E1) coupling to the BBR field. Additionally, atoms couple to the BBR field via magnetic dipole (M1) and higher multipolar (E2, M2,...) interactions. For room temperature BBR, M1 dipole coupling in alkaline earth-like atoms *could* cause fractional frequency shifts at the 10^{-18} level [102]. However frequency shifts

resulting from higher multipolar (E2, M2,...) terms were shown to yield fractional shifts below 10^{-18} for alkaline earth-like atoms. As such we evaluated the M1 dipole shift in ytterbium for room temperature BBR. Mathematically the M1 BBR shift is analogous to the E1 shift, where ΔE_n is given by Equation 4.3 but with a frequency dependent *magnetic* polarizability, $\alpha(\omega) \rightarrow \beta(\omega)/c^2$ and dipole operator, μ. The M1 shift is evaluated by assuming the non-relativistic limit and an absence of configuration mixing between states, specifically, $\mu = -\mu_B(L + 2S)$ where L and S are orbit and spin angular momentum respectively. Of particular interest is a low-frequency M1 transition, $^3P_0$-$^3P_1$ in the ^3P_j fine structure manifold which accounts for a majority of the M1 shift.[4]   With the above approximations my colleague K. Beloy evaluated Equation 4.3 analytically to find the energy shift from the $^3P_0$- $^3P_1$ matrix element, then expressed it as an additional contribution to $\eta_{clock}(T)$. The M1 BBR shift to the $^3P_0$ clock level is found to be $\eta_{clock}^{(M1)}(300K) \approx 1 \times 10^{-5}$, indicating that ytterbium M1 coupling to the BBR field is negligible at room temperature.

To complement our radiative lifetime measurement, we independently compute D via a semi-empirical technique by combining existing ytterbium polarizability data with atomic theory [12]. We report the reduced matrix element D to be 2.77(4) a.u. and 2.80(7) a.u. for our experimental determination and semi-empirical calculation respectively [12]. Additional work conducted shortly after our decay measurement featuring *ab initio* theoretical treatment was in good agreement with our findings [108]. Assuming an ideal BBR environment at 300 K we can evaluate Equation 4.3 making the substitution of $\alpha_n(\omega) \rightarrow \alpha_{clock} + (2/3\hbar)(D^2/\omega_0^3)\omega^2$. Taking the weighted mean of all reported reduced diple matrix results, and integrating over ω we find $\eta_{clock}(T)$ to be:

$$\eta_{clock}(T) = 0.0173(5)\left(\frac{T}{300\ K}\right)^2 + 0.0006\left(\frac{T}{300\ K}\right)^4 \tag{4.10}$$

with a fractional clock frequency uncertainty from the dynamic correction to BBR of $< 1.0 \times 10^{-18}$.

---

[4] μ is an even-parity operator, where $\mathbf{D}$ is an odd-parity operator

4.4   Defining the blackbody environment

An imprecise knowledge of the BBR environment prevents quantifying the characteristic temperature, T, contained in $\langle E^2 \rangle_T \left[1 + \eta_{clock}(T) \right]$ from Equation 4.5. To overcome this issue we constructed a passive, room temperature, in-vacuum radiation shield that furnishes a uniform, well-characterized BBR environment for clock spectroscopy. Here we describe the construction of our BBR shield with a defined radiation environment corresponding to fractional ytterbium clock uncertainty contribution of 5.5×10^{-19}.

4.4.1   The blackbody radiation shield

The BBR shield, shown in Figure 4.5, possesses a number of important features to approximate an ideal blackbody environment. The experimental requirements of our shield are as follows: it must possess excellent temperature uniformity, accommodate the collection, cooling and trapping, interrogation, and state-detection of the atoms, prevent static Stark shifts from stray charges that might accumulate on the vacuum apparatus, limit atom exposure to uncharacterized BBR, and provide an accurate absolute temperature reading. The bulk material of our shield is constructed from thermally conductive copper stock. Two apertures on opposing sides of the shield allow a collimated thermal beam of atoms to pass through the central region, providing a source for the lattice-trapped sample. Additionally, six 2.54 cm countersunk insets accommodate round glass windows for optical laser cooling and trapping of our atomic sample. A seventh window inset is used for PMT detection of lattice trapped atoms. While the glass windows are nearly opaque to room-temperature BBR, they are highly transmissive and anti-reflection coated for the appropriate ytterbium laser wavelengths. Because the shield apertures allow outside radiation to enter the shield, we apply a high-emissivity, carbon nanotube coating to all internal surfaces of the shield body to minimizing reflections and maintain a well defined radiation environment. All internal shield surfaces are conductive and grounded, protecting the clock atoms from stray

charge that might accumulate on the vacuum apparatus [80]. The copper construct provides a naturally conductive surface where the recessed windows have a transparent ITO layer. The black carbon nanotube coating has low resistance and is in good electrical contact with the surrounding highly conductive copper shield. To frustrate Eddy currents in the copper, we split the shield in half with an electrically insulative, thermally conductive thin spacer. The shield construction is held together with boron nitrite retaining rings placed on the upper and lower sections of the copper halves. Approximately five calibrated platinum resistance temperature detectors (RTDs) distributed throughout the shield provide an accurate, real-time measure of the shield's absolute temperature, T. The final shield sits thermally isolated on four PEEK plastic support posts inside ultra-high vacuum (UHV) at 2×10^{-9} torr.

4.4.2 Characterizing blackbody temperature inhomogeneities

In normal operation, the BBR shield has high temperature uniformity afforded by its copper construction. However, passively coupled BBR from the surrounding environment via conductive and radiative heat transfer along with BBR window leak-through can cause small temperature inhomogeneities. To account for departures from an isothermal environment, my colleague K. Beloy developed the following model for the BBR shield. The internal surfaces of the shield and windows are modeled as opaque, diffuse, graybody surfaces having temperature-independent emissivities. We accurately portray the shield apertures by creating two circular blackbody surfaces matched to the aperture size and blackbody characteristics. Collectively these surfaces fully enclose the atoms residing in the center of the shield. The effective temperature at the center, T_{eff}, is given by the local field energy density, u, a superposition of surrounding radiating surfaces as derived from the Stefan-Boltzmann law:

$$T_{eff}^4 = \frac{c}{4\sigma}u = \sum_i \left(\frac{\Omega_i^{eff}}{4\pi} T_i^4 \right) \tag{4.11}$$

where c is the speed of light, σ is the Stefan-Boltzmann constant and the index i runs over all surfaces where T_i is the temperature and Ω_i^{eff} is the effective solid angle of surface i. We assign
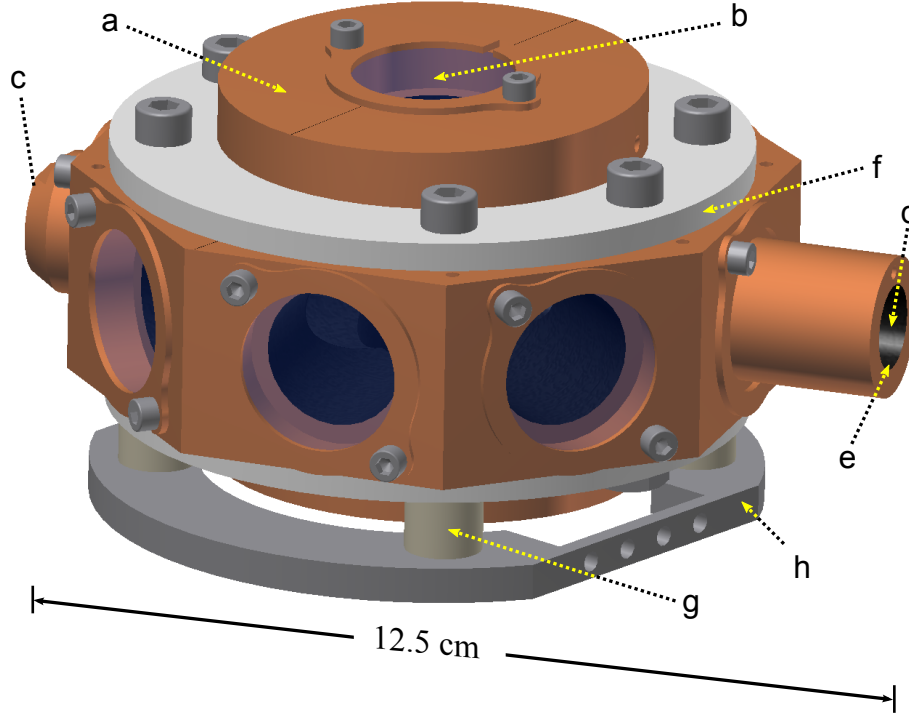
Figure 4.5: CAD rendering of the radiation shield installed in our ytterbium lattice clock from modeling done by K. Beloy. Features include (a) copper bulk material (b) BK7 glass windows with AR coatings (c) atomic thermal beam entry and (d) exit aperture (e) carbon nanotubed coating (f) boron nitride retaining rings (g) PEEK plastic posts and (h) vacuum system support plate (stainless steel). BBR shield is only connected to the vacuum system through PEEK supports and rests entirely in ultra high vacuum.

an 'effective solid angle' to surfaces to assess the dependance of u to individual surface radiation. For example, if our shield was completely reflective to BBR, an infinitely small geometric opening would define the effective temperature at the atoms (Ω_i^{eff} subtending all space). In the limit of a completely black (unit-emissivity) enclosure, Ω_i^{eff} reduces to the geometric solid angle subtended by surface i as perceived by the atoms. Effective solid angles are non-negative, depend on the geometry and emissivity of all enclosure surfaces, and satisfy the normalization $\sum_i \Omega_i^{eff} = 4\pi$. We compute effective solid angles for our shield enclosure with a finite element radiation analysis, constructing a model enclosure with new Ω_i^{eff} solid angles. Introducing a small blackbody sphere, or probe, centered in the shield we calculated the BBR effective temperature, T_e, as governed by radiative
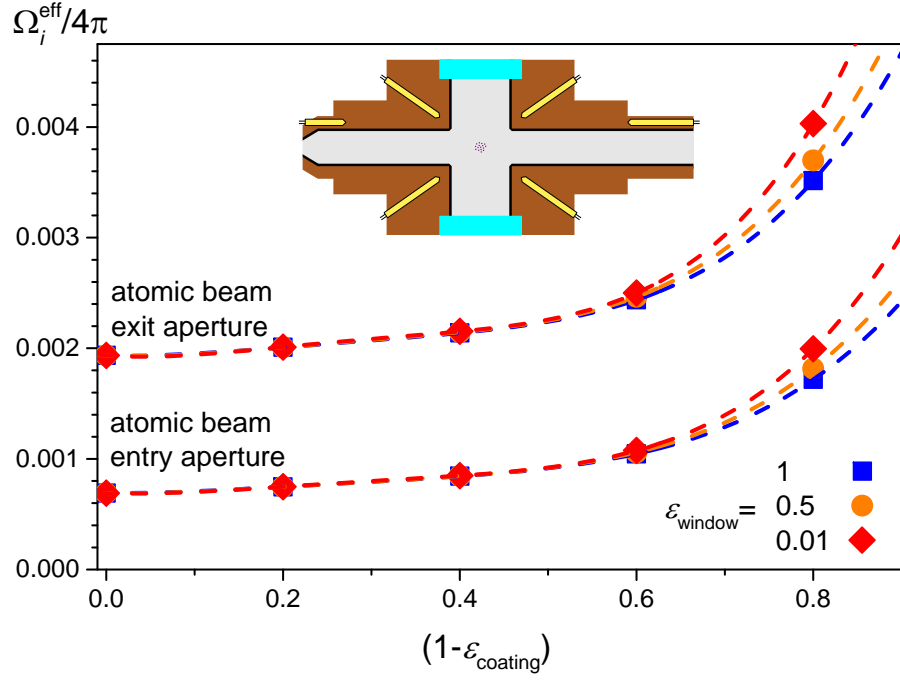
Figure 4.6: Finite element radiation analysis of effective solid angles for atomic beam entry and exit apertures with different window emissivity. ϵ denotes emissivity value. The inset diagram displays a two-dimensional cross section of the blackbody radiation shield, with entry and exit apertures on the left and right respectively. Top and bottom windows are illustrated as light blue substrates and the yellow cylinders represent RTDs embedded in the shield.

photon exchange with the molded finite element enclosure [1]. Calculating the probe temperature for different input configurations of the surface temperatures and emissivities allows extraction of individual Ω_i^{eff} from Equation 4.11. Highlighted in Figure 4.6 are the entry and exit apertures Ω_i^{eff} as a function of various combinations of coating and window emissivities. Importantly, for a perfectly black coating, both the Ω_i^{eff} are independent of the window emissivity and reduce to their respective geometric solid angles because, by design, the apertures are not permitted direct line-of-sight to the windows. As the coating emissivity departs from unity, Ω_i^{eff} increase while acquiring a dependence on window emissivity. Also seen in Figure 4.6 is largely constant Ω_i^{eff} over a range of moderately-high coating emissivity. This illuminates a two-fold advantage in using a high-emissivity coating: (i) it minimizes the overall influence of BBR entering through the apertures and (ii) it minimizes the sensitivity to exact emissivity values. For the interior shield body surfaces, we employ a high emissivity coating that consists of multi-wall carbon nanotubes [71, 70]. The coating is highly-thermally and -electrically conductive with a surface emissivity measured to be $\epsilon_{coating} > 0.8$ for wavelengths from visible to 20 μm.[5]   With the above data and a high emissivity coating, we can equate our modeled effective solid angles to the shield geometric solid angles, with the finite element analysis providing a means to gauge corresponding environment uncertainties.

4.4.3   Measuring absolute temperature

After characterization of inhomogeneities in the ideal BBR environment a special effort must be made to measure the absolute temperature, T, of the BBR shield. While some systematics can be absolutely calibrated with the atoms, there is no means to detect absolute temperature with the clock atoms. Thus we employ highly precise, calibrated platinum resistance temperature detectors (RTD)s to provide a real time measure of the shield's absolute temperature. After a thermal-cycling process, a NIST-traceable absolute temperature calibration is performed on each RTD by the manufacturer. The simultaneous use of many (up to seven) sensors for temperature

---

[5] This is done by hemispherical reflectance measurements linked to a NIST blackbody standard

measurement aids in the detection of calibration shifts and sensor reading errors. For high accuracy resistance evaluation we adopt the four wire resistance measurement technique. Self-heating from ohmic dissipation of the RTD sense current can be meaningful, especially in vacuum where thermal transfer from the platinum wires is significantly reduced. We have directly measured self-heating of 7 K/mW, which for our low sense current (96 μA into 109 Ω) yields an effect of 7 mK. Reduced thermal transfer from the platinum wires also enables parasitic heat flow through the RTD leads. To counter these effects, a thermally-conductive (but electrically-insulative) epoxy covers the entire RTD and its leads, making excellent thermal contact between the shield and all parts of the sensor. Window temperatures are not directly measured in real-time to maintain optical access to the atomic sample. A thin carbon-loaded polyimide layer provides a high but finite thermal contact between the glass-copper contact leading to some window temperature uncertainty. We measure the temperature conductance from the window substrates to copper shield by temporarily fitting a temperature sensor and heater to a glass substrate, then record the shield temperature as a function of heater power. We found the measured temperature discrepancy between the window and shield leads to a clock uncertainty of 3×10^{-19} at room temperature. Additionally, BK7 windows are also weakly transparent to BBR radiation but we find this correction factor to be negligible provided both the shield and surrounding apparatus are at similar temperatures.[6]

4.4.4   Blackbody radiation shift uncertainty

Table 6.1 summarizes the BBR shift uncertainties for our ytterbium lattice clock. In addition to items that have been described so far, we note that variations in the position of the lattice-trapped atoms from the geometric center of the chamber, non-scalar Stark shifts from anisotropy in the BBR, and the application of T_{eff} in the dynamic correction, all leading to comparatively small uncertainties. Table 6.1 is divided into BBR environmental uncertainty, ytterbium atomic response uncertainty, and total BBR ytterbium clock uncertainty. All reported uncertainties are in

---

[6] BK7 is mostly transparent to radiation below 3 μm and weakly transparent ($< 1\%$) to radiation above 3 μm.

fractional clock frequency units and result from the quadrature sum of component uncertainties. We find a total uncertainty associated with the BBR environment to be 5.5×10^{-19}. The reported dynamic correction η_1 is taken as the weighted average of three distinct determinations of its value [12, 108]. Magnetic dipole (M1) interaction with the BBR leads to a clock shift of $\sim 3 \times 10^{-20}$, with a small uncertainty included in the atomic response factor. Finally, combining the BBR environment and atomic response uncertainties yields a total uncertainty for the BBR shift given by Equation 4.5 of 1.0×10^{-18}.

Table 4.3: BBR shift uncertainty in fractional clock frequency at room temperature operation (~ 296.7 K).

BBR environment	$\times 10^{-19}$
RTD temperature measurements	
manufacturer calibration (5 mK)	1.6
post-calibration fidelity	2.4
digital multimeter (4-wire)	2.2
self heating	1.6
parasitic conduction/radiation	0
Temperature inhomogeneity/effective solid angles	
BK7 glass windows	2.9
entry aperture (oven shielded by shutter)	2.4
exit aperture	0.3
Other	
application of T_{eff} in dynamic correction	0.1
residual transmission through windows	0.2
atomic position/dimensional tolerances	0.5
BBR anisotropy (non-scalar Stark)	0
Total BBR environment uncertainty	5.5
Atomic response	$\times 10^{-19}$
dynamic correction η_1	8.5
dynamic correction η_2	0.4
BBR Zeeman (M1) factor	0.1
Total atomic response uncertainty	8.5
Total BBR clock shift uncertainty	1.0×10^{-18}

4.5   Direct measurement of the blackbody Stark shift

Since the determination of the blackbody environment plays such a critical role in the final uncertainty budget of a 10^{-18} level optical lattice clock, it is imperative to experimentally validate our treatment of this effect. To this end, we heat the BBR shield to directly observe the temperature dependence of the BBR shift. In principle, this measurement could be used to determine the atomic response parameters, α_{clock} and $\eta_{clock}(T)$ in Equation 4.5. However, since these parameters have been independently determined to a high level of accuracy, here we make the more meaningful comparison between measured and expected BBR shift as characterized by T_{eff}. To uniformly heat the copper shield we fit annulus-shaped resistive heaters on the top and bottom of the copper mass, nested below the boron-nitride holding rings. This enables us to raise the shield temperature by up to 100 K above room temperature during operation of the lattice clock. We operate two Yb lattice clocks and make direct frequency measurements between them. One lattice clock is fitted with the BBR shield and heaters, while the second serves as an optical frequency reference. The uncharacterized ambient BBR environment within the second system is known to be sufficiently stable over the course of a measurement (several hours). While comparing the atomic clock frequencies, we gradually raise the temperature of the BBR shield of the first clock and then allow the shield to cool to room temperature (1/e time of ∼3 hours). The hottest shield temperature was limited by vacuum degradation, frustrating lattice clock operation. Each BBR data point was a result of binning difference frequency data segments that averaged to a measurement precision of $\sim 3 \times 10^{-17}$. The observed clock shift versus temperature is plotted in Figure 4.7. The results from three distinct measurement protocols are shown: (1) the top curve shows measurement for the case of a slow continuous heating of the shield temperature, (2) the middle curve for the case of controlled intermittent heating to allow the shield to settle at a nearly-constant temperature for each measurement point, (3) and the bottom curve for the case of passive cooling of the shield after a heating cycle. Red solid curves fit the data to Equation 4.5. The temperature of the shield windows closely

follows that of the shield body, with a difference determined by thermal conductance measurements described above together with the estimated radiative heat transfer from its surfaces. While the shield body is heated and subsequently cooled, the apertures expose the atoms to unchanging room temperature BBR. However, given our measurement precision of $\sim 3 \times 10^{-17}$ per point, limited exposure from room temperature BBR gives a negligible systematic effect. Whichever measurement protocol was employed, we ensured that temperature changes were sufficiently slow to avoid any meaningful temperature dependent Doppler shifts.[7]   Also shown in Figure 4.7 is the resulting static polarizability from ten different direct BBR shift measurements. We fix $\eta_1 = 0.01745(38)$ and $\eta_2 = 0.000593(16)$ allowing α_{clock} to be the free parameter.[8]   The weighted mean of the measured differential static polarizability is found to be $\alpha_{clock} = 146.1(1.3)$ a.u., in excellent agreement with static Stark measurements, $\alpha_{clock} = 145:726(3)$ a.u. or $36.2612(7)$ kHz(kV/cm)$^{-2}$.

In conclusion, we demonstrated control and characterization of room-temperature BBR shift at 1×10^{-18} with a radiation shield in an ytterbium optical lattice clock. The resulting BBR shift uncertainty from the thermal environment is 5.5×10^{-19} with an atomic response uncertainty of 8.5×10^{-19} [11]. We note that this level of control is achieved with the simplicity of room-temperature operation, without the special transport of lattice trapped atoms to a cryogenic environment and offers a real time measurement of the BBR shift. Moreover, our shield design is expected to be applicable to optical lattice clocks based on other atomic species. For example, replacing ytterbium inside our shield with Mg, Ca, Sr, or Hg, would yield an uncertainty from the BBR environment of $9 \times 10^{-20}, 6 \times 10^{-19}, 1 \times 10^{-18}$, or 4×10^{-20}, respectively [102, 49]. Finally, our explicit measurement of the BBR shift temperature dependence supports out treatment of this shift at the 10^{-18} level.

---

[7] Specifically, Doppler shifts from optical phase chirps from window thermal expansion or temperature dependent indices of refraction.

[8] This includes additional independent efforts to determine the dynamic correction factor beyond our decay measurement technique.

68
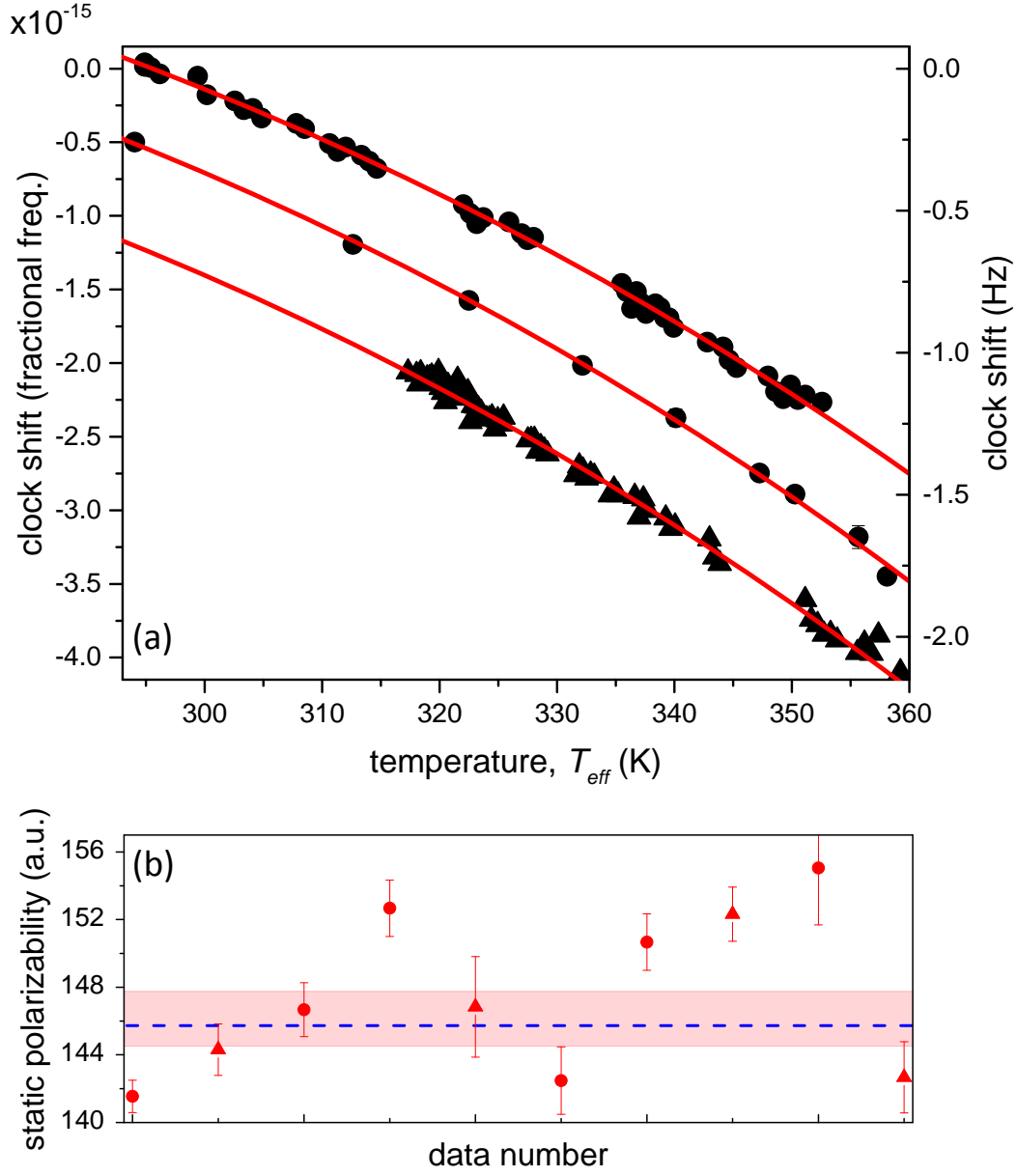
Figure 4.7: Measurement of ytterbium clock frequency shift relative to defined blackbody environment temperature. Upper plot displaying measured frequency shifts for different shield temerature cases with corresponding fit (red solid curve): (a) measured frequency shift for shield heating (dots) and cooling (triangles). Frequency offset was intentionally applied to aid in visual clarity. (b) The extracted differential polarizability value, $\Delta\alpha_{clock}$, from ten measurements of blackbody radiation shift versus temperature. Circles denote heating the shield and tangles denote cooling the shield with $\pm 1\sigma$ weighted standard error given by the red shaded region. The dotted blue line gives the expected result from previous measurement.

Chapter 5

Lattice Light Shifts

Elimination of motional effects is essential for studying ultra-narrow transitions in atomic frequency standards. A quantum oscillator must be fixed in space, insensitive to external perturbations, free from Doppler shifts, atomic collisions, and gravitational acceleration before realizing ultra-precise spectroscopy. The lattice clock achieves these requirements via an engineered light trap or optical lattice potential. The stark shift resulting from this lattice potential on the clock states can exceed 100 kHz to realize sufficient trap depths for containment of cooled clock atoms. However, to reach 10^{-18} clock operation these stark shifts need to be characterized at the 1mHz level. Fortunately lattice clocks have been spectacularly successful at creating trap potentials with near zero net stark shift on an ensemble of atoms. Even the first reported optical lattice clocks realized < 1 kHz, laser limited clock linewidths [125]. Here we study the lattice confinement of ytterbium atoms and our ability to cancel and control lattice induced light shifts for 10^{-18} clock operation.

5.1   Optical dipole potential

Matter exposed to an electric field becomes polarized via the Coulomb force. Classically we express this electric field and matter interaction of an isotropic media as:

$$\vec{\mathbf{d}} = \alpha(t)\, \vec{\mathbf{E}} \tag{5.1}$$

where $\vec{\mathbf{d}} = \vec{d}(\mathbf{r}, t)$ is the induced dipole moment, $\alpha(t)$ represents the polarizability of an object, and $\vec{\mathbf{E}} = \vec{E}(\mathbf{r}, t)$ is the surrounding electric field [47]. The Coulomb force between $\vec{\mathbf{d}}$ and $\vec{\mathbf{E}}$, will result in an interaction energy, expressed as:

$$U = - \vec{\mathbf{d}} \cdot \vec{\mathbf{E}} \tag{5.2}$$

with a net torque about an object's center of mass [47]. In a nonuniform electric field, the object will experience different Coulomb forces across its structure, resulting in an additional nonzero net force. In the case of a *conservative* potential, we can express the force, $\vec{\mathbf{F}}$, from a nonuniform electric field as:[47]

$$\vec{\mathbf{F}} = - \vec{\nabla} U = (\vec{\mathbf{d}} \cdot \vec{\nabla}) \vec{\mathbf{E}} = \alpha(t)(\vec{\mathbf{E}} \cdot \vec{\nabla}) \vec{\mathbf{E}} . \tag{5.3}$$

The above relation reveals several important consequences of controlling matter with an electric field: (1) the net force scales with the object polarizability, (2) a nonzero force requires an electric field gradient, and (3) the force scales with E^2 because the electric field induces, as well as interacts with, a dipole moment. Similarly, an atom confined in an optical lattice experiences an induced atomic dipole moment. Of course, atoms absorb and re-emit photons at specific frequencies, leaving $\alpha(t)$ complex and dependent on electric field frequency.

To calculate the polarizability of an atom, we consider the equation of motion of an electron in an external electric field that is bound (classically) to a potential,

$$\ddot{x} + \Gamma_w \dot{x} + \omega_0^2 x = \frac{-e}{m_e} E(t) \tag{5.4}$$

with ω_0 identified as the atomic transition frequency, and Γ_w is the damping coefficient do to radiative energy loss [48]. We find $\alpha(t)$ to be

$$\alpha(t) = \frac{e^2}{m_e} \frac{1}{\omega_0^2 - \omega^2 - i\omega\Gamma_w}. \tag{5.5}$$

with the imaginary part of $\alpha(t)$ responsible for absorption of energy (re-emitted as dipole radiation, heating the sample) and the real part of $\alpha(t)$ responsible for the interaction potential in Equation 5.2

[48]. The dynamic dipole polarizability can be calculated semi-classically for a two level quantum system however we forgo that derivation here (e.g. [23]).

Careful control in the optical lattice confinement requires the atom-trapping light interaction be well defined and uniform over the quantum ensemble. To this end we construct a 1-D optical standing wave potential providing a simple, near ideal trap for confinement of the ultra cold ytterbium. The optical lattice is formed by interfering high power, counter-propagating, focused Gaussian laser beams of the same mode structure, frequency, and polarization resulting in a time averaged intensity distribution given by:

$$\langle I(r,z) \rangle = \frac{2P}{\pi \omega^2(z)} e^{-\left(\frac{2r^2}{\omega^2(z)}\right)} \tag{5.6}$$

where z is in the direction of laser light propagation, r denotes the radial coordinate, and P is the power in a single direction [54]. Naturally, the $1/e^2$ intensity radius, $\omega(z)$, depends on position relative to the focus, given by

$$\omega(z) = \omega_0 \sqrt{1 + \left(\frac{z}{z_R}\right)^2} \tag{5.7}$$

where ω_0 is the minimum beam radius, and $z_R = \pi \omega_0^2 / \lambda$ gives the Rayleigh length [54]. For dimensions close to the lattice focus we can approximate the electric field as two one-dimensional, linearly polarized, interfering plane waves, creating a standing electric filed wave with frequency ω_L given by:

$$\vec{E}(z,t) = E_0 e^{i(kz - \omega t)} + E_0 e^{-i(kz + \omega t)} \hat{\mathbf{z}}. \tag{5.8}$$

Combining Equation 5.1, Equation 5.2, and Equation 5.5 for an oscillatory field, we find

$$\langle U(r,z) \rangle = -\frac{1}{2\epsilon_0 c} \text{Re}[\alpha(t)] I(r,z) \tag{5.9}$$

where $I(r,z) = 2\epsilon_0 c |\mathbf{E}|^2$ is the field intensity [48]. Around the focus, if we take the averaged value of $\vec{E}(z,t)$ over a period, $\tau = 2\pi/\omega$ we find the trapping potential is modulated sinusoidally according to

$$\langle U(r,z) \rangle = -U_0 \cos^2(kz) e^{-2r^2/\omega_0^2}. \tag{5.10}$$

We define the trap depth for a given state polarizability, α_i, at $U(r = 0, z = 0)$ found to be

$$U_0 = \alpha_i \frac{4P}{c\epsilon_0 \pi \omega_0^2} \tag{5.11}$$

where U_0 accounts for the constructive interference of two identical counter propagating laser beams [48]. From Equation 5.10, for small deviations about the focus we can write the time averaged trapping potential as periodic array of 2-D discus shaped electric field potentials every $\lambda/2$, confined radially by the Gaussian parameters. We can approximate confinement in in the radial and longitudinal directions using the quantum harmonic oscillator potential, $V(x) = \frac{1}{2}m\omega^2 x^2$, where m representing the atomic mass. We find the radial and longitudinal frequencies to be:[6]

$$f_{radial} = \frac{1}{\pi \omega_0} \sqrt{\frac{U_0}{m}} \tag{5.12}$$

$$f_{long.} = \frac{1}{\lambda} \sqrt{\frac{2U_0}{m}}. \tag{5.13}$$

These represent the eigen trap frequencies and, consequently, the energy spacing between motional states of our quantum harmonic oscillator model used to describe our system.

5.2   Frequency shifts in a 1-D lattice trap

The presence of an external electric field results in the shifting and splitting of spectral lines in atomic spectra, altering the frequency of our clock timebase. Critical to reaching the true performance of an optical lattice clock is canceling the > 100 kHz light shifts induced by the off resonant (conservative), electric field trap. The dominate Stark shift when optical trapping is from the atoms' electronic dipole polarizability, α_{E1}. However, by choosing a lattice frequency where α_{E1} of the two clock states match ($\Delta\alpha_{E1}$ is minimized), we engineer a trapping environment that is virtually free of (net) lattice light shifts, preserving the desired natural atomic transition. As lattice clocks reach a level of performance beyond state-of-the-art microwave standards, Stark shifts stemming from higher multipolarizabilities contributions (e.g. magnetic dipole and electric quadrupole) prevent a simple cancellation of the lattice Stark shift. For a harmonic electromagnetic

fields with shared time dependance we can write $\mathbf{E}(\mathbf{x},t)=\text{Re}[Ee^{-i\omega t}]$. The resulting time averaged energy shift is given by:

$$
\begin{aligned}
U \quad = \quad & -\frac{1}{4}(E \cdot E^*)\alpha_{E1}(\omega) \\
& -\frac{1}{4k^2}[(\nabla \times E) \cdot (\nabla \times E^*)]\alpha_{M1}(\omega) \\
& -\frac{1}{2k^2}[\{\nabla \otimes E\}_2 \cdot \{\nabla \otimes E^*\}_2]\alpha_{E2}(\omega) \\
& -\frac{1}{16}(E \cdot E)(E^* \cdot E^*)\beta_{E1}(\omega)
\end{aligned}
$$

(5.14)

where $k = \omega/c$ (c is the speed of light), α_{M1} and α_{E2} are the magnetic dipole and electric quadrupole polarizabilities respectively, and $\{\nabla \otimes E\}_2 \cdot \{\nabla \otimes E^*\}_2$ is a second rank tensor. For our 1-D linearly polarized optical lattice where $\omega_0 >> \lambda$, we model E as

$$
\vec{E} = E_0 e^{(-r^2/\omega_0^2)}\cos(kz)\hat{z}.
$$

(5.15)

However, by Maxwell's equation, $\nabla \times \vec{E} = -\frac{1}{c}\frac{\partial \vec{B}}{\partial t}$, we find the spatial distribution of the magnetic field is 90° out of phase with the electric field, giving the strongest magnetic field gradients at regions of high electric field intensity and weakest magnetic field gradients at regions of low electric field intensity [122]. Consequently, the time-averaged trapping potential felt by each atomic component in $\alpha(\omega_L)$, and $\beta(\omega_L)$, in the direction of tight lattice confinement, is given by:

$$
U_{E1}(z) \quad = \quad -\left(\frac{E_0}{2}\right)^2\alpha_{E1}(\omega)e^{(-2r^2/\omega_0^2)}\cos^2(kz)
$$

(5.16)

$$
U_{M1}(z) \quad = \quad -\left(\frac{E_0}{2}\right)^2\alpha_{M1}(\omega)e^{(-2r^2/\omega_0^2)}\sin^2(kz)
$$

(5.17)

$$
U_{E2}(z) \quad = \quad -\left(\frac{E_0}{2}\right)^2\alpha_{E2}(\omega)e^{(-2r^2/\omega_0^2)}\sin^2(kz)
$$

(5.18)

$$
U_{E1}(z) \quad = \quad -\left(\frac{E_0}{2}\right)^4\beta_{E1}(\omega)e^{(-4r^2/\omega_0^2)}\cos^4(kz)
$$

(5.19)

In general, we can write the total potential as:

$$
U(\omega) = -U_0 a(\omega)e^{(-2r^2/\omega_0^2)}\cos^2(kz) - U_0 a'(\omega)e^{(-2r^2/\omega_0^2)}\sin^2(kz) - U_0^2 b(\omega)e^{(-4r^2/\omega_0^2)}\cos^4(kz) \quad (5.20)
$$

where $U_0 \equiv \left(\frac{E_0}{2}\right)^2 \alpha(\omega*)$ (where $\omega*$ is the magic frequency), and quantities $a(\omega), a'(\omega), b(\omega)$ are atomic properties given by:

$$
\begin{aligned}
a(\omega) &\equiv \frac{\alpha_{E1}(\omega)}{\alpha(\omega*)} \\
a'(\omega) &\equiv \frac{\alpha_{M1}(\omega) + \alpha_{E2}(\omega)}{\alpha(\omega*)} \\
b(\omega) &\equiv \frac{\beta(\omega)}{\alpha(\omega*)}
\end{aligned}
$$

To proceed, we approximated motional sates as decoupled harmonic oscillator states in the $\hat{x}$, $\hat{y}$, and $\hat{z}$ dimension ($r^2 = x^2 + y^2$). Expanding the spatial part of Equations 5.16, 5.17, and 5.19 yields:

$$
\begin{aligned}
e^{(-2\rho^2/\omega^2)}\cos^2(kz) &\approx 1 - (kz)^2 + \frac{(kz)^4}{3} + \left(-\frac{2}{\omega^2} + \frac{2(kz)^2}{\omega^2} - \frac{2(kz)^4}{3\omega^2}\right)\rho^2 \ldots \\
e^{(-2\rho^2/\omega^2)}\sin^2(kz) &\approx (kz)^2 - \frac{(kz)^4}{3} + \left(-\frac{2(kz)^2}{\omega^2} + \frac{2(kz)^4}{3\omega^2}\right)\rho^2 \ldots \\
e^{(-2\rho^2/\omega^2)}\cos^4(kz) &\approx 1 - 2(kz)^2 + \frac{5(kz)^4}{3} + \left(-\frac{2}{\omega^2} + \frac{4(kz)^2}{\omega^2} - \frac{10(kz)^4}{3\omega^2}\right)\rho^2 \ldots
\end{aligned}
\tag{5.21}
$$

taking the form of a quantum harmonic oscillator with higher order corrections. To calculated the lattice trap eigen energies, we express powers of kz and ρ in terms of the raising and lowering operators, a_i and $a_i^\dagger$, and $\xi = \frac{\sqrt{2}}{k\omega}$ to the corresponding to the i-th harmonic mode.

$$
kx = \frac{1}{\sqrt{2}} U^{-1/4} \xi^{-1/2} (a_x + a_x^\dagger) \tag{5.22}
$$

$$
ky = \frac{1}{\sqrt{2}} U^{-1/4} \xi^{-1/2} (a_y + a_y^\dagger) \tag{5.23}
$$

$$
kz = \frac{1}{\sqrt{2}} U^{-1/4} (a_z + a_z^\dagger) \tag{5.24}
$$

For the case of the above Equations:

$$
\langle n_i | e^{(-2\rho^2/\omega^2)}\cos^2(kz) | n_i \rangle \approx 1 - U^{-1/2}\left(n_z + \frac{1}{2}\right) + \frac{1}{2}U^{-1}\left(n_z^2 + n_z + \frac{1}{2}\right) - U^{-1/2}\frac{\sqrt{2}}{k\omega}\left(n_\rho + \frac{1}{2}\right) \ldots
$$

$$
\langle n_i | e^{(-2\rho^2/\omega^2)}\sin^2(kz) | n_i \rangle \approx U^{-1/2}\left(n_z + \frac{1}{2}\right) - \frac{1}{2}U^{-1}\left(n_z^2 + n_z + \frac{1}{2}\right) + U^{-1}\frac{\sqrt{2}}{k\omega}\left(n_z + \frac{1}{2}\right)(n_\rho + 1) \ldots
$$

$$
\langle n_i | e^{(-2\rho^2/\omega^2)}\cos^4(kz) | n_i \rangle \approx 1 - 2U^{-1/2}\left(n_z + \frac{1}{2}\right) + \frac{5}{6}U^{-1}\left(n_z^2 + n_z + \frac{1}{2}\right) - U^{-1/2}\frac{\sqrt{2}}{k\omega}\left(n_\rho + \frac{1}{2}\right) \ldots
$$

where $n_\rho = n_x + n_y$. Substituting these equations into Equation 5.20 we find the *net* energy shift from our optical lattice harmonic potential to be:

$$
\begin{aligned}
\Delta E &= \left(n_z + \frac{1}{2}\right)\left(n_\rho + \frac{1}{2}\right)\Delta\tau(\omega) + \left(n_z + \frac{1}{2}\right)\Delta\gamma(\omega_L)U^{1/2} + \\
&\quad \Delta\alpha(\omega_L)U + \left(n_z + n_\rho + \frac{3}{2}\right)\Delta\sigma(\omega_L)U^{3/2} + \Delta\beta(\omega_L)U^2 + \dots
\end{aligned}
\tag{5.25}
$$

where $n = 0, 1, 2, \dots$ is the vibrational quantum state in the harmonic potential, and the terms $\tau(\omega_L)$, $\gamma(\omega_L)$, $\sigma(\omega_L)$, and $\beta(\omega_L)$ are composed of U_0, $a(\omega), a'(\omega)$, and $b(\omega)$. Astonishingly, the quantization of motion yields frequency shifting terms with $U^{1/2}$, and $U^{3/2}$ (and higher-order) dependance. With the above equation, we proceed to minimize the net scalar stark shift and examine the terms $\tau(\omega_L)$, $\gamma(\omega_L)$, $\sigma(\omega_L)$, and $\beta(\omega_L)$ which further reduce in the experimental measurement, hence we forgo their full derivation here (see section 5.5).

5.3   Minimizing the net scalar Stark shift

The lattice light and atom interaction is dominated by the polarizability term in Equation 5.25, $\alpha(\omega_L)$. Crucial to measuring higher order effects is our ability to first minimize the net scalar Stark shift on our clock frequency. As α_{E1} term is $\sim 10^6$ times larger than α_{M1} and α_{E2} in two-electron atoms, it represents by far the largest shift in the polarizability coefficient [64, 122]. Therefore, we must carefully consider the electronic dipole interaction and our methods to zero this effect. We can write the net frequency shift from α_{E1} into scalar, vector, and tenser components in terms of $|F, m_F\rangle$ for a given quantum oscillator by expanding α_{E1} as:

$$
\alpha_{E1}(\omega_L, \mathbf{e}) \cong \Delta\kappa_s(\omega_L) + m_F\xi(\mathbf{k}\cdot\vec{B})\Delta\kappa_v(\omega_L) + \left[3m_F^2 - F(F+1)\right]\left(3\left|\mathbf{e}\cdot\vec{B}\right|^2 - 1\right)\Delta\kappa_t(\omega_L)\dots
$$

where ξ is the lattice polarization ellipticity, $\mathbf{e}$ and $\mathbf{k}$ are the lattice polarization and propagation vectors, respectively, $\vec{B}$ is the spectroscopy bias field, and the differential scalar, vector, and tensor coefficients are $\Delta\kappa_s, \Delta\kappa_v$, and $\Delta\kappa_t$, respectively [131]. Our choice of ytterbium isotope forces the tensor term coefficient to zero because the ^{171}Yb quantum system, where $m_F = \pm 1/2$, possesses

insufficient angular momentum to support a tensor component. Alignment of the bias magnetic field, $\vec{B}$, is perpendicular to lattice propagation, $\mathbf{k}$, implying the coefficient in front of the vector stark term is near zero as well, with any residual shift removed by averaging $m_F = \pm 1/2$ spin state frequencies. We also choose to operate in a 1-D lattice configuration with linear lattice light polarization ($\xi = 0$), further suppressing vector stark effect. With the above techniques, we are free to choose ω_L were the net scalar Stark shift, $\Delta \kappa_s(\omega_L)$, is minimized. Additionally, because frequency is such a precisely measured quantity, reducing α_{E1} to a single, frequency-dependent component facilitates high accuracy measurements of clock shifts relative to lattice intensity.

5.4   Ultra-cold ytterbium ensemble in an optical lattice

The preceding formulation of lattice light shifts only considers a single atom in a particular motional state n. However, as an optical lattice clock contains an ensemble of atoms, forming a diverse array of transverse and longitudinal motional states, we must make an additional effort to quantify our atomic ensemble motional state characteristics before pursuing an absolute lattice light shift measurement. When simultaneously probing an ensemble of atoms, we define an average value of motional state occupation, $\langle n \rangle$, as no single state can be selected. Standard practice is to assume a Boltzmann distribution over bound lattice states, implying $\langle n \rangle$, is given by

$$\langle n \rangle = \frac{\sum_n n e^{\left(-\frac{\epsilon_n}{k_B T}\right)}}{Z} \tag{5.26}$$

where ϵ_n are eigen-energy states of the Hamiltonian, $Z = \sum_n e^{\left(-\frac{\epsilon_n}{k_B T}\right)}$ is the partition function, k_B is Boltzmanns constant, and T is the temperature of the atomic sample [48]. Trap frequencies and eigen-energy spacing are determined by Equations 5.12 and 5.13. Unfortunately this picture is incomplete, as we require an accurate value of atomic ensemble temperature to find $\langle n \rangle$.

Initial intuition supports using an ensemble temperature given by the Doppler cooling limit of our final stage of laser cooling. However, this approach makes the (unlikely) assumption that no alternative cooling is present (e.g. Sisyphus cooling). Furthermore, because optical lattice trap

potential depths can be slightly below final average atomic motional energy, evaporative filtering of atoms from the atomic ensemble can yield Boltzmann distributions inconsistent with the minimum Doppler temperature. Consequently we use only lattice trapped atoms to determine ensemble temperature, utilizing characterization techniques from sideband spectra of single atoms bound in the Lamb-Dicke regime. In such a system, the measure of longitudinal 'temperature' is manifested in the suppression of the red-detuned sideband with respect to the blue detuned sideband [13]. In contrast to the single, well-defined peaks found in single atom spectra, an atomic ensemble will have an integral effect of asymmetrically broadening the oscillator's sideband spectra (see A in Figure 5.3) [16]. The sideband skewing results from longitudinal motion coupling to radial motion, because the potential (Equation 5.9) is not fully separable into longitudinal and radial components, and expansion of $\cos^2$ in Equation 5.10 is not perfectly harmonic. Fortunately, component line shape temperature suppression is still conserved, allowing the measure of atomic ensemble temperature by analyzing total area under the red-detuned and blue-detuned sidebands. Borrowing previous knowledge from the well known single atom spectra, the cumulative sideband line shape can be expressed as a Boltzmann-weighted superposition of motional component line shapes (see [16] for full details). Assuming single dimension excitation, we can write the integrated sideband cross section relation to longitudinal temperature as:

$$\frac{\sigma_{red}^{total}}{\sigma_{blue}^{total}} = 1 - \frac{e^{-E_0/k_B T}}{\sum_{n=0}^{N} e^{-E_n/k_B T}} \tag{5.27}$$

where σ^{total} is that area of the normalized sideband, k_B is Boltzmann's constant, E_0 is the zero-point energy, determined by sharp sideband edge furthest from the carrier, and E_n is the energy of the motional state n. Experimentally we probe the atomic sample along the longitudinal trap direction, recording a frequency scan including both first order blue and red detuned sideband spectra, normalized for atom number. Sideband area is calculated after identifying sideband edge frequency and fitting a curve to the blue and red sidebands separately. We ensure atomic sample depletion is minimal during spectroscopy, preventing a false sideband area ratio. After determining

$f_{long.}$, σ_{red}^{total}, and σ_{blue}^{total}, solving Equation 5.27 numerically yields the corresponding temperature in the longitudinal dimension. Several atomic ensemble spectroscopic line shapes for temperatures ranging from 3-30 μK are displayed in Figure 5.3 A.

Radial sideband excitation is limited by probe light orthogonality and detuning ($f_{radial} \sim 100 - 400$ Hz and $f_{long.} \sim 18 - 200$ kHz), complicating the determination of radial temperature in our experimental setup. Slight probe beam misalignment will excite transverse trap motional states allowing accurate measurement of f_{radial}. Based on Equations 5.12 and 5.13, longitudinal sideband spectrum, and the methods in used reference [16], we can determine the radial temperature from the longitudinal sideband spectra. Notably, the width of the sideband broadening from dimensional coupling (e.g. Figure 5.3 A) is proportional to transverse ensemble temperature.

5.5   Experimental determination of lattice light shifts

Experimental determination of our lattice light shifts has been reported by our group previously [73, 9]. However, realizing a 10^{-18} uncertainty in these shifts requires accounting for additional systematics introduced when varying lattice power in a similar, but more accurate, lattice light measurement. To this end, we implemented several features in a new lattice construction to facilitate our high accuracy measurement. First, as completing a lattice light shift measurement requires interleaving measurments with alternating lattice power, we constructed a build-up cavity around our atoms, substantially amplifying the relativity small light shifting effects. Second, with an enhanced lattice intensity, we expanded the trap mode volume such that single clock cycle collisional shifts where limited at $\sim 5 \times 10^{-18}$, which were then measured with an uncertainty of $\sim 3 \times 10^{-19}$.[1]   Third, to frustrate atomic tunneling between lattice sights, we employ a simple, 1-D vertical lattice, lifting the degeneracy from each motional state via the gravitational potential. In this configuration, atoms trapped in a lattice potential must gain or lose a quanta of Bloch energy

---

[1] See Chapter 6, Section 6.1.4 for more details

when tunneling, greatly suppressing this effect.[2]   Finally, we applied advanced filtering to the lattice light, significantly suppressing background laser amplified spontaneous emission not at the operating lattice frequency.[3]   Our lattice engineering enables trap depths reaching 2000 E_r (lattice recoil energy, $E_r/k_B = 100$ nK), thereby trapping up to several million atoms in a well defined and uniform periodic potential.

Previous lattice light measurements required little knowledge of atomic ensemble temperatures for the desired clock performance. However as previous theoretical work predicted motional state dependent lattice frequency shifts, we began to investigate motional temperature dependance relative to lattice trap potential. Figure 5.3 B shows the corresponding trap temperature with lattice potential depth in E_r. The data reviled a near perfect linear dependence of trap temperature on trap depth, implying components of $\propto$(n+1) in Equation 5.25 gain an $U^{1/2}$ dependance. We find that intensity terms with root dependance ($U^{m/2}$ where m is an integer) collapse to coefficients of linear, quadratic, and higher order powers. The relatively complex lattice clock frequency shift from Equation 5.25 reduces to

$$\Delta\nu = \alpha(\omega_L, T)U + \beta(\omega_L, T)U^2 \qquad (5.28)$$

where the coefficients $\alpha(\omega_L)$, $\beta(\omega_L)$ gain a temperature dependance. Therefore, we must report the lattice atomic temperature at each set-point when recording a light shift measurement. Also, great care must be taken when relating $\alpha(\omega_L)$ to $\alpha(\omega_L, T)$ etc. as these coefficients are not, strictly speaking, well resolved into pure atomic polarizabilities of ytterbium. Additionally, because different motion states $|n\rangle$ sample different magnetic and electric field intensities we must precisely control the atomic temperature loaded into the lattice.

At a unique lattice frequency, we make an absolute frequency measurement referenced to a NIST traceable Hydrogen maser. After confirming the absolute lattice frequency, we take sideband spectra for two clock configurations, the first is the 'reference' clock (based on a given lattice

---

[2] See Chapter 6, Section 6.1.6 for more details
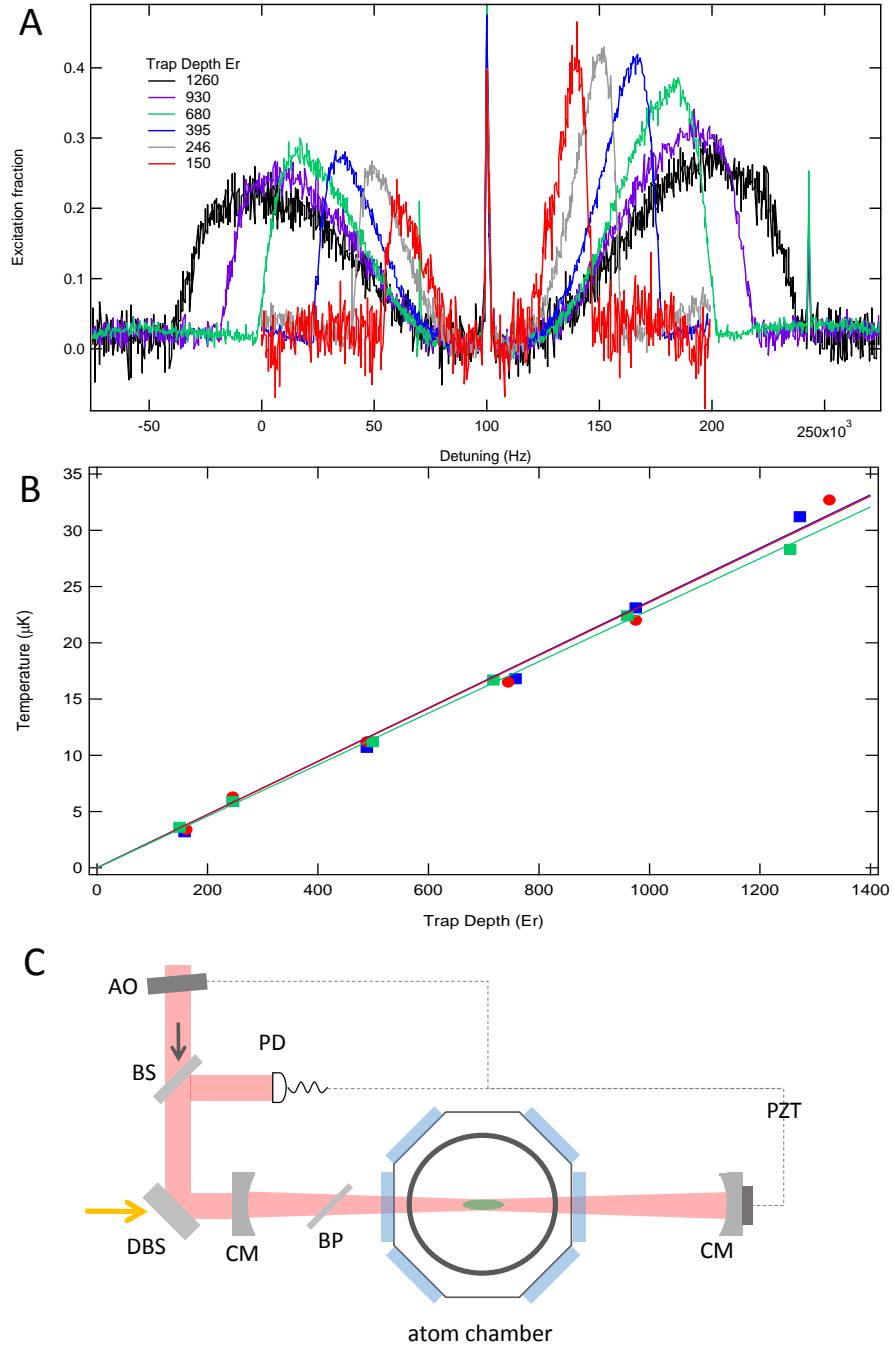[3] See Chapter 2 for more details

Figure 5.1: (A) A broad frequency trace subtending red-detuned and blue-detuned sidebands around the carrier frequency for different trap depths. (B) Calculated atomic ensemble temperature at different trap depths. (C) A graphic depiction of our improved vertical optical lattice build-up cavity utilized in this measurement configuration.

intensity) used throughout all measurements and a second perturbed light shifted case. With the sideband spectra we are able to confirm accurate temperature dependance vs. lattice intensity and absolute temperature values [16]. We record the differential frequency shift between the two clock configurations, to an uncertainty of $\sim 1 \times 10^{-17}$ for a particular change in lattice intensity. Repeating the above procedure for different lattice intensities produces a single curve found in Figure 5.2. With sufficient data, we fit our curve to Equation 5.28, producing linear and quadratic coefficients
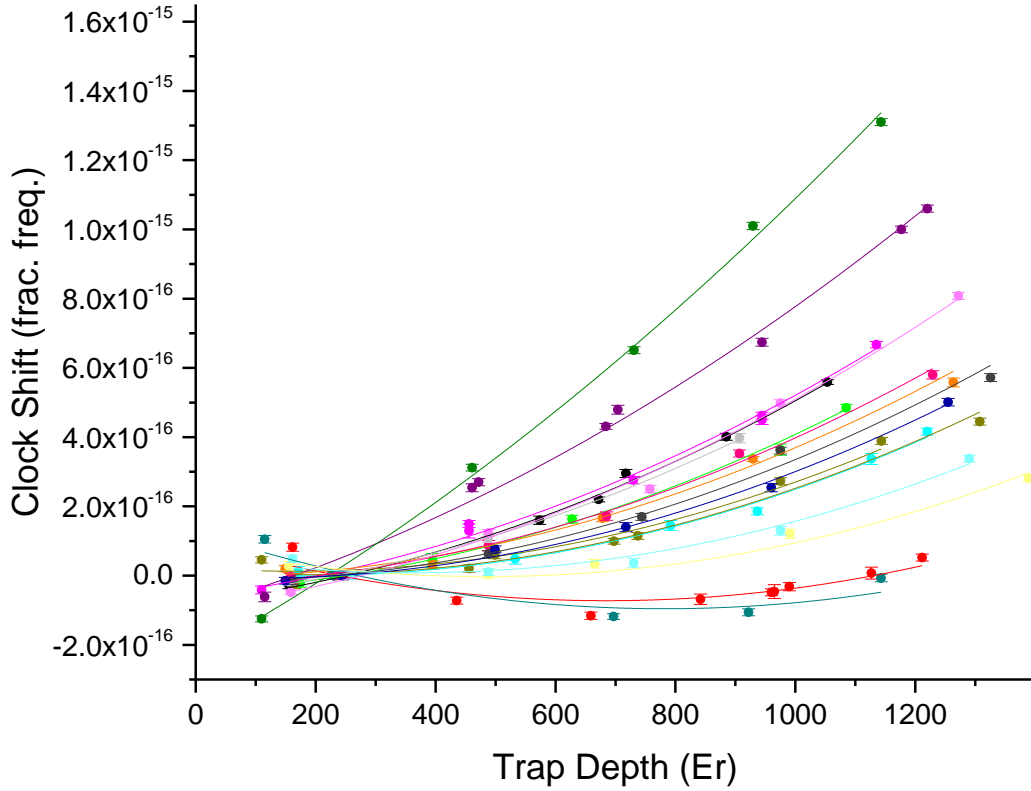

Figure 5.2: Recorded clock shift dependance on optical lattice trap depth for different lattice detuning around 394,798,270 MHz

with one sigma uncertainties given by the reduced χ^2. In our range of curve detuning there is

negligible frequency dependance on $\beta(\omega_L, T)$ for our required accuracy measurement. As such, we use a fitting protocol to globally fit $\beta(\omega_L, T)$ while locally fitting $\alpha(\omega_L, T)$, yielding improved uncertainty results. We estimate our differential temperature uncertainty between measurement points to be $< 10\%$, with an absolute value limited by our understanding of the thermal ensemble. Special attention must be given to the spectral purity of the lattice laser light source. Laser sources have amplified spontaneous emission that forms (usually) time-dependent, background spectrum of off resonant light that can Stark shift the atoms, yielding a false determination of the magic wavelength [118]. The Ti:Sapphire lasers used here exhibit a low amplified spontaneous emission background spectrum (> 60 dB below carrier) and pass through additional Bragg grating filters of various bandwidths (1 nm to 50 pm). Also excessive heating can result from amplitude noise and frequency noise resonant with the motional sideband. Careful control of servo resonances limited these unwanted heating effects.

5.5.1   Lattice polarizability

In 2008 we made a first attempt to find a working wavelength for our optical lattice starting from a theoretical calculation of the lattice magic wavelength, where the ac-Stark shift of the upper and lower clock state match, preserving the natural transition frequency [103, 9]. By tuning the lattice laser frequency around the calculated value, and monitoring the asymmetry of the clock spectroscopic line shape, we reduced the sensitivity of motional state occupation to lattice intensity. After minimizing line-shape asymmetry, we recorded the clock frequency shift relative different lattice intensities for a unique lattice frequency and fit the data to a linear dependance. The slope of each record is proportional to the differential polarizability (at that lattice frequency). Plotting the linear coefficients as a function of lattice frequency reveals a 'zero crossing' or intensity independence in lattice frequency, defined as the magic wavelength.

Here we repeat the above measurement in a similar fashion with several improvements. First, the precision of our clock frequency shift uncertainties are reduced by ~ 100x ($< 3 \times 10^{-17}$ vs.

$< 3 \times 10^{-15}$). Second, we doubled the lattice trap depth (measurement leverage) to $\sim 2000 \, E_r$ from our previous depth of $\sim 1000 \, E_r$. Third, we fix and record the temperature for each measurement set-point. Finally, we independently measure the density shift as a function of trap depth and apply the correction ($\sim 4 \times 10^{-18}$ fractional shift with a 10% uncertainty) to our measured fractional frequency shift. For a unique lattice frequency we vary lattice power as described above and fit our data to Equation 5.28. In Figure 5.3 we plot the resulting linear differential polarizability coefficients per unit of recoil energy, E_r, as a function of lattice detuning (corrected for the density shift). Taking a linear weighted fit of our data we find the zero crossing frequency, to be 394,798,271.3(6) MHz with a $\alpha(\omega_L, T)$ slope (in fractional frequency units) of $-1.84(5) \times 10^{-20} \frac{1}{E_r MHz}$ at 3 μK. For a 100 E_r potential, we find a systematic fractional frequency uncertainty for this system of 1.0×10^{-18}.

5.5.2 Lattice hyperpolarizability

The hyperpolarizability effect, $\propto U^2$, is a result of fourth order electric dipole interactions between the quantum oscillator and lattice light field. By the nature of this effect, the induced clock frequency shift should be quite small unless an atom experiences high lattice intensity or the lattice frequency is close to any two-photon resonances. After experimentally determining the magic wavelength in our original 2008 measurement, we found three two-photon resonances close enough in frequency to warrant a direct measurement of this effect. The nearby, off resonant transitions are: $6s6p^3P_0 \leftrightarrow 6s8p^3P_{j=0,2}$ at 759.7082 nm ($j = 0$), and 754.23 nm ($j = 2$), and $6s6p^3P_0 \leftrightarrow 6s5f^3F_2$ resonances at 764.95 nm. Of particular concern is the $^3P_0 \leftrightarrow ^3P_0$ transition as it is close to the magic wavelength and has an ~ 10 times larger shift than $^3P_0 \leftrightarrow ^3P_2$ and $^3P_0 \leftrightarrow ^3F_2$ resonances.

In our previous hyperpolarizability measurement, the clock frequency shift was recorded near each two photon resonance relative to a frequency comb stabilized to a Ca clock. The shifted Yb clock frequency line was fit to a Lorentzian, and plotted relative to lattice laser detuning. Frequency
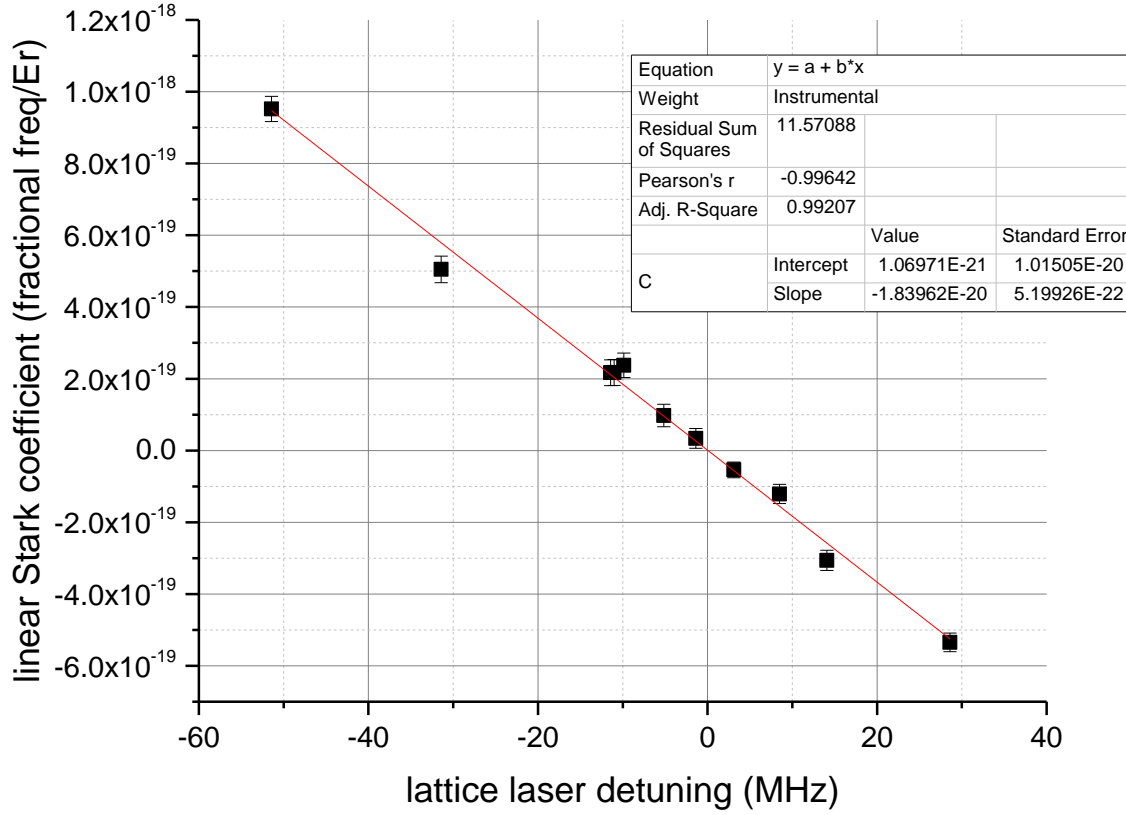
Figure 5.3: Differential polarizability coefficient per unit of lattice recoil energy plotted as a function of lattice detuning around 394,798,271.3 MHz.

shift data was fit to dispersion line shape of the from

$$\Delta\nu = \delta\frac{\Omega_{2\gamma}^2}{4\delta^2 + \Gamma^2} \tag{5.29}$$

where $\Delta\nu$ is the clock shift, δ is the lattice detuning from λ_m, $\Omega_{2\gamma}^2$ is the rabi rate of the two-photon transition, and Γ is the linewidth of the resonance. After a careful line shape fit and lattice intensity calibration, the corresponding clock shift is calculated at the magic wavelength, with a hyperpolarizability shift of $0.80(12)$ $\mu Hz/E_r^2$ [9]. At 100 E_r, this corresponds to a total frequency shift of ~ 8 mHz or fractional shift of 1.5×10^{-17} with an uncertainty of $< 5 \times 10^{-18}$.

In our second hyperpolarizability treatment, we extract $\propto U^2$ dependance from a global free parameter fit of Equation 5.28 an collected polarizability data. The $\beta(\omega_L, T)$ coefficient at 3 μK was found to be $3.6(2) \times 10^{-22} \frac{\Delta\nu}{\nu_0} \frac{1}{E_r^2}$ or $0.19(0.02)$ μHz/E_r^2. We note the large discrepancy between our previously reported hyperpolarizability value and second treatment. The observed $\beta(\omega_L, T)$ coefficient is reduced in magnitude relative to the bare atomic value by the finite ensemble temperature; since atoms in higher motional states experience lower time averaged lattice laser intensity. Further modeling of motional state affect on the hyperpolarizability shift supports our lower 'operational' hyperpolarizability coefficient, but remains in disagreement with theory (within a factor of 1.5) implying more investigation is warranted. However, at the time of this writing we report an 'operational' hyperpolarizability coefficient of $0.19(0.02)$ μHz/E_r^2 at 3 μK. This corresponds to an induced fractional frequency shift of 3.6×10^{-18} with an uncertainty of less than 4×10^{-19}.

5.5.3 Multipolar polarizability

Initial theoretical work proposing the presence of an M1-E2 related shift estimated the effect could lead to fractional frequency shifts as large as 10^{-16}, limiting the clock's ultimate performance [122]. However, a subsequent experimental investigation in a Strontium optical lattice clock indicated a shift consistent with zero at 10^{-17} level [131]. In our experimental study of lattice light shifts the M1-E2 term is absorbed into $\alpha(\omega_L, T)$ and $\beta(\omega_L, T)$ therefore we make a theoretical calculation of this systematic [2]. For ytterbium, we compute the M1 and E2 polarizabilities to be roughly equivalent and $\sim 4.0(0.4) \times 10^{-7}$ less then the E1 polarizability. Starting from Equations 5.16 -5.18 we can write the total M1-E2 potential as

$$U_{M1/E2}(z) \quad = \quad -\left(\frac{E_0}{2}\right)^2 \alpha_{M1}(\omega)\sin^2(kz) - \left(\frac{E_0}{2}\right)^2 \alpha_{E2}(\omega)\sin^2(kz) \tag{5.30}$$

$$U_{M1/E2}(z) \quad \cong \quad -2\left(\frac{E_0}{2}\right)^2 \alpha_{M1}(\omega)\sin^2(kz). \tag{5.31}$$

$$\tag{5.32}$$

We can write the electric field in terms of the potential from Equation 5.16:

$$-\left(\frac{E_0}{2}\right)^2 = \frac{U_{E1}(z)}{\alpha_{E1}(\omega)\cos^2(kz)} \tag{5.33}$$

Implying,

$$U_{M1/E2}(z) = -2\frac{\alpha_{M1}(\omega)}{\alpha_{E1}(\omega)}\left(\frac{sin^2(kz)}{\cos^2(kz)}\right)U_{E1}$$

Rewriting in fractional units we have,

$$\frac{\Delta\nu}{\nu_0} = -2\frac{\alpha_{M1}(\omega)}{\alpha_{E1}(\omega)}\left(\frac{\sin^2(kz)}{\cos^2(kz)}\right)\frac{U_{E1}}{E_r}\frac{E_r}{h\nu_0} \tag{5.34}$$

Where

$$\frac{\alpha_{M1}(\omega)}{\alpha_{E1}(\omega)} \cong 4.0 \times 10^{-7}$$

$$\frac{\sin^2(kz)}{\cos^2(kz)} \cong 0.01 \text{ for a Lamb-Dicke parameter of } \eta = 0.1$$

$$\frac{U_{E1}}{E_r} = 100 \text{ for our operational lattice depth}$$

$$\frac{E_r}{h\nu_0} = 3.88 \times 10^{-12}$$

Armed with the calculations we find fractional frequency shift to be 3.1×10^{-18} with a 10% uncertainty stemming from our calculations of the M1 and E2 polarizabilities.

5.6   A magic wavelength for 10^{-18} timekeeping

The key to lattice clock operation is correctly canceling large scalar light shifts and measuring residual systematics created by the trapping potential. After careful study of our first order and second order coefficients we consider the correct operation frequency of our lattice light. First, we fix the final atomic ensemble temperature to $\sim 3~\mu$K, the minimum temperature limit we can experimentally achieve for ytterbium. Then we limit the lattice intensity utilizing a vertical lattice configuration so that a low 100 E_r operational trap debt can be employed, minimizing the second order coefficient uncertainty while providing enough trapping potential to retain between 5000-100,000 for sufficiently low lattice tunneling, and atomic quantum projection noise

below the optical local oscillator fractional instability. Finally, to minimize sensitivity to lattice intensity uncertainty, we operate $\sim$3.9 MHz blue detuned from the measured magic wavelength (394,798,271.3(6) MHz), where the polarizability and hyperpolarizability balance, leading to insensitivity to first order changes in lattice intensity as shown in Figure 5.4. The above techniques produce a robust operational optical lattice with a total lattice light clock shift of ~ -1.6 mHz or -3×10^{-18} fractionally, with an uncertainty of 1.1×10^{-18}. The uncertainty is increased from Figure 5.4 because although a particular clock (in this case, the second ytterbium system) can be well studied, universal understanding of the lattice light shift is limited by modeling of motional state population at the time of this writing.
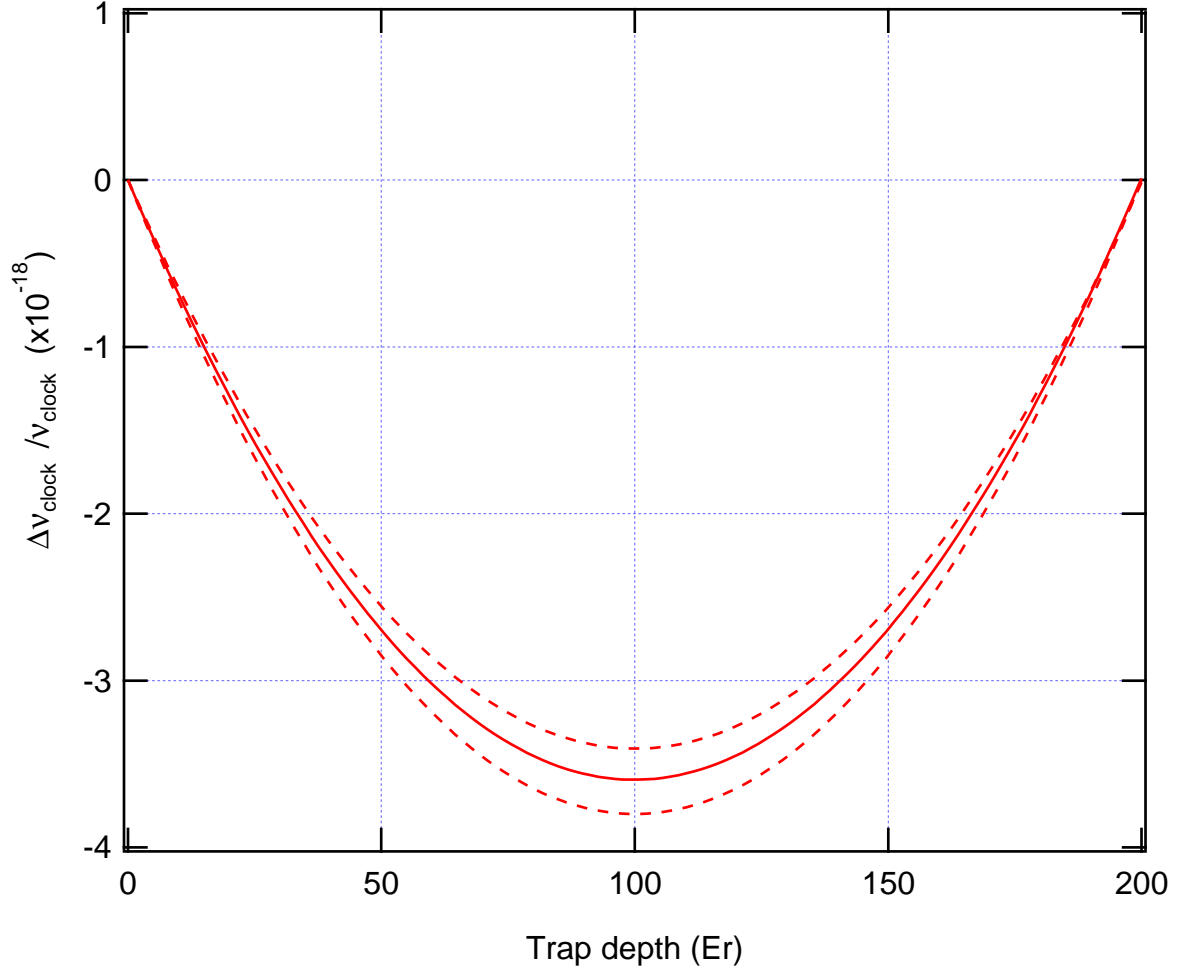
Figure 5.4: Operational magic wavelength tuned to operate around 100 E_r lattice depth. Dashed lines represent one sigma standard error from the hyperpolarizability uncertainty. Plot courtesy of R. Brown.

Chapter 6

Systematic Frequency Shifts in a Ytterbium Optical Lattice Clock

Previous chapters featured effects significant to the fundamental operation of an optical lattice clock for optical based timing performance. Our motivation for these studies was to further our understanding of the physics governing atoms as well as measure and reduce the systematic effects of our atomic clock. Here we reflect on other systematic effects that influence 10^{-18} timekeeping. Then we report our current physical understanding of the $^1S_0 - ^3P_0$ clock transition at 2×10^{-18} fractional frequency uncertainty. Finally we consider future prospects for 10^{-18} timekeeping and beyond.

6.1   Other systematic effects

To reach 10^{-18} level timekeeping performance, we must consider other important, but perhaps less relevant systematics effects. In this section we cover a detailed list of all systematic effects that alter our clock frequency by performing a series of optical frequency comparisons between normal clock operation and a highly perturbed (leveraged for measurement) clock configurations that quantify our desired systematic.

6.1.1 First-order Zeeman effect: with lattice Stark shift

Starting from M. M. Boyd *et al.* [22], we can write the total frequency shift on the ground and excited state as

$$\Delta_e \;=\; -m_F(g_I+\delta g)\mu_0 B - \kappa_e^S\frac{U_T}{E_r} - \kappa_e^V\xi m_F\frac{U_T}{E_r} \tag{6.1}$$

$$\Delta_g \;=\; -m_F g_I\mu_0 B - \kappa_g^S\frac{U_T}{E_r} - \kappa_g^V\xi m_F\frac{U_T}{E_r}. \tag{6.2}$$

where $g_I = \mu_I(1-\sigma_d)/(\mu_0 I)$ is the nuclear g factor, $\mu_I(1-\sigma_d) = 0.491\,889(8)\times\mu_N$ is given by L. Olschewski [92], δg is the differential g factor, κ_e and κ_g are shift coefficients for scalar and vector polarizabilities (note that tensor polarizability is identically zero for $m_F = \pm 1/2$), and subscripts e and g refer to the excited and ground states, respectively. E_r is the energy of a lattice photon recoil and U_T/E_r characterizes the lattice intensity.

If we assume that the $^1S_0$ state vector shift is sufficiently small, and we operate at the magic wavelength, $\lambda \sim 394,798,220$ MHz, we can write the differential frequency shift, $\Delta\nu$, using Equations 6.1 and 6.2 as;

$$\Delta\nu \;=\; \Delta_e - \Delta_g = -m_{F_e}(g_I+\delta g)\mu_0 B - \kappa_e^V\xi m_{F_e}\frac{U_T}{E_r} + m_{F_g}g_I\mu_0 B. \tag{6.3}$$

We can write frequency differences corresponding to π and σ transitions from line center as;

$$\nu_{\sigma^+} - \nu_c \;=\; -\frac{1}{2}(\delta g + 2g_I)\mu_0 B - \frac{1}{2}\delta\kappa U_0. \tag{6.4}$$

$$\nu_\pi^L - \nu_c \;=\; -\frac{1}{2}\delta g\mu_0 B - \frac{1}{2}\delta\kappa U_0, \tag{6.5}$$

$$\nu_\pi^H - \nu_c \;=\; \frac{1}{2}\delta g\mu_0 B + \frac{1}{2}\delta\kappa U_0, \tag{6.6}$$

$$\nu_{\sigma^-} - \nu_c \;=\; \frac{1}{2}(\delta g + 2g_I)\mu_0 B + \frac{1}{2}\delta\kappa U_0 \tag{6.7}$$

where $\delta\kappa = \kappa_e^V\xi$. From the above equations, we have

$$\Delta\pi \;=\; \nu_\pi^H - \nu_\pi^L = \delta g\mu_0 B + \delta\kappa U_0, \tag{6.8}$$

$$\Delta\sigma \;=\; \nu_{\sigma^-} - \nu_{\sigma^+} = (\delta g + 2g_I)\mu_0 B + \delta\kappa U_0. \tag{6.9}$$

Combining Equations 6.8 and 6.9, we have

$$B = \frac{\Delta\sigma - \Delta\pi}{2g_I\mu_0}.$$ (6.10)

Solving Equation 6.8 for $\delta g\mu_0$ we get

$$\delta g\mu_0 = \frac{1}{B}\left(\Delta\pi - \delta\kappa U_0\right).$$ (6.11)

To determine B and δg, we need to know a priori $\delta\kappa$. First, we minimize $\delta\kappa$ by running the clock in a low bias field case and rotating a $\lambda/2$ and $\lambda/4$ waveplates, minimizing π splitting. Then to quantify $\delta\kappa$, we operate our clock in an interleaved two-clock mode, alternating between two different lattice potentials $U_0 = U_T^L/E_R \propto 567$ mW and $U_1 = U_T^H/E_R \propto 908$ mW, respectively. For this unique lattice configuration, we calculate the slope $\delta\kappa$ by recording differential π transition spacing between U_0 and U_1 lattice potentials, measuring $\delta\kappa = 0.28(3)$ mHz/mW.

With this formulation we measure the first order Zeeman coefficient, $\delta g\mu_0$, by recording the frequency spacing between each hyperfine component in an artificially stretched clock configuration. Due to a small drifting B field (several mG/hour), it was necessary to calculate $\delta g\mu_0$ 'line-by-line' as frequency information was recorded from the π and σ transitions. This data exhibited a statistically significant dependence on the magnetic field, due to the vector Stark shift. As such, calculating $\delta g\mu_0$ at higher magnetic fields proved more advantageous because the fractional contribution of $\delta\kappa$ in Equation 6.11 is highly suppressed. Figure 6.1 displays the calculated (average) value of $\delta g\mu_0$ for different magnetic bias fields. Error bars, representing one sigma uncertainty on each first order coefficient, are taken from a total Allan deviation of computed line-by-line $\delta g\mu_0$ data. We find a weighted averaged of $\delta g\mu_0$ to be 399.031(4) Hz/G.

For normal clock operation we configure a 1 G bias field and alternately interrogate both $m_F = \pm 1/2$ Zeeman states, dramatically suppressing the first order Zeeman effect [73]. However, any magnetic field drift between $m_F = \pm 1/2$ clock interrogations can result in a residual first order Zeeman shift. Therefore we interrogate the π transitions in an interleaved forward and reverse
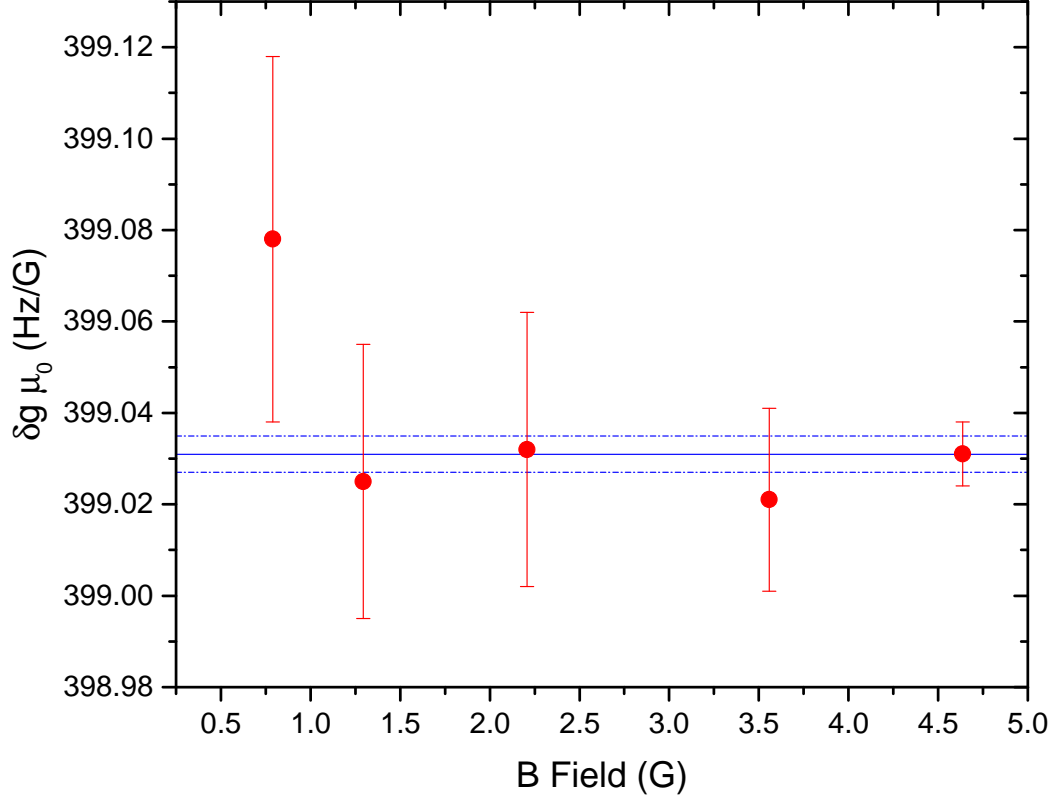
Figure 6.1: First order Zeeman coefficient, $\delta g \mu_0$, measured at different bias magnetic fields. We report a $\delta g \mu_0$ weighted average (solid line) of 399.031(4) Hz/G. Dotted line represents one sigma error.

frequency detuning, removing first order drift sensitivity. After implementing a drift insensitive frequency interrogation, we Allan deviate the in-loop error signal from the Zeeman component in the atomic system lock. We find an offset consistent with zero with a one sigma uncertainty of 3×10^{-7} Hz, limiting the residual first order Zeeman shift uncertainty to $< 6 \times 10^{-22}$. Concurrent work demonstrated frequency agreement between a $+B$ direction clock and a $-B$ direction clock that was consistent with zero with an uncertainty of 3.9×10^{-19}, shown in Figure 6.2.

6.1.2   Second-order Zeeman effect: with lattice Stark shift

After measuring $\delta g \mu_0$ and $\delta \kappa$, we can measure the second-order Zeeman shift coefficient α by running our lattice clock at two different magnetic fields, B_0 and B_1 at constant lattice potential U_0. Writing optical frequency differences from line center, ν_c, corresponding to π transitions for clock 0 at B_0 and for clock 1 at B_1 gives;

$$\nu_{(0,1)}{}_\pi^L - \nu_c = -\frac{1}{2}\delta g \mu_0 B_{(0,1)} - \frac{1}{2}\delta \kappa U_0 + \alpha B_{(0,1)}^2, \tag{6.12}$$

$$\nu_{(0,1)}{}_\pi^H - \nu_c = +\frac{1}{2}\delta g \mu_0 B_{(0,1)} + \frac{1}{2}\delta \kappa U_0 + \alpha B_{(0,1)}^2. \tag{6.13}$$

Because the second order Zeeman shift $\propto B^2$, it cannot be averaged away like the first order component. Writing the above equations to show the averaged frequency offset from ν_c from a bias field $B_{(0,1)}$, we have

$$\text{Avg}_\pi^0 = \frac{1}{2}(\nu_{0\pi}^H + \nu_{0\pi}^L - 2\nu_c) = \alpha B_0^2, \tag{6.14}$$

$$\text{Avg}_\pi^1 = \frac{1}{2}(\nu_{1\pi}^H + \nu_{1\pi}^L - 2\nu_c) = \alpha B_1^2. \tag{6.15}$$

Solving for the second order Zeeman coefficient, α, we find

$$\alpha = \frac{\text{Avg}_\pi^0 - \text{Avg}_\pi^1}{B_0^2 - B_1^2} \tag{6.16}$$

where B is measured using Equation 6.11. This formulation can be used to do a line-by-line calculation of the second order coefficient. However, as our measurement leverage is increased from large, hard to control magnetic bias fields, our clock stability can degrade, limiting our measurement of α.

Alternatively we can obtain the second order coefficient from recording the clock shift between bias fields, fitting data to the function $\Delta\nu = b(B_1 - B_0) + c(B_1^2 - B_0^2)$. To extend our measurement leverage we build a bidirectional bias field controller, interleaving clock measurements at high +B and -B bias fields ($\Delta B \sim 18$ G). To verify cancellation of the first order Zeeman shift, as well as the concatenation of +B and -B field measurements in the second order Zeeman shift data, we

needed to demonstrate frequency agreement between a $+B$ direction clock and a $-B$ direction clock. Shown in Figure 6.2 is a $+B,-B$ clock difference consistent with zero with a one sigma uncertainty of 3.9×10^{-19}. After demonstrating $+B$ and $-B$ bias field agreement, we recorded
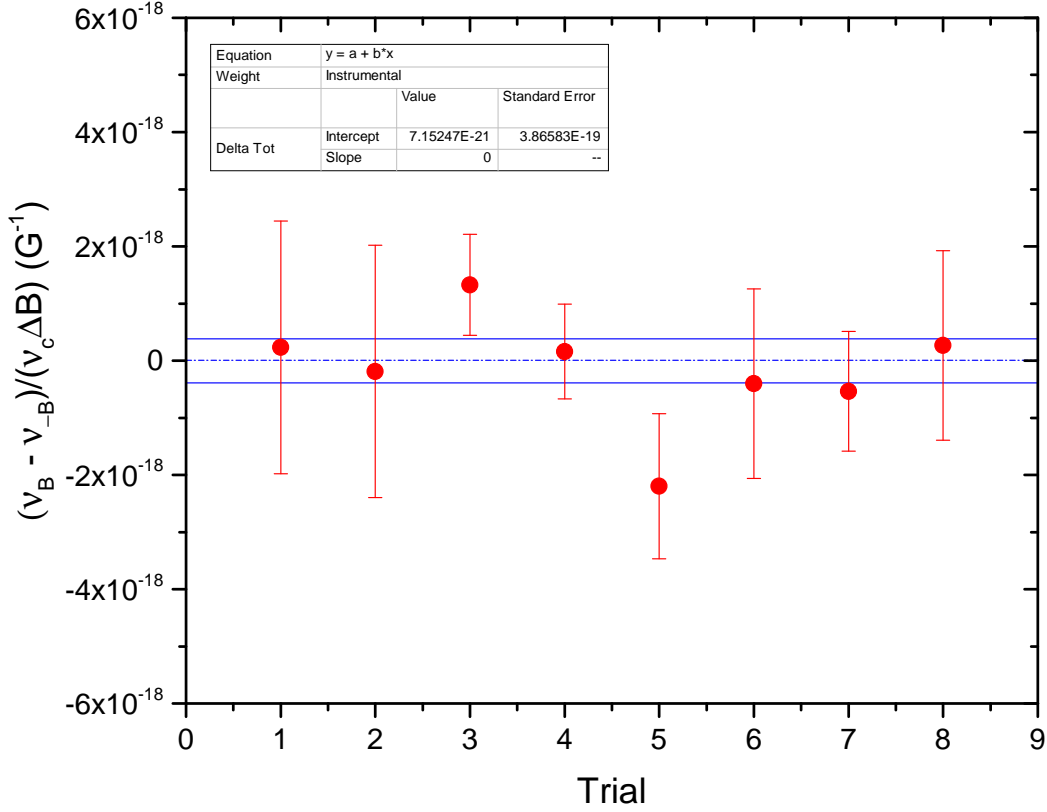
Figure 6.2: Frequency agreement between a $+B$ direction clock and a $-B$ direction clock. The weighted average frequency difference (dotted line) was found to be consistent with zero with an uncertainty of 3.9×10^{-19}. Solid lines represent one sigma error.

the the frequency difference for interleaved high +B and -B bias fields. Using a nonlinear 2-D surface fitting method yielded a second order coefficient of -0.06095(7) Hz/G^2. Additionally we found the line by line calculation of α to give -0.06100(13) Hz/G^2, in good agreement with our measured quantity. A summery of our results are shown in Figure 6.3 and 6.4. Shown in Figure
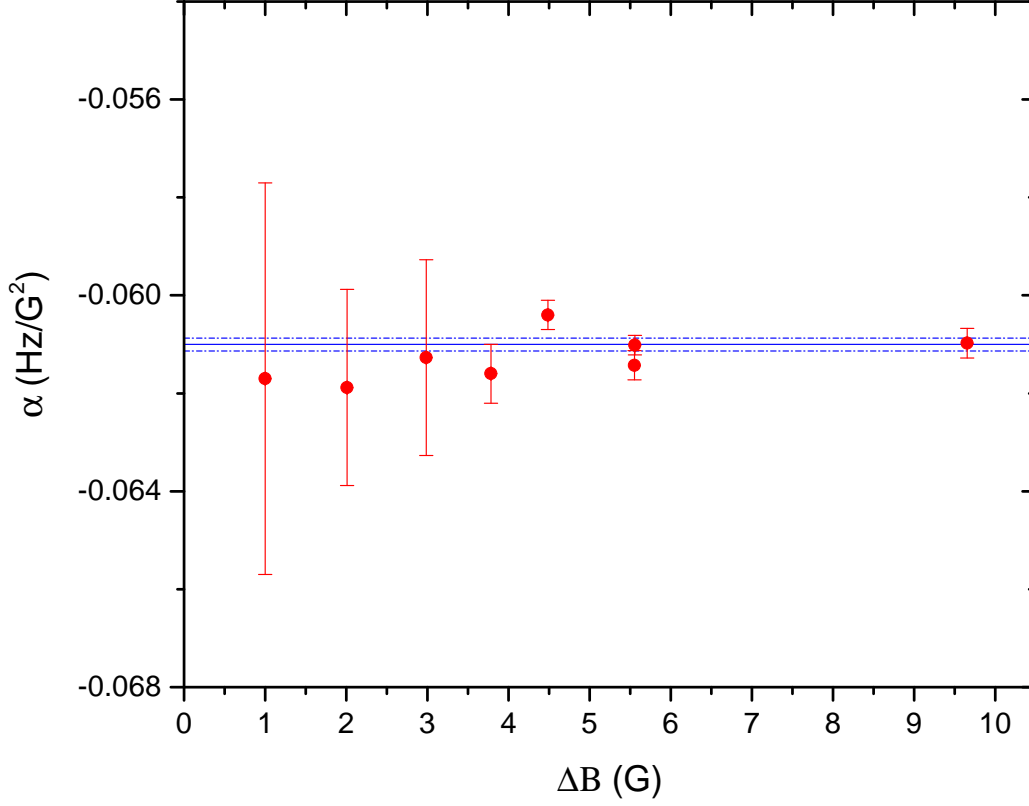
Figure 6.3: Line by line calculation of second order Zeeman coefficient, α, vs. bias field ΔB (B_0 was 1.25 G.). The weighted average value of α, (solid line) is -0.06100(13) Hz/G^2. Dotted lines represent one sigma error.

6.5 is an Allan deviation of the computed second order Zeeman shift from a typical data set. We report an estimated fractional uncertainty of 4×10^{-19}. Additionally, because the combined noise characteristics of our applied and stray B fields are not white, we note the second order Zeeman shift could be a limiting effect when averaging through the 10^{-19} decade for our standard 1 G field. Further efforts to improved instability would greatly benefit from a lower bias field as this shift is $\propto$ Hz/G^2.
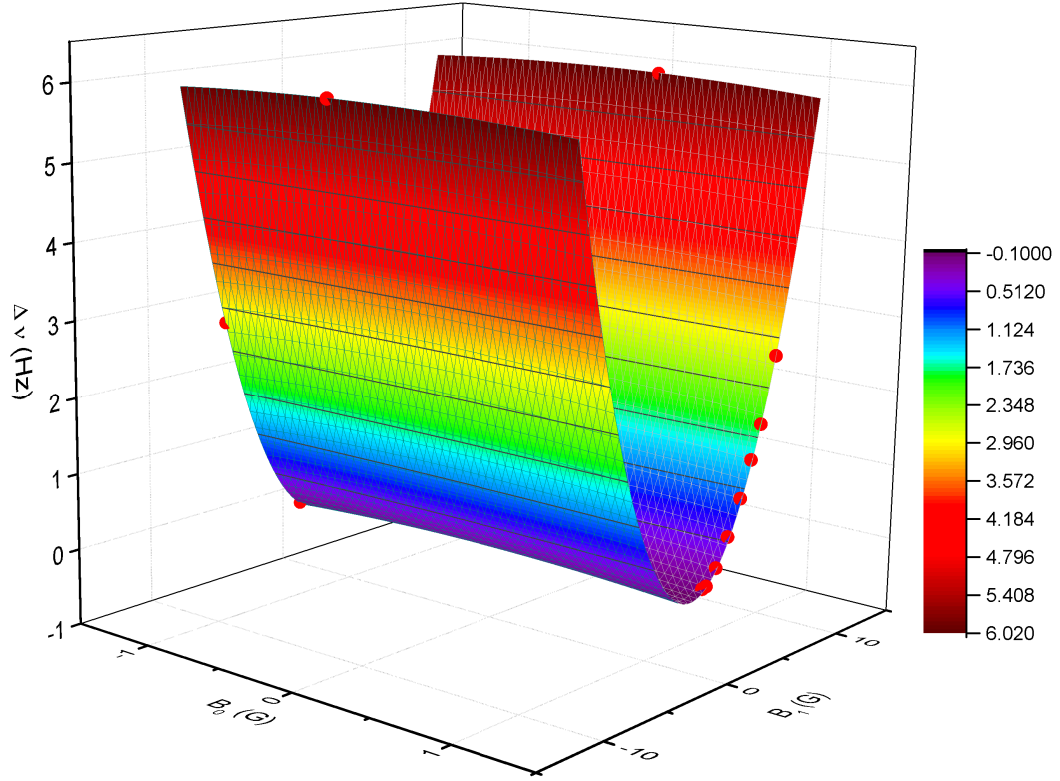
$$\Delta\nu = b(B_1 - B_0) + c(B_1{}^2 - B_0{}^2)$$

Figure 6.4: 2-D surface fit of fractional clock frequency shift, $\Delta\nu$ vs. bias field B_0, B_1 to the function $\Delta\nu = b(B_1 - B_0) + c(B_1^2 - B_0^2)$. The coefficients b, c were found to be -0.0011(7) Hz/G and -0.06095(7) Hz/G^2, respectively.
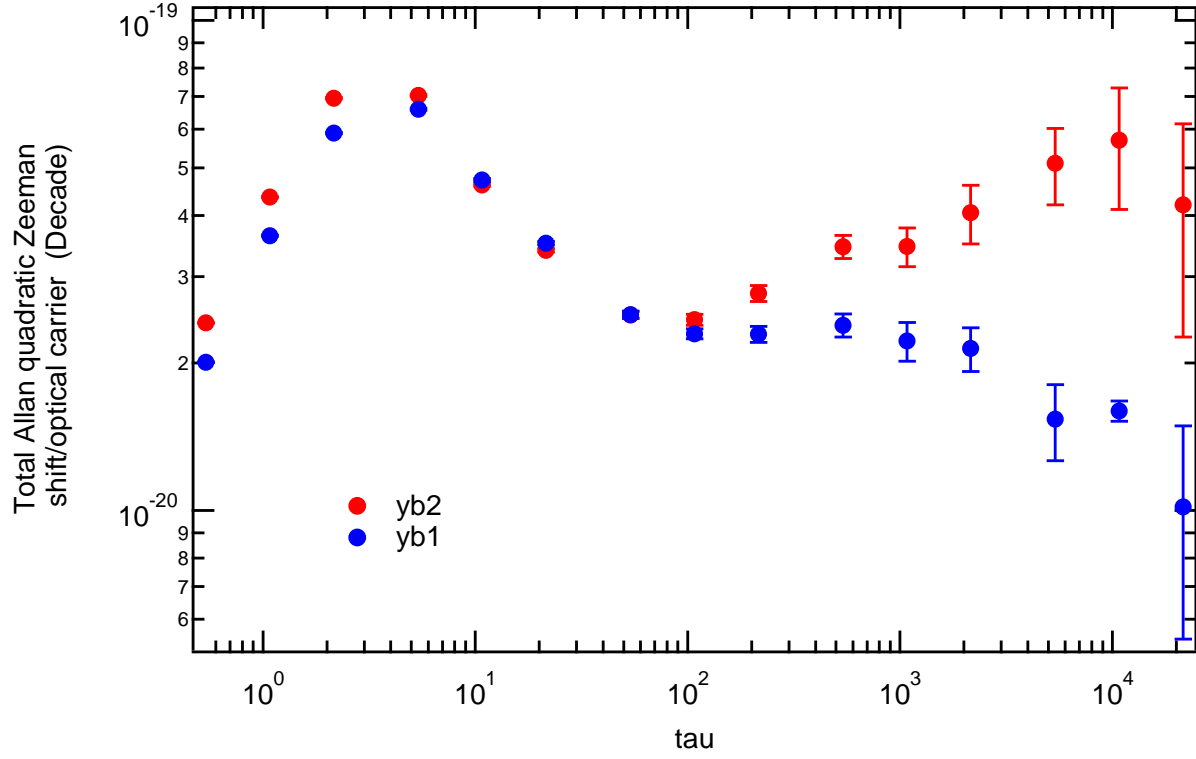
Figure 6.5: A real time measure of the second order Zeeman shift for typical data collection. The peak at ~2 s results from our atomic servo.

6.1.3   DC Stark shift in a radiation shield

Any stray charge accumulating on the inner surface of the vacuum system creates an electric field that could Stark shift our clock frequency [80]. Fortunately our blackbody radiation enclosure also provides our atoms with a Faraday cage, shielding stray electric fields at the lattice potential. To demonstrate this enclosure feature, we apply voltages to opposing windows of our blackbody radiation shield to produce a well defined perturbed electric field along each orthogonal axis. Assuming a stray electric field E_s is independent of all applied fields, we find the clock shift can be expressed as

$$
\begin{aligned}
\Delta \nu &= -\frac{1}{2h}\alpha_{clock}\left|\mathbf{E_s} + \mathbf{E_a}\right|^2 \\
&= -\frac{1}{2h}\alpha_{clock}\left(E_s^2 + E_a^2 + 2E_s^{(i)}E_a^{(i)}\right)
\end{aligned}
$$

where $E_s \equiv |\mathbf{E_s}|$, and $E_s^{(i)} \equiv \mathbf{E_s} \cdot \hat{\mathbf{e}}$. We implement the three following experiment conditions: An applied electric field $E_a^{(i)} = +E_0$, with resulting clock frequency $\nu_+^{(i)}$, an applied electric field $E_a^{(i)} = -E_0$, with resulting clock frequency $\nu_-^{(i)}$, and a ground plate voltage with with resulting clock frequency $\nu_G^{(i)}$. With the above equation we can write the interleaved clock frequency difference as

$$
\begin{aligned}
\Delta\nu_{+-}^{(i)} &\equiv \nu_+^{(i)} - \nu_-^{(i)} = -\frac{1}{2h}\alpha_{clock}\left(4E_s^{(i)}E_0\right) \\
\Delta\nu_{+G}^{(i)} &\equiv \nu_+^{(i)} - \nu_G^{(i)} = -\frac{1}{2h}\alpha_{clock}\left(E_0^2 + 2E_s^{(i)}E_0\right) \\
\Delta\nu_{-G}^{(i)} &\equiv \nu_-^{(i)} - \nu_G^{(i)} = -\frac{1}{2h}\alpha_{clock}\left(E_0^2 - 2E_s^{(i)}E_0\right)
\end{aligned}
$$

Solving for the stray field in the direction $\hat{\mathbf{e}}_{\mathbf{i}}$, independent of E_0 by taking an algebraic combination of the above equations gives,

$$
\begin{aligned}
\delta\nu_s^{(i)} \equiv -\frac{1}{2h}\alpha_{clock}\left(E_s^{(i)}\right)^2 &= \frac{1}{16}\frac{(\Delta\nu_{+-}^{(i)})^2}{\Delta\nu_{+G}^{(i)} - \frac{1}{2}\Delta\nu_{+-}^{(i)}} \\
&= \frac{1}{16}\frac{(\Delta\nu_{+-}^{(i)})^2}{\Delta\nu_{-G}^{(i)} + \frac{1}{2}\Delta\nu_{+-}^{(i)}} \\
&= \frac{1}{8}\frac{(\Delta\nu_{+-}^{(i)})^2}{\Delta\nu_{+G}^{(i)} + \Delta\nu_{-G}^{(i)}}
\end{aligned}
$$

$$= \quad \frac{1}{8} \frac{(\Delta\nu_{+G}^{(i)} - \Delta\nu_{-G}^{(i)})^2}{\Delta\nu_{+G}^{(i)} + \Delta\nu_{-G}^{(i)}} \quad (6.17)$$

A small angle misalignment between windows in the blackbody shield is employed to frustrate etalon formation. Unfortunately, this plate tilt could lead to a non-orthogonal application of E_a. Using ANSYS modeling of the applied electric field we find that window tilt could be as large as 10% fractionally before measurement degradation, well within our shield design. We constructed a high voltage supply to deliver ± 1500-0 V in the three experimental conditions to orthogonal directions [56]. In the vertical direction, $\hat{\mathbf{e}}_\mathbf{z}$, shown in Figure 6.6, the stray charge shift was consistent with zero with a one sigma confidence of $< 1 \times 10^{-20}$. The horizontal directions, larger window spacing and increased grounded shield exposure limited E_a. We found the stray charge to be consistent with zero with a one sigma confidence $< 3 \times 10^{-19}$ and $< 5 \times 10^{-19}$ in the $\hat{\mathbf{e}}_\mathbf{x}$ and $\hat{\mathbf{e}}_\mathbf{y}$ directions respectively. The total stray charge at the atoms was consistent with zero with a one sigma uncertainty of $< 5.8 \times 10^{-19}$.

6.1.4   Cold collision shift

Optical lattice clocks possess the ability to simultaneously interrogate many quantum absorbers with an ultra-narrow-band electronic transition. While this characteristic is essential for exquisite clock performance, tight spatial confinement of quantum oscillators leads to atom-atom interactions in multiple atom occupancy of trap potentials, giving rise to a systematic known as the cold collision shift [83, 73]. Importantly, because the cold collision shift becomes more pronounced with growing atomic population we start to trade systematic uncertainty for improved clock signal to noise. Therefore, suppression and characterization of this shift is critical to realizing optimized clock performance.

In our previous work, we explored methods to minimize, control, and quantify the cold collision shift in our optical lattice clock [74]. In theory, by using an ultra-cold, spin polarized, fermionic isotope of ytterbium we benefit twofold: First, because of odd fermionic exchange symmetry, truly identical fermions cannot collide via even-partial-wave collisions, and second, for the lowest odd-
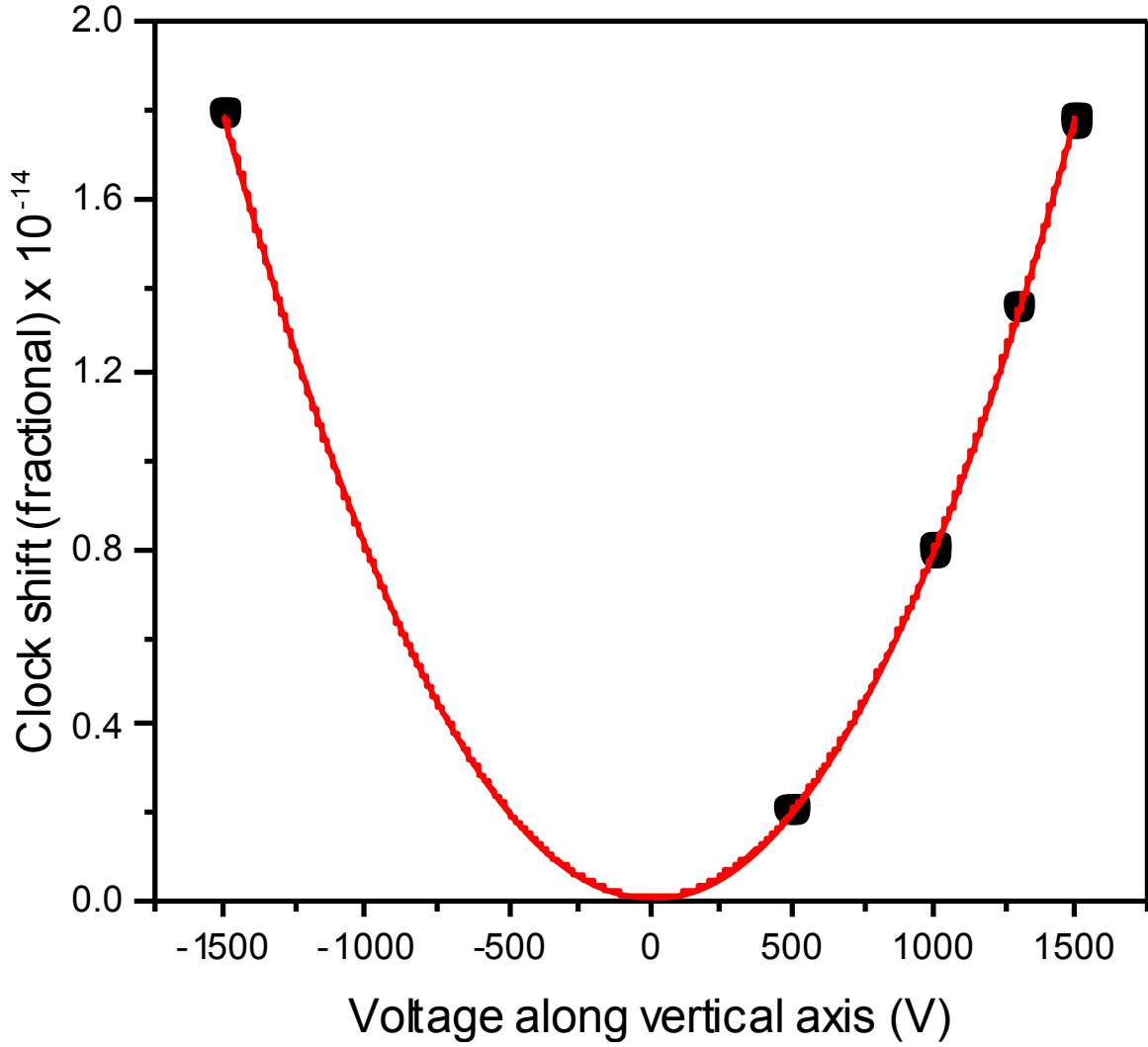
Figure 6.6: Recorded Stark shifts to the clock frequency as a function of applied voltage to the vertically oriented blackbody shield windows. The one sigma standard error for each recorded Stark shift in the vertical direction was $\sim 3 \times 10^{-17}$

partial-wave collisions there exists a centrifugal barrier between atoms but ultra-cold atomic ensemble temperatures possess insufficient energy to overcome this barrier [121, 27]. We found clear evidence of p-wave interactions leading to a cold collision shift in our atomic system, indicating that the collisional energy of the atoms ($\sim$10 μK) facilitates meaningful tunneling through the p-wave barrier. Fortunately, higher partial wave collisions where frozen out and Fermi suppression was significant provided ground state atoms where truly indistinguishable particles (i.e. uniform lattice potential). We proposed cancellation of the cold collision shift using Ramsey spectroscopy with $\sim$50% population excitation, where excited and ground states experience identical collisional shifts, leaving a net zero shift for the atomic ensemble [74].

To construct a clock for 10^{-18} level timekeeping we borrow from our knowledge of cold collisions and take a direct approach to reduced this shift by dramatically expanding our trapping potential volume. We measure the frequency shift from two interleaved clock configurations; one operational with high atom number, and one operational with low atom number. The two independent atomic systems are identical in operation with differing 399 nm slowing beam optical power. In this way, all systematic are common mode with the resulting clock frequency difference resulting from the different densities. Shown in Figure 6.7 is the density shift per atom number for different trap potentials. We use a linear relationship approximation between the cold collisional shift and trap potential over high trapping depths. With lower trapping potentials we find suppression of the collisional shift as our atomic ensemble temperature suppressed tunneling through the p- wave barrier. Our uncertainty in this characterization is largely limited by atom number fluctuations. For 100 E_r and 10000 atoms we find density shift correction to be 4×10^{-18} with an corresponding uncertainty of 3×10^{-19}.

6.1.5   Probe light shift

Interrogation of the clock transition can generally be modeled using a quantum two level system. However, a complete representation includes off-resonant coupling of $^1S_0$ and $^3P_0$ to other

Scaling of Shift with Trap Depth
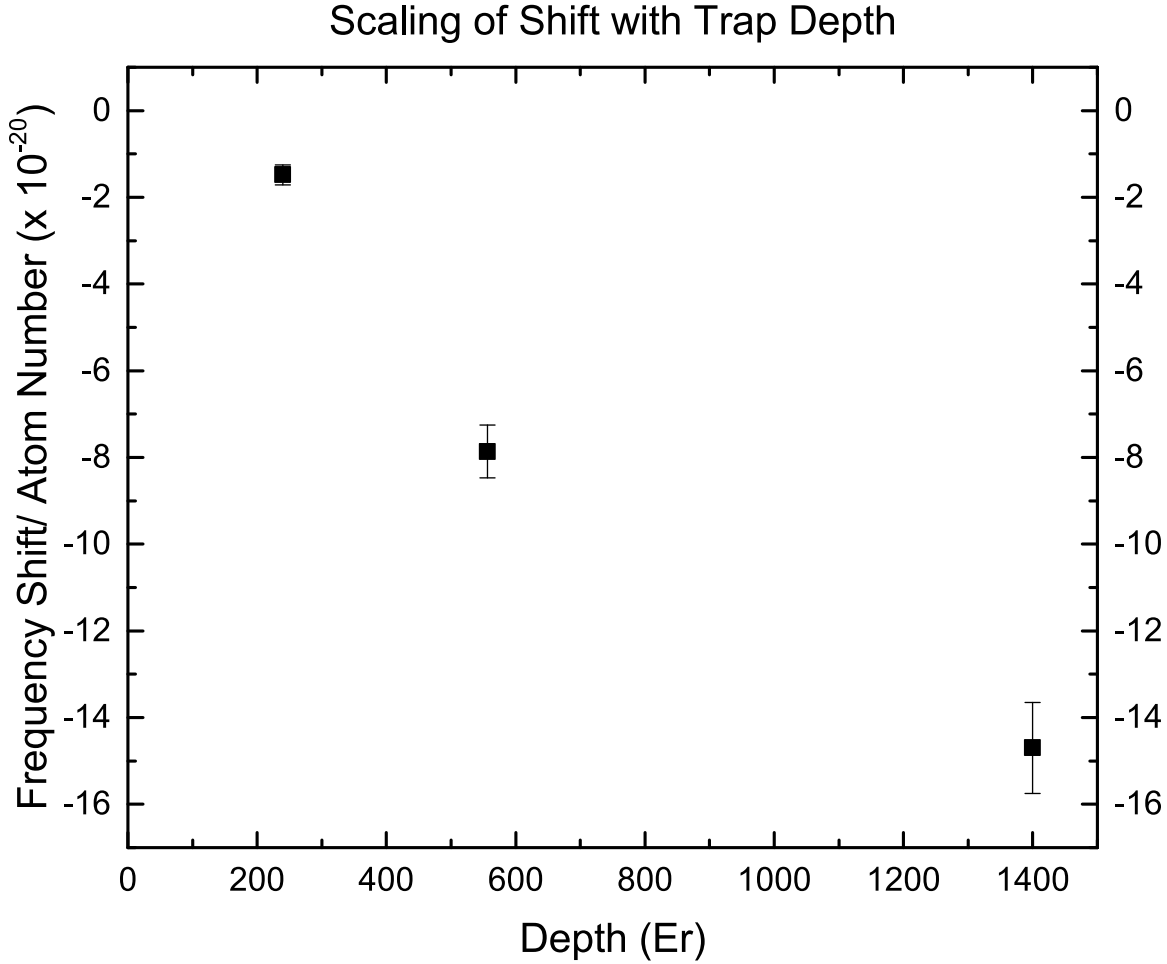
Figure 6.7: The measured collisional shift per unit atom as a function of trap potential in lattice recoil energy. Thermal suppression of p- wave collisions is evident for $E_r < 300$, as atomic ensemble temperatures required for these trap potentials prevent tunneling through the p- wave barrier (30-45 μK).

states, leading to an ac-Stark shift from 578 nm clock light during clock spectroscopy [99]. Direct calculation of the ac-Stark shift from the dynamic polarizabilities of $^1S_0$ and $^3P_0$ at 578 nm gives a shift coefficient of $\sim$17 mHz/(mW/cm^2) [98]. For our experimental setup, we operated with a Gaussian $1/e^2$ intensity clock laser to lattice laser waist ratio of 5 to 1 ensuring a uniform electromagnetic wavefront intensity for clock spectroscopy. A 140 ms Rabi clock spectroscopy time requires $\sim$0.100 mW/cm^2 of 578 nm light intensity, governed by our operating waist ratio,

producing a probe light shift of only a few mHz. Typical Rabi interrogation times last 280 ms - 560 ms, easily placing this effect in the 10^{-19} range.

To directly measure our probe light shift we illuminate our lattice trapped atoms with off resonant 578 nm light while performing clock spectroscopy and record the resulting shift in our clock frequency. Before entering the vacuum enclosure, we send clock light through an electro-optic modulator (EOM) producing first order sidebands at a fixed drive frequency, ω, (from 500 kHz to 10 MHz) with with a fixed amplitude $\sim 20 - 40$ dB below the (carrier) clock light frequency. Then we perform an interleaved clock measurement: the first clock is carrier resonant with the ytterbium clock transition, and the second clock is sideband resonant with the ytterbium clock transition. We modulate the RF power and frequency to the acousto-optic modulator controlling the 578 nm light frequency such that clock light interrogating the atoms is π-pulse resonant with the $^1S_0$-$^3P_0$ clock transition for the respective clock configuration. In this way carrier excitation represents our normal clock operation and sideband excitation represents a highly leveraged probe light shift. Shown in Figure 6.8 is the frequency shift at different off-resonant intensities for our horizontal lattice configuration, (lattice waist of 60 μm). We find a linear shift dependance with a slope of $-4.7(1) \times 10^{-17}/\mu$W. The frequency difference between our two interleaved clocks was a result of servo noise on the clock laser. We operated at 500 kHz and 10 Mz where this effect was minimized. Other detuning with larger frequency offsets produced consistent linear shift dependence. Even operating at a short 140 ms Rabi time, we experience a fractional probe light shift of $< 9.4 \times 10^{-19}$, with a one sigma uncertianty of 2×10^{-20}.

6.1.6   Tunneling in lattice

Tunneling is a consequence of quantum systems constrained in finite periodic potentials. For atoms contained in a optical lattice, this phenomenon can result in coherent atomic motion along the lattice potential, producing Doppler or recoil related effects. Although tunneling is unavoidable, of particular concern are tunneling rates similar to clock spectroscopy times. By
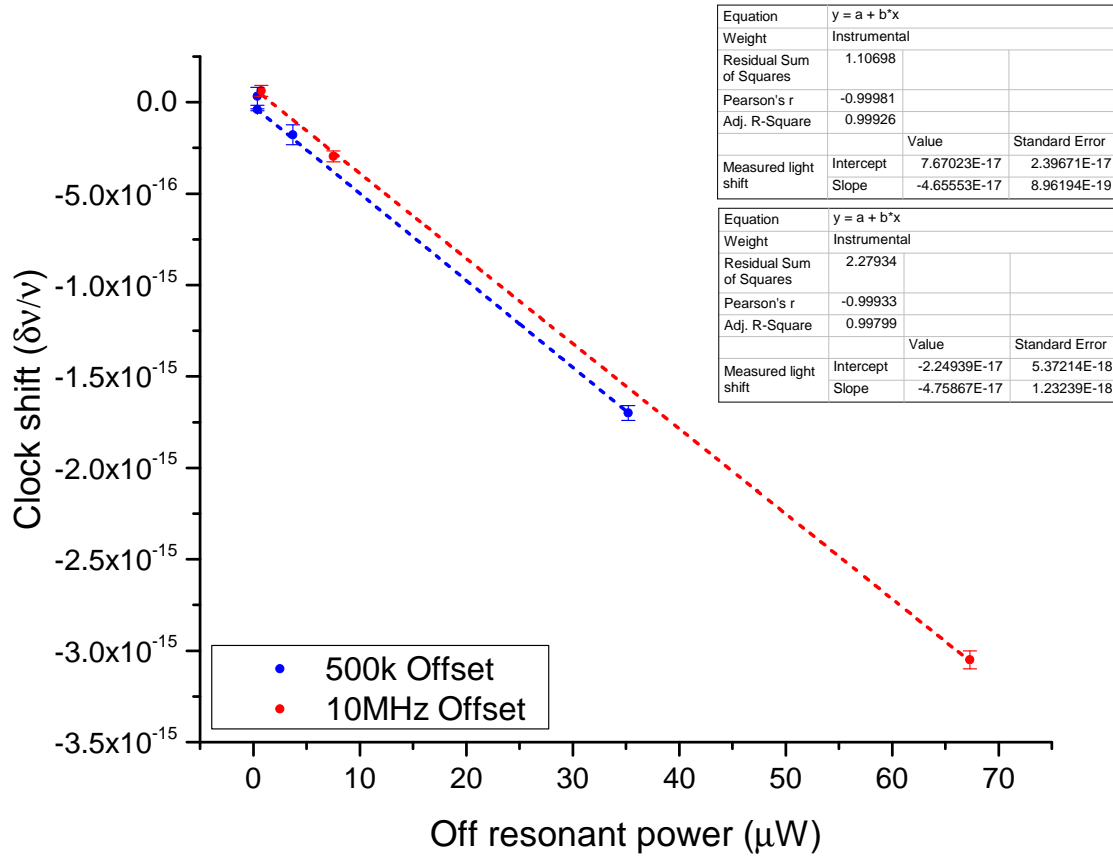
Figure 6.8: Measured Probe light shift on the ^{171}Yb clock frequency for off-resonant frequencies of 500 kHz and 10 MHz detunings at various probe light intensities.

means of the Heisenberg uncertainty principle, we anticipate the tunneling time between adjacent lattice sites to be inversely proportional to energy bandwidth ($\Delta t \propto \frac{\hbar}{2\Delta E}$). For example, assuming a lattice motional bandwidth of ~ 1 Hz (motional bandwidth $\propto$ tunneling energy, J) we estimate a transmission time between potential wells of ~ 0.1 s, potentially delocalizing an atom as much as fifteen lattice wells during our longest spectroscopy times.

In an attempt to limit this effect, we exploit two techniques: gravity induced energy offset between adjacent lattice sites in a vertical lattice configuration, and sideband spectroscopy cooling

technique to force atoms to the ground motional state in the direction of tight lattice confinement (motional bandwidth is a minimum) [76]. This potential energy offset results in a suppression of tunneling rates between lattice sites [76]. Specifically, with the gravitational potential energy offset ($\Delta = mg\lambda/2h \cong 1.6$ kHz for ytterbium, where m is atom mass, $g = 9.81$ m/s^2 and λ is the lattice wavelength) the tunneling rate is suppressed by the tunneling energy and site detuning, scaling as $J^2/\sqrt{J^2 + \Delta^2}$ [75].

In an effort to add additional suppression, we employ a sideband spectroscopy cooling technique by applying off resonant clock light, detuned by the sideband frequency. After higher motional state atoms are excited to the upper $^3P_0$ clock state, we force them back to the ground state $^1S_0$ through the $^3D_1$ state decay (see Chapter 2). In this way, with repeated cycling, we force all atoms to the ground motional state, with the compromise of an extended clock cycle time (increased Dick noise). For a 100 E_r lattice we find the corresponding single-sided velocities in a vertical lattice configuration to be 8.2×10^{-15} m/s, 6.3×10^{-11} m/s, 1.6×10^{-7} m/s, and 2.53×10^{-5} m/s for $n = 0, 1, 2, 3$ respectively. This corresponds to a fractional frequency Doppler shift of 2.7×10^{-23}, 2.1×10^{-19}, 5.2×10^{-16}, and 8.4×10^{-14} respectively. For $n > 2$, tunneling will result in frequency shifts significantly detuned from our clock laser (assuming typical spectroscopy times) with negligible line-pulling. For $n = 2$ we find a special case where the doppler shift is comparable to the linewidth given by our spectroscopy times, potentially contributing the largest source of uncertainty from tunneling in our lattice. For $n < 2$, tunneling related shifts are contained to a level that is inconsequential for 10^{-18} clock operation.

As indicated above, key to containing tunneling related frequency shifts to below 1×10^{-18} is depopulating the $n = 2$ motional state. This requires sideband cooling an atomic sample to < 100 nK in a 100 E_r lattice, reducing the Boltzmann weighted line-pulling from $n = 2$ excited atoms to less than 1×10^{-18}. We note that this corresponds to a "worst case scenario" where atoms tunnel *only* in one direction. Likely tunneling takes place bi-directionally such that line pulling is at some level symmetric, resulting in a lower normalized atomic sample, with a "balanced" Doppler

shift. Taking a conservative estimate, (single-sided tunneling) we find the tunneling effect to be $\sim 5 \times 10^{-19}$ fractionally with a realistic clock cycle time for continuous clock operation in a 100 E_r lattice.

6.1.7 Doppler shift, 1st and 2nd order

The motion of atoms relative to the clock laser wavefront can result in a systematic Doppler shift in the clock frequency. Harmonic confinement provided by the optical lattice virtually eliminates this effect, with motion in the trap averaging to a zero net Doppler shift. Unfortunately, suppression of the Doppler effect degrades with any movement of the trap potential relative to the clock laser wavefront [133].

To faithfully transfer our stabilized clock light through a potentially noisy laboratory (optical fiber) environment, we implement a fiber noise cancelation scheme that works as follows: preceding the optical fiber in-coupler we place an optic that picks off a small amount of stable laser light. After the light has propagated through the optical fiber we designate a 'reference point' at which we wish to transfer our stabilized light. A fraction of the laser light is reflected from the reference point and sent, counter propagating, back through the optical fiber. The reflected light contains noise from the optical fiber environment which, when mixed with the stabilized light, forms a beat note that can be used to write opposing frequency corrections on the stabilized light to effectively cancel the noise from the optical fiber.

In our fiber noise cancelation system we use an acousto-optic modulator in the beam path after the stable light pickoff. This allows us to write frequency corrections on the laser light before entering the optical fiber with relatively high bandwidth, and to detect our error signal at twice the modulation frequency of 81 MHz. We mix the beat note error signal with a 162 MHz source that is referenced to a Hydrogen maser. This technique transfers the superb stability and spectral coherence of our stabilized clock light to the desired reference frame. Specifically, we aim to minimize any phase chirp (motion) between the atoms and clock light phase front therefore we

reference the lattice retro-reflecting optic that defines the standing wave. Monitoring the fiber noise cancellation signal to noise indicates a 99.9% fidelity in transferring the clock light to the rest frame of the lattice.

In order to quantify the remaining noise from a 0.1% uncertainty in π radian of reference phase, we consider the residual Doppler shift resulting from three oscillatory periods, τ, relative to our spectroscopy period, τ_s: $\tau > \tau_s$, $\tau < \tau_s$, and $\tau = \text{n} \times \tau_s$ (where n = 1,2,3...). For long Doppler oscillation periods, $\tau > \tau_s$, our clock frequency would appear sinusoidal in time, with a zero average Doppler shift.[1] For short Doppler periods, $\tau < \tau_s$, we find a behavior analogous to the atom in the trap potential, high frequency trap motion should average to zero, causing no net frequency shift. However, excess trap motion correlated with clock spectroscopy time could lead to a net nonzero Doppler shift during spectroscopy. If we assume the 0.1% uncertainty in π radian of reference phase translates to a constant linear phase chirp over the duration of a spectroscopy cycle, we can write the total phase as a function of time as

$$\phi(t) = \frac{\pi \times 10^{-3} \text{ rad}}{\tau_s} t + \phi_0 \tag{6.18}$$

where τ_s is the spectroscopy duration, and ϕ_0 is an arbitrary phase offset. Noting that the time derivative of the phase is the radian frequency, we find a fractional frequency shift of 6.4×10^{-19} for a spectroscopy time of 1500 ms. However, we suspect $> 99.9\%$ fidelity is realized with repeated clock cycles as our largest noise source in the phase lock stems from the incoupling lens to the fiber, located in a separate room on a active vibration isolation platform, mechanically decoupled from τ_s. In our current laboratory configuration a spectroscopy time of 1500 ms is achievable but atypical for robust clock operation. A simple interleaved clock measurement recording the frequency difference between two clocks with different delay times preceding a common τ_s would quantify this statistic below 1×10^{-18} for spectroscopy times < 1 s.

---

[1] A clock frequency output that is sinusoidal in time *would* degrade instability performance, see Chapter 3 for more details. We note that our measured Allan deviation is consistent with our optical lattice clock construction (see Figure 3.1, Figure 3.2) indicating the absence of long Doppler oscillation periods.

To test the robustness off the phase transfer process, we attach a piezoelectric (PZT) device to the retro-reflecting mirror that defines the lattice standing wave to induce vibrations up to 40 dB greater then that during normal clock operation. Figure 6.9 shows clock spectroscopy during a 40 Hz sine wave PZT modulation while referenced to lab frame (red dots) and referenced to the retro-reflecting lattice frame (blue dots). As expected, the harmonic motion of the trap potential relative to the phase of the clock laser light produces sidebands at the drive frequency. When referencing to the lattice retro-reflector while modulating the PZT we find no sideband presence, and experience no degradation of the phase lock, demonstrating faithful transfer to the atom frame (for noise frequencies near 40 Hz).
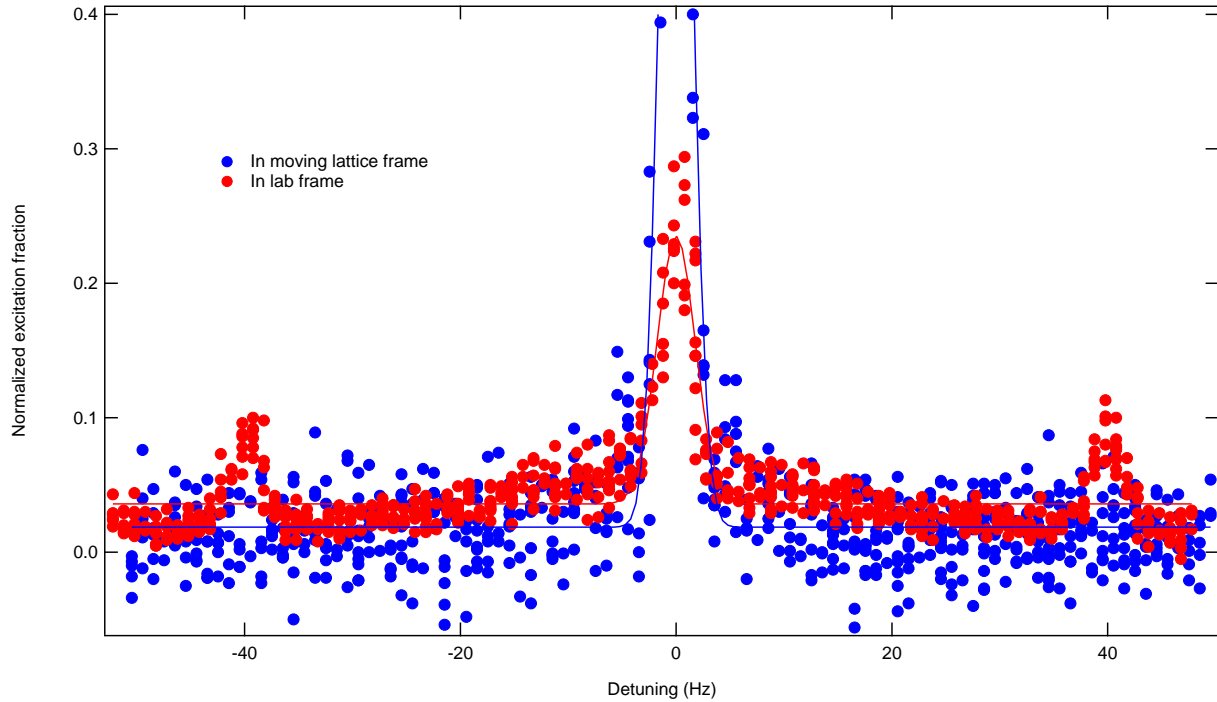

Figure 6.9: Spectroscopy on a trap potential oscillating with an amplitude 40 dB greater than normal clock vibrations. Image displays a frequency trance of the carrier when phase referencing clock laser to the atom frame (blue dots) and the lab frame (red dots).

Expanding the Doppler effect to second order we find a relativistic component with a frac-

tional frequency shift given by

$$\frac{\Delta \nu}{\nu_0} = \frac{1}{2} \frac{\langle v^2 \rangle}{c^2} \tag{6.19}$$

where $\langle v^2 \rangle$ is the time-averaged atomic velocity and c is the speed of light. Assuming a final green MOT temperature of $\sim 4 \ \mu$K with an RMS velocity of ~ 2.4 cm/s we find this effect to be $< 5 \times 10^{-21}$ fractionally.

6.1.8 Background gas

Analogous to the density shift discussed previously, background gas, predominantly hydrogen and ytterbium, can collide with our lattice trapped ytterbium atoms, perturbing the natural clock frequency [44]. However, these elements exhibit distinctly different behavior in a vacuum system, determined by their interaction with the vacuum enclosure. Hydrogen spends little time adhered to overall vacuum system, where ytterbium sticks readily to other metal surfaces. To experimentally characterize the background gas shift we independently study both hydrogen and ytterbium in two separate leveraged measurements.

As our atomic oven produces a large source of ytterbium, we measure the background gas frequency shift from ytterbium in an interleaved clock configuration: 1) a normal clock, operating with a shuttered atomic beam and 2) a clock with various atomic beam fluxes hitting the atoms. The interleaved atomic systems eliminates many systematic shifts via common mode rejection, however; we expect an additional blackbody radiation shift in our perturbed clock of $\sim 5 \times 10^{-18}$ [11]. By directly monitoring the florescence signal from the atomic beam, we can determine the ytterbium flux retaliative to normal operation. Shown in Figure 6.10 is the background gas shifts at different ytterbium flux, corrected for the blackbody radiation shift from the atomic oven tip. Our normal operation has a ytterbium background signal of < 1 mV, limiting this shift to $< 5 \times 10^{-19}$ fractionally with an uncertainty of 2×10^{-19}.

The different characteristics of hydrogen as background gas requires an alternative measurement procedure. To directly characterize the background hydrogen shift we run two clock systems

proven to be stable over the chosen duration of data collection. On our leveraged system we increase the hydrogen pressure up to a factor of ten above normal operating vacuum levels by heating a non-evaporable getter vacuum pump. Frequency shifts where record over a range of increased background gas pressures over several days for consent clock configurations. The vacuum pressure is monitored with a calibrated ion gauge and lattice lifetime decay pre- and post- frequency measurement. We observed a linear background gas fractional shift scaling of $1.76(0.18) \times 10^{-17}/\tau^{-1}$ for lattice decay constant τ in seconds (for τ from 0.1 to 2). Our normal background gas pressure of 1×10^{-9} Torr corresponds to a fractional shift of 8.9×10^{-18} with an uncertainty of 8.8×10^{-19}. Our treatment of this shift indicates vacuum pressures of $< 1 \times 10^{-9}$ Torr are likley required for routine operation at the 10^{-18} level. We note that vacuum pressures below 10^{-10} Torr in atomic systems are commonly achieved, however, in the presence of an atomic oven, this may require carful construction.

An alternative method for measuring background gas collisions exploits a ytterbium lattice lifetime measurement and knowledge of long-range van der Waals interactions from the $C_6 r^{-6}$ interaction [44]. Importantly, computing the *differential C_6* coefficient between ground and excited clock states, coupled with a lattice lifetime will give a measure of the background gas shift. Methods employing this approach find similar 10^{-19} level shifts from background gas collisions for a strontium optical lattice clock [89]. However, we note that the mechanism and nature of background gas collisions is still under investigation.

6.1.9   Servo error and line pulling

Our atomic servo is designed to lock to the exact center of the atomic response structure by probing both $\pm 1/2 m_F$ states using Rabi spectroscopy [73]. Any effect degrading this process will result in a systematic frequency shift in our recorded clock transition. The predominate servo error is a result of uncompensated linear drift in systematics or local oscillator during clock spectroscopy [98]. For drifting systematics, we implement an interrogation scheme where $\pm 1/2 m_F$ states are
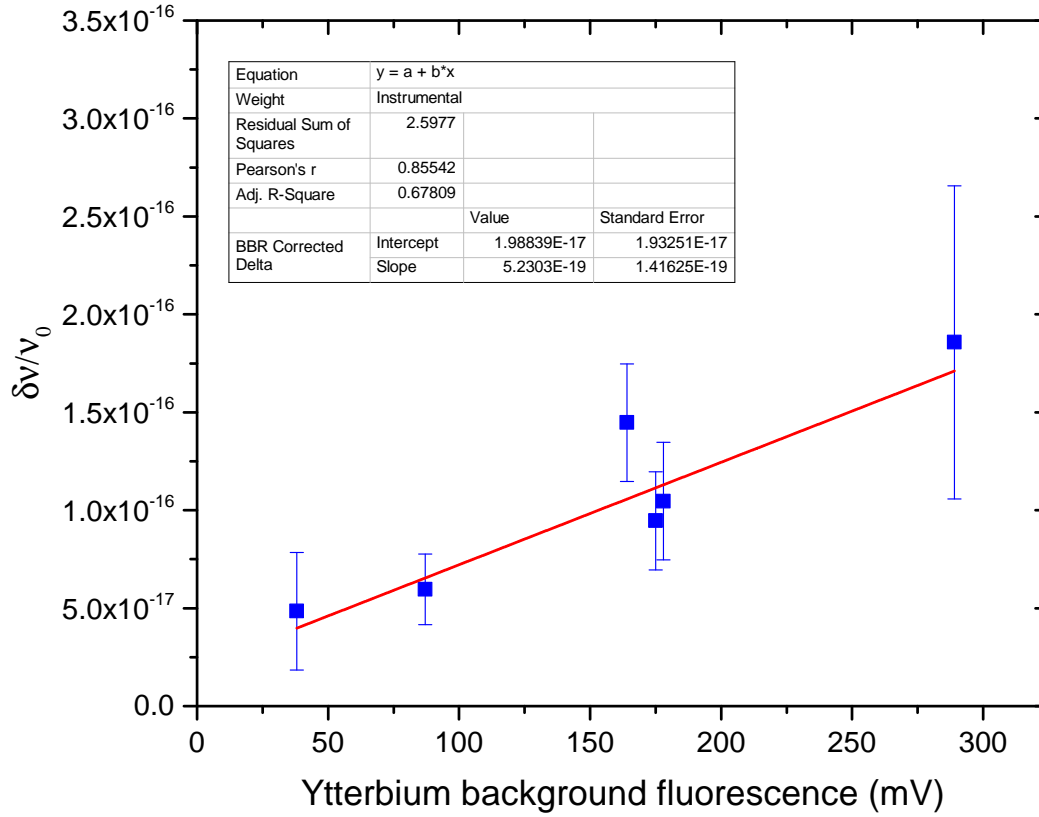
Figure 6.10: The measured fractional frequency shift from an atomic thermal beam in a ytterbium optical lattice clock.

probed in increasing frequency order followed by decreasing frequency order, averaging any linear drift. For uncompensated linear drift in the local oscillator we apply a second integrator servo to hold our first atomic servo near zero offset. Additionally, we used a micro controller updating a direct digital synthesizer to implement a feed forward drift calculation holding the second integrator drift to < 1 Hz over 2 hours, with a 24 hour drift of < 20 Hz. Our uncompensated servo error is consistent with zero with a one sigma error < 3 μHz for a for an averaging time of ~ 10000 s. Asymmetries in the Rabi line-shape are absent as well, provided we execute a well defined Rabi pulse

and our systematics are controlled over the spectroscopy period. We place a fractional uncertainty from servo errors at $< 1 \times 10^{-20}$.

Line pulling can result when any spectral features are unbalanced about the clock transition (i.e. $\sigma-$transitions, residual $\pi-$transitions, and motional state transitions). We suppress this effect by magnetically stretching, and optically pumping our atoms to the desired clock state before performing spectroscopy. To quantify residual line pulling effects, we generated a Rabi lineshape for 560 ms spectroscopy time and compute the frequency shift from σ and π transitions for a 1 G magnetic bias field as well as motional state sideband excitation. We find line pulling effects from the σ and π transitions are limited to $< 1 \times 10^{-22}$, provided we achieve 95% optical pumping efficiency, and 99% pure linear polarization of yellow light. The opposing π transition is responsible for nearly all of the calculated line pulling as it is closest in detuning and only suppressed by optical pumping (amplitude imbalance of 20:1). The line pulling from σ transitions is nearly zero because they enjoy four times larger sensitivity to the magnetic bias field compared to the π transitions and are further suppressed with linear polarization of clock light. Our ultra narrow band spectroscopy cleanly resolves the carrier transition between largely symmetric, longitudinal motional state frequencies of > 50 kHz and transverse frequencies > 50 Hz. Transverse frequency excitation is greatly suppressed, provided probe light propagation is perpendicular to the radial trap direction. Computing a worst case scenario shift from transverse motional frequencies at ± 50 Hz with an amplitude imbalance of 3:1, with no suppression from probe light alignment we find this effect is limited to $< 1 \times 10^{-19}$ fractionally.

6.1.10   AOM phase chirp

In our atomic system, we employ acoustic optic modulators (AOM)s to apply the necessary frequency corrections required for the atomic servo. Although AOMs can add a well defined RF frequency to an optical electromagnetic wave with high fidelity, phase chirps can result from inefficiency in this process, leading to a net frequency shift. Two distinct physical processes produce

phase chirps in an AOM; a ringing effect from a burst of RF entering the AOM crystal (microsecond timescales), and a thermal heating effect from absorption of RF power (second timescales) [32].

To implement full clock light frequency control for frequency locking and fiber noise cancellation, our atomic system uses separate sequential AOM devices, referred to here as AOM_{freq} and AOM_{noise}. Both AOMs are positioned before the optical distribution fibers, with AOM_{freq} preceding AOM_{noise}. In this configuration, we maintain constant RF power to the control frequency AOM device, eliminating the thermal phase chirp. The function of AOM_{noise} becomes two-fold: it servos noise out of the fiber system, and shutters the clock light on and off for spectroscopy. In this way, phase chirping effects should be eliminated, provided the servo bandwidth of our fiber noise cancellation system is adequate. During non-spectroscopy cycle times, a large servo offset can develop, leading to a nonzero phase chirp when engaging the servo to implement clock interrogation. To combat this problem, we feed a dummy RF signal to our fiber noise cancellation servo electronics, ensuring zero servo offset before spectroscopy. When AOM_{noise} is activated, symmetric phase excursions resulting from the servo activation can still occur about the servo point. By employing high bandwidth (~ 300 kHz) electronics, we ensure our servo attack excursions are held to < 10 μs, in the limited atomic sensitivity region of Rabi spectroscopy for interrogations times of 140 ms-1.5 s. Nonetheless, the possibility of a significant frequency shift warrants further investigation. To this end, we recorded the maximum induced phase chirp, and the time averaged phase deviation for several hundred spectroscopy interrogations. We numerically calculated the worst case servo attack phase chirp frequency shift for a Rabi spectroscopy time of 140 ms to be $< 3 \times 10^{-19}$ fractionally [40]. With the above implementations, we find the net phase chirp averages to zero with repeated clock cycles. Recording and averaging several hundred phase chirp excursions then repeating our numerical phase chirp calculations we find a systematic frequency shift consistent with zero with a one sigma fractional uncertainty of $< 3 \times 10^{-20}$.

6.1.11   Phase chirps from thermal effects

Any path taken by clock light that is uncompensated by active noise cancellation can lead to frequency errors in the atomic servo. By referencing the lattice retro reflector optic we achieve faithful transfer efficiency of our cavity stabilized light to the lattice frame. However, temperature changes in optical elements following the retro reflector can cause phase chirps in the clock light interrogating trapped atoms. To quantify this effect we consider a (large) linear temperature drift of 1 K/Hr in a 1 cm thick fused silica, the material used in our vacuum viewports. With a thermo-optic coefficient, $\frac{dn}{dT}$ (where n is the index of refraction), of $\sim 9.0 \times 10^{-6}$ at 300 K and a thermal expansion coefficient of $\sim 0.55 \times 10^{-6}$ we find an effective velocity between lattice trapped atoms and probe light wave front of $\sim 2.5 \times 10^{-12}$ m/s [79]. This results in a Doppler like shift of 8.3×10^{-21} fractionally, however, control of our environmental temperature better than 1 K/Hr is routine, therefore we report this uncertainty to be $< 3 \times 10^{-21}$. A similar calculation for laser propagation in air (thermo-optic coefficient of $\sim 1 \times 10^{-5}$ at standard pressure around 300 K) over a distance d = 15 cm yields a fractional shift of $\sim 1 \times 10^{-19}$ assuming a linear temperature drift of 1 K/Hr [52].

6.1.12   Local gravitational potential shift

One of the outcomes of Einstein's theory of relativity was the abandonment of an absolute time. A consequence of this paradigm is the gravitational redshift, where the frequency of electromagnetic radiation will be reduced in the presence of strong a gravitational potential relative to a weaker one. For example, the gravitational fractional frequency shift, referenced to a specific location on the Boulder NIST campus, is estimated to be -1798.7×10^{-16} with an uncertainty of $\pm 3 \times 10^{-17}$ from an ideal geoid surface at 'sea level' [95]. The geoid surface is defined with respect to an ideal mean-Earth ellipsoid in a tide free system, at the equipotential surface of Earth's gravity field matching the global mean sea level. The uncertainty in quantifying this definition limits

the realization of a second over large distances to $\sim 1 \times 10^{-17}$ [95]. As this value is an order of magnitude above our clock performance, our ability to quantify this effect is partitioned into two scenarios, distant and local clock comparisons.

For clock comparisons over large distances we start from the theory of general relativity assuming a stationary observer in the Schwarzschild metric. We find that the frequency of a photon in a gravitation potential, ν_0, relative to the frequency of a photon infinitely far away, ν_∞ (zero gravitational potential) to be:

$$\frac{\nu_\infty}{\nu_0} = \left(1 - \frac{2GM}{r_0 c^2}\right)^{1/2} \tag{6.20}$$

where G is the gravitational constant, M is the mass of the earth, r_0 is the radius of the mass, and c is the speed of light. With the binomial approximation we can write this equality as:

$$\frac{\nu_\infty}{\nu_0} \approx 1 - \frac{GM}{r_0 c^2} \cdots \tag{6.21}$$

Implying that it is necessary to determine the gravitational potential a clock is operating in for accurate computation of this frequency shift. For comparison of two clocks at different gravitational potentials we find:

$$\frac{\delta\nu}{\nu_0} = \frac{\Phi_1 - \Phi_2}{c^2}. \tag{6.22}$$

where one potential is (generally) defined relative to the geoid. Comparison of clocks with this technique will comprise of two errors: the definition of the geoid and the ability to measure local potential relative to the geoid. Absolute clock frequency comparison for fractional accuracies reaching 10^{-18} is limited, impart, by geoid potential at a few parts in 10^{-17}, further study is warranted and is still under investigation [38, 46].

For clocks in the same location (e.g. same laboratory) we find our relativistic uncertainty is limited by our ability to measure height differences between two lattice trapped atomic samples. Assuming variations in g are sufficiently small between measurements locations, we find the

fractional frequency shift close to the surface of the Earth to be

$$\frac{\delta\nu}{\nu_0} = \frac{g\Delta h}{c^2} \tag{6.23}$$

where g is the local acceleration due to gravity, Δh is the difference in height, and c is the speed of light. The gravitational shift at the Earth's surface ($g \approx 9.81$ m/s^2) has a fractional shift on the clock frequency of $\sim 1 \times 10^{-16}$ per meter of height [29]. Typical theodolite precision allows for 1 mm level relative accuracy between a height measurement spanning ~ 0.5 km distance, limiting this effect to $\sim 1 \times 10^{-19}$ fractionally.[2]   We note that absolute measurement of g by gravimeters at the 10^{-6} level is routine [42].

---

[2] A theodolite is an instrument used to measure hight differences between locations

6.2   Total systematic uncertainty of ^{171}Yb lattice clock

With the above discussion of possible systematic errors in ytterbium's clock frequency, we can tabulate a total clock uncertainty budget, shown in Table 6.2. Directly evident by the table 6.2 is at the Blackbody radiation shift and lattice light shifts continue to limit the performance of our optical lattice clock. However, it is encouraging that other shifts have been well characterized for 10^{-19} clock operation, indicating further efforts to reduced the Blackbody radiation shift and lattice light shifts are warranted. Potential next steps to reduced these limiting uncertainties could be implementing a cryogenic radiation shield, and continued lattice polarizability measurements further minimizing higher order lattice effects [127, 63]. Additionally, further study of lattice tunneling combined with sideband cooling could afford lower lattice depths greatly reducing our current sensitivity to lattice light shifts. We see no formidable obstacle to reducing total ^{171}Yb lattice clock uncertainty into the 10^{-19} fractional level.

Table 6.1: ^{171}Yb lattice clock uncertainty in fractional clock frequency operating at room temperature (~ 296.7 K) with atoms trapped in $\sim 1 \times 10^{-9}$ Torr vacuum.

Systematic Effect	$\times 10^{-18}$
Blackbody radiation	1.0
Lattice light shifts	1.1
First-order Zeeman effect	0.4
Second-order Zeeman effect	0.4
DC Stark shift	0.6
Background gas	0.9
Density shift	0.3
Probe light shift	0.4
Tunneling in lattice	0.5
First-order Doppler shift	0.6
Second-order Doppler shift	0.0
Servo error and line pulling	0.0
AOM phase chirp	0.0
Phase chirps from thermal effects	0.1
Total ytterbium clock uncertainty	2.1×10^{-18}

Chapter 7

Concluding remarks

The staggering advancement of optical based timekeepers in the last decade has been a direct consequence of unique class quantum systems studied through the perspective of high resolution spectroscopy. As recently as the mid-2000s to the time of this writing, optical clock measurement capability has experienced a full three orders of magnitude improvement, sitting on the cusp of 10^{-19} fractional performance [124, 21, 85, 57, 89]. Indeed the improvement of timekeepers has far outpaced need for such precise timing application in everyday life, reshaping what the word 'timekeeper' has come to define. The worldwide research undertaken on optical clocks, and the work detailed in this thesis, takes an important first step in providing an ultra sensitive probe to be used in studying and defining our surrounding world. Optical frequency standards will play a major role in studying the fundamental constants [15], Einstein's theory of relativity [29], physics beyond the Standard Model [43], quantum simulations [17], quantum computing, many-body physics [18], and more.

As for optical lattice clocks, such as the ytterbium system detailed in this thesis, the outlook remains encouraging. No major clock limitations exist to push fractional lattice clock uncertainties into the 10^{-19} decade. The absolute frequencies of Strontium-87 and Ytterbium-171 optical lattice clocks have been measured with fractional uncertainties of $\sim 1 \times 10^{-15}$. Additionally, many of these systems (including Mercury-199 at the time of this writing) possess fractional systematic uncertainties below 10^{-16} [89, 135]. This places frequency metrology in a rather awkward place where

frequency comparisons can be made far beyond the realized SI limit. Key to reaching systematic uncertainties past 10^{-18} is the reduction, control, and quantifying of systematics. Likely additional atomic system shielding (thermal, electrical, magnetic ect...) accompanied by an improved optical oscillator with reduced thermal noise will achieve these requirements, enabling 10^{-18} leveraged systematic measurements in 100 seconds or less. Even with the above improvements, the next two orders of magnitude in inaccuracy reduction will be exceedingly challenging.

To date, no single atomic species (Sr, Yb, Hg...) used in an optical lattice clock has proven advantageous for an 'ultimate' time keeper. At this stage, we are blessed to have such a plethora of quantum species capable of 10^{-18} or better measurement ability. In due time, with the limitation of our ability to control systematics, an ultimate optical frequency source will become evident, and likely be adopted to redefine the standard second. For now, optical standards are reported as 'secondary representations of the second', a symbolic 'first step' away from the microwave based definition [34, 45]. It is encouraging to witness the rapid improvement, and implementation of optical based frequency standards in laboratories around the world. However, the full benefit of an optical base timescale is still hindered by our ability to transfer time to different locations. As described in Chapter 6, accuracy of clocks in the presence of Earth's gravity will be limited by our ability to measure the gravitational potential and the current definition of the geoid. One solution for comparison between two remote locations is a transportable operating clock. However, this would require historical knowledge of the clock speed and geopotential trajectory [81]. Alternatively, a collection of well-characterized clocks operating in a low gravitational environment (such as orbits in space) could provide a second geoid with greatly reduced gravitational noise.

A network of optical clocks operating at the level of 10^{-18} offers a platform for tests of fundamental physics such as Einstein's theory of relativity, and physics beyond the Standard Model [113, 111, 28]. The backbone of general relativity is based on the equivalence principle. This idea holds for both velocity and position related effects (commonly referred to as local Lorentz invariance, and local position invariance). A network of optical clocks, such as the one presented in this thesis,

could be placed in orbits to directly study Lorentz invariance and position invariance. These relativity tests measure deviations from the predicted theory (either from velocity or position) by measuring relative or absolute redshift measurements. Other possibilities range from detection of gravitational waves, and potentially studying the nature of dark matter [3, 33].

One of the intriguing outcomes from the study of optical based timekeepers is the large number of different quantum oscillators that can be used as a clock timebase. The internal ticking rate of each quantum oscillator is unique and determined by the substructure of the oscillator. In this way, the study of quantum oscillator frequencies relative to one another offers a opportunity to explore subatomic particle interaction with nature (space, gravity, time, etc...) [107, 135]. These measurements are realized by selecting transitions in quantum oscillators that are sensitive to the desired study. For example, different optical clocks possess varying dependence on the fine structure constant, α [8]. Thus, a frequency ratio measurement between two clocks with different α dependence over a duration of time (years) can be used to quantify the rate of change in α. Together, these measurement possibilities make optical lattice clocks invaluable tools for interrogating the construction of the universe; as frequency continues to be, and will remain for the foreseeable future, the most precisely measurable quantity in nature.

As we look to the future, it is important to recall what made optical clocks so metrologically potent: An incredibly high frequency combined with an ultra-narrow transition. This powerful strategy is being continued in current work searching for the (illusive) nuclear clock transitions in Thorium-229, with proposed clock uncertainties reaching the 10^{-20} level [96, 26]. The advantage of a nuclear clock is twofold, with clock wavelengths potentially < 200 nm, nuclear clocks 'tick' fundamentally faster than conventional optical atomic clocks, and clock shifts are highly suppressed because the frequency time base is derived from a well isolated nucleus. A clock defined by an atomic nuclear transition would mark a new era in timekeeping, opening the door for metrology at a level unattainable by presently realized optical standards.

Bibliography

[1] Ansys version 13.0.0, steady-state thermal analysis.

[2] K. beloy, private communication (unpublished).

[3] BP Abbott, Richard Abbott, TD Abbott, MR Abernathy, Fausto Acernese, Kendall Ackley, Carl Adams, Thomas Adams, Paolo Addesso, RX Adhikari, et al. Observation of gravitational waves from a binary black hole merger. Physical review letters, 116(6):061102, 2016.

[4] Ali Al-Masoudi, Sören Dörscher, Sebastian Häfner, Uwe Sterr, and Christian Lisdat. Noise and instability of an optical lattice clock. Phys. Rev. A, 92:063814, Dec 2015.

[5] David W Allan. Statistics of atomic frequency standards. Proceedings of the IEEE, 54(2):221–230, 1966.

[6] Wolfgang Alt, Dominik Schrader, Stefan Kuhr, Martin Müller, Victor Gomer, and Dieter Meschede. Single atoms in a standing-wave dipole trap. Phys. Rev. A, 67:033403, Mar 2003.

[7] E. J. Angstmann, V. A. Dzuba, and V. V. Flambaum. Frequency shift of the cesium clock transition due to blackbody radiation. Phys. Rev. Lett., 97:040802, Jul 2006.

[8] EJ Angstmann, VA Dzuba, and VV Flambaum. Relativistic effects in two valence-electron atoms and ions and the search for variation of the fine-structure constant. Physical Review A, 70(1):014102, 2004.

[9] Z. W. Barber, J. E. Stalnaker, N. D. Lemke, N. Poli, C. W. Oates, T. M. Fortier, S. A. Diddams, L. Hollberg, C. W. Hoyt, A. V. Taichenachev, and V. I. Yudin. Optical lattice induced light shifts in an yb atomic clock. Phys. Rev. Lett., 100:103002, Mar 2008.

[10] James A Barnes. Atomic timekeeping and the statistics of precision signal generators. Proceedings of the IEEE, 54(2):207–220, 1966.

[11] K. Beloy, N. Hinkley, N. B. Phillips, J. A. Sherman, M. Schioppo, J. Lehman, A. Feldman, L. M. Hanssen, C. W. Oates, and A. D. Ludlow. Atomic clock with 1×10^{-18} room-temperature blackbody stark uncertainty. Phys. Rev. Lett., 113:260801, Dec 2014.

[12] K. Beloy, J. A. Sherman, N. D. Lemke, N. Hinkley, C. W. Oates, and A. D. Ludlow. Determination of the $5d6s\ ^3D_1$ state lifetime and blackbody-radiation clock shift in yb. Phys. Rev. A, 86:051404, Nov 2012.

[13] J. C. Bergquist, Wayne M. Itano, and D. J. Wineland. Recoilless optical absorption and doppler sidebands of a single trapped ion. Phys. Rev. A, 36:428–430, Jul 1987.

[14] Rainer Blatt and David Wineland. Entangled states of trapped atomic ions. Nature, 453(7198):1008–1015, 2008.

[15] S. Blatt, A. D. Ludlow, G. K. Campbell, J. W. Thomsen, T. Zelevinsky, M. M. Boyd, J. Ye, X. Baillard, M. Fouché, R. Le Targat, A. Brusch, P. Lemonde, M. Takamoto, F.-L. Hong, H. Katori, and V. V. Flambaum. New limits on coupling of fundamental constants to gravity using ^{87}Sr optical lattice clocks. Phys. Rev. Lett., 100:140801, Apr 2008.

[16] S. Blatt, J. W. Thomsen, G. K. Campbell, A. D. Ludlow, M. D. Swallows, M. J. Martin, M. M. Boyd, and J. Ye. Rabi spectroscopy and excitation inhomogeneity in a one-dimensional optical lattice clock. Phys. Rev. A, 80:052703, Nov 2009.

[17] Immanuel Bloch, Jean Dalibard, and Sylvain Nascimbène. Quantum simulations with ultracold quantum gases. Nature Physics, 8(4):267–276, 2012.

[18] Immanuel Bloch, Jean Dalibard, and Wilhelm Zwerger. Many-body physics with ultracold gases. Rev. Mod. Phys., 80:885–964, Jul 2008.

[19] J. Borregaard and A. S. Sørensen. Efficient atomic clocks operated with several atomic ensembles. Phys. Rev. Lett., 111:090802, Aug 2013.

[20] C. J. Bowers, D. Budker, E. D. Commins, D. DeMille, S. J. Freedman, A.-T. Nguyen, S.-Q. Shang, and M. Zolotorev. Experimental investigation of excited-state lifetimes in atomic ytterbium. Phys. Rev. A, 53:3103–3109, May 1996.

[21] Martin M. Boyd, Andrew D. Ludlow, Sebastian Blatt, Seth M. Foreman, Tetsuya Ido, Tanya Zelevinsky, and Jun Ye. ^{87}Sr lattice clock with inaccuracy below 10^{-15}. Phys. Rev. Lett., 98:083002, Feb 2007.

[22] Martin M. Boyd, Tanya Zelevinsky, Andrew D. Ludlow, Sebastian Blatt, Thomas Zanon-Willette, Seth M. Foreman, and Jun Ye. Nuclear spin effects in optical lattice clocks. Phys. Rev. A, 76:022510, Aug 2007.

[23] B.H. Bransden and C.J. Joachain. Physics of Atoms and Molecules. Pearson Education. Prentice Hall, 2003.

[24] D. Budker, D.F. Kimball, and D.P. DeMille. Atomic Physics: An Exploration Through Problems and Solutions. Oxford University Press, 2004.

[25] Milan Burša, Jan Kouba, Muneendra Kumar, Achim Müller, Karel Raděj, Scott A True, Viliam Vatrt, and Marie Vojtíšková. Geoidal geopotential and world height system. Studia Geophysica et Geodaetica, 43(4):327–337, 1999.

[26] C. J. Campbell, A. G. Radnaev, A. Kuzmich, V. A. Dzuba, V. V. Flambaum, and A. Derevianko. Single-ion nuclear clock for metrology at the 19th decimal place. Phys. Rev. Lett., 108:120802, Mar 2012.

[27] GK Campbell, MM Boyd, JW Thomsen, MJ Martin, S Blatt, MD Swallows, TL Nicholson, T Fortier, CW Oates, SA Diddams, et al. Probing interactions between ultracold fermions. science, 324(5925):360–363, 2009.

[28] Takeshi Chiba. The constancy of the constants of nature: updates. Progress of theoretical physics, 126(6):993–1019, 2011.

[29] Chin-Wen Chou, DB Hume, Till Rosenband, and DJ Wineland. Optical clocks and relativity. Science, 329(5999):1630–1633, 2010.

[30] Steven Chu. Nobel lecture: The manipulation of neutral particles. Rev. Mod. Phys., 70:685–706, Jul 1998.

[31] Garrett D Cole, Wei Zhang, Michael J Martin, Jun Ye, and Markus Aspelmeyer. Tenfold reduction of brownian noise in high-reflectivity optical coatings. Nature Photonics, 7(8):644–650, 2013.

[32] Carsten Degenhardt, Tatiana Nazarova, Christian Lisdat, Hardo Stoehr, Uwe Sterr, and Fritz Riehle. Influence of chirped excitation pulses in an optical clock with ultracold calcium atoms. IEEE transactions on instrumentation and measurement, 54(2):771–775, 2005.

[33] Andrei Derevianko. Detecting dark matter waves with precision measurement tools. arXiv preprint arXiv:1605.09717, 2016.

[34] Bureau International des Poids et Mesures. Report of the 19th meeting of consultative committee for time and frequency. Technical report, International Committee for Weights and Measures, September 2012.

[35] GJ Dick, JD Prestage, CA Greenhall, and L Maleki. Proceedings of the 22nd annual precise time and time interval (ptti) applications and planning meeting. 1990.

[36] R. H. Dicke. Coherence in spontaneous radiation processes. Phys. Rev., 93:99–110, Jan 1954.

[37] RWP Drever, John L Hall, FV Kowalski, J Hough, GM Ford, AJ Munley, and H Ward. Laser phase and frequency stabilization using an optical resonator. Applied Physics B, 31(2):97–105, 1983.

[38] S. Droste, F. Ozimek, Th. Udem, K. Predehl, T. W. Hänsch, H. Schnatz, G. Grosche, and R. Holzwarth. Optical-frequency transfer over a single-span 1840 km fiber link. Phys. Rev. Lett., 111:110801, Sep 2013.

[39] V A Dzuba and A Derevianko. Dynamic polarizabilities and related properties of clock states of the ytterbium atom. Journal of Physics B: Atomic, Molecular and Optical Physics, 43(7):074011, 2010.

[40] S. Falke, M. Misera, U. Sterr, and C. Lisdat. Delivering pulsed and phase stable light to atoms of an optical clock. Applied Physics B, 107(2):301–311, 2012.

[41] Stephan Falke, Nathan Lemke, Christian Grebing, Burghard Lipphardt, Stefan Weyers, Vladislav Gerginov, Nils Huntemann, Christian Hagemann, Ali Al-Masoudi, Sebastian Hfner, Stefan Vogt, Uwe Sterr, and Christian Lisdat. A strontium lattice clock with 3 10 17 inaccuracy and its frequency. New Journal of Physics, 16(7):073023, 2014.

[42] James E Faller. The measurement of little g: a fertile ground for precision measurement science. Journal of Research of the National Institute of Standards and Technology, 110(6):559, 2005.

[43] Harald Fritzsch and Joan Sol. Matter non-conservation in the universe and dynamical dark energy. Classical and Quantum Gravity, 29(21):215002, 2012.

[44] Kurt Gibble. Scattering of cold-atom coherences by hot atoms: Frequency shifts from background-gas collisions. Phys. Rev. Lett., 110:180802, May 2013.

[45] Patrick Gill. When should we change the definition of the second? Philosophical Transactions of the Royal Society of London A: Mathematical, Physical and Engineering Sciences, 369(1953):4109–4130, 2011.

[46] Fabrizio R Giorgetta, William C Swann, Laura C Sinclair, Esther Baumann, Ian Coddington, and Nathan R Newbury. Optical two-way time and frequency transfer over free space. Nature Photonics, 7(6):434–438, 2013.

[47] D.J. Griffiths. Introduction to Electrodynamics. Prentice Hall, 1999.

[48] R Grimm and Y B Ovchinnikov. Optical dipole traps for neutral atoms. 2000.

[49] H. Hachisu, K. Miyagishi, S. G. Porsev, A. Derevianko, V. D. Ovsiannikov, V. G. Pal'chikov, M. Takamoto, and H. Katori. Trapping of neutral mercury atoms and prospects for optical lattice clocks. Phys. Rev. Lett., 100:053001, Feb 2008.

[50] Sebastian Hafner, Stephan Falke, Christian Grebing, Stefan Vogt, Thomas Legero, Mikko Merimaa, Christian Lisdat, and Uwe Sterr. $8{\times}10^{-17}$ fractional laser frequency instability with a long room-temperature cavity. Optics letters, 40(9):2112–2115, 2015.

[51] J. L. Hall, L. Hollberg, T. Baer, and H.G. Robinson. Optical heterodyne saturation spectroscopy. Applied Physics Letters, 39(9):680–682, 1981.

[52] W.M. Haynes. CRC Handbook of Chemistry and Physics, 91st Edition. Taylor & Francis, 2010.

[53] Thomas P Heavner, Elizabeth A Donley, Filippo Levi, Giovanni Costanzo, Thomas E Parker, Jon H Shirley, Neil Ashby, Stephan Barlow, and S R Jefferts. First accuracy evaluation of nist-f2. Metrologia, 51(3):174, 2014.

[54] E. Hecht. Optics. Addison-Wesley, 2002.

[55] N Hinkley, JA Sherman, NB Phillips, M Schioppo, ND Lemke, K Beloy, M Pizzocaro, CW Oates, and AD Ludlow. An atomic clock with 10–18 instability. Science, 341(6151):1215–1218, 2013.

[56] P. Horowitz and W. Hill. The Art of Electronics. Cambridge University Press, 2015.

[57] N. Huntemann, C. Sanner, B. Lipphardt, Chr. Tamm, and E. Peik. Single-ion atomic clock with 3×10^{-18} systematic uncertainty. Phys. Rev. Lett., 116:063001, Feb 2016.

[58] LR Hunter, D Krause, KE Miller, DJ Berkeland, and MG Boshier. Precise measurement of the stark shift of the cesium d1 line. Optics communications, 94(4):210–214, 1992.

[59] W. M. Itano, J. C. Bergquist, J. J. Bollinger, J. M. Gilligan, D. J. Heinzen, F. L. Moore, M. G. Raizen, and D. J. Wineland. Quantum projection noise: Population fluctuations in two-level systems. Phys. Rev. A, 47:3554–3570, May 1993.

[60] S. R. Jefferts, T. P. Heavner, T. E. Parker, J. H. Shirley, E. A. Donley, N. Ashby, F. Levi, D. Calonico, and G. A. Costanzo. High-accuracy measurement of the blackbody radiation frequency shift of the ground-state hyperfine transition in ^{133}Cs. Phys. Rev. Lett., 112:050801, Feb 2014.

[61] YY Jiang, AD Ludlow, ND Lemke, RW Fox, JA Sherman, L-S Ma, and CW Oates. Making optical atomic clocks more stable with 10-16-level laser stabilization. Nature Photonics, 5(3):158–161, 2011.

[62] YY Jiang, AD Ludlow, ND Lemke, RW Fox, JA Sherman, L-S Ma, and CW Oates. Making optical atomic clocks more stable with 10-16-level laser stabilization. Nature Photonics, 5(3):158–161, 2011.

[63] Hidetoshi Katori, V. D. Ovsiannikov, S. I. Marmo, and V. G. Palchikov. Strategies for reducing the light shift in atomic clocks. Phys. Rev. A, 91:052503, May 2015.

[64] Hidetoshi Katori, Masao Takamoto, V. G. Pal'chikov, and V. D. Ovsiannikov. Ultrastable optical clock with neutral atoms in an engineered light shift trap. Phys. Rev. Lett., 91:173005, Oct 2003.

[65] T Kessler, C Hagemann, C Grebing, T Legero, U Sterr, F Riehle, MJ Martin, L Chen, and J Ye. A sub-40-mhz-linewidth laser based on a silicon single-crystal optical cavity. Nature Photonics, 6(10):687–692, 2012.

[66] Daniel Kleppner. Time too good to be true. Physics Today, 59(3):10, 2006.

[67] R. Kohlhaas, A. Bertoldi, E. Cantin, A. Aspect, A. Landragin, and P. Bouyer. Phase locking a clock oscillator to a coherent atomic ensemble. Phys. Rev. X, 5:021011, Apr 2015.

[68] R Le Targat, L Lorini, Y Le Coq, M Zawada, J Guéna, M Abgrall, M Gurov, P Rosenbusch, DG Rovera, B Nagórny, et al. Experimental realization of an optical second with strontium lattice clocks. Nature communications, 4, 2013.

[69] Rodolphe Le Targat, Xavier Baillard, Mathilde Fouché, Anders Brusch, Olivier Tcherbakoff, Giovanni D. Rovera, and Pierre Lemonde. Accurate optical lattice clock with ^{87}Sr atoms. Phys. Rev. Lett., 97:130801, Sep 2006.

[70] John H. Lehman, Katherine E. Hurst, Antonije M. Radojevic, Anne C. Dillon, and Jr. Richard M. Osgood. Multiwall carbon nanotube absorber on a thin-film lithium niobate pyroelectric detector. Opt. Lett., 32(7):772–774, Apr 2007.

[71] John H Lehman, Mauricio Terrones, Elisabeth Mansfield, Katherine E Hurst, and Vincent Meunier. Evaluating the characteristics of multiwall carbon nanotubes. Carbon, 49(8):2581–2602, 2011.

[72] D. Leibfried, R. Blatt, C. Monroe, and D. Wineland. Quantum dynamics of single trapped ions. Rev. Mod. Phys., 75:281–324, Mar 2003.

[73] N. D. Lemke, A. D. Ludlow, Z. W. Barber, T. M. Fortier, S. A. Diddams, Y. Jiang, S. R. Jefferts, T. P. Heavner, T. E. Parker, and C. W. Oates. Spin-1/2 optical lattice clock. Phys. Rev. Lett., 103:063001, Aug 2009.

[74] N. D. Lemke, J. von Stecher, J. A. Sherman, A. M. Rey, C. W. Oates, and A. D. Ludlow. p-wave cold collisions in an optical lattice clock. Phys. Rev. Lett., 107:103902, Aug 2011.

[75] Nathan D Lemke. Optical lattice clock with spin-1/2 ytterbium atoms. 2012.

[76] Pierre Lemonde and Peter Wolf. Optical lattice clock with atoms confined in a shallow trap. Phys. Rev. A, 72:033409, Sep 2005.

[77] Judah Levine. Introduction to time and frequency metrology. Review of scientific instruments, 70(6):2567–2596, 1999.

[78] Judah Levine. Invited review article: The statistical modeling of atomic clocks and the design of time scales. Review of Scientific Instruments, 83(2):021101, 2012.

[79] Douglas B Leviton and Bradley J Frey. Temperature-dependent absolute refractive index measurements of synthetic fused silica. In SPIE Astronomical Telescopes+ Instrumentation, pages 62732K–62732K. International Society for Optics and Photonics, 2006.

[80] Jérôme Lodewyck, Michal Zawada, Luca Lorini, Mikhail Gurov, and Pierre Lemonde. Observation and cancellation of a perturbing dc stark shift in strontium optical lattice clocks. Ultrasonics, Ferroelectrics, and Frequency Control, IEEE Transactions on, 59(3):411–415, 2012.

[81] Andrew D. Ludlow, Martin M. Boyd, Jun Ye, E. Peik, and P. O. Schmidt. Optical atomic clocks. Rev. Mod. Phys., 87:637–701, Jun 2015.

[82] Andrew D. Ludlow, Martin M. Boyd, Tanya Zelevinsky, Seth M. Foreman, Sebastian Blatt, Mark Notcutt, Tetsuya Ido, and Jun Ye. Systematic study of the ^{87}Sr clock transition in an optical lattice. Phys. Rev. Lett., 96:033003, Jan 2006.

[83] Andrew D Ludlow, T Zelevinsky, GK Campbell, S Blatt, MM Boyd, Marcio HG de Miranda, MJ Martin, JW Thomsen, Seth M Foreman, Jun Ye, et al. Sr lattice clock at $1 \times 10{-}16$ fractional uncertainty by remote optical evaluation with a ca clock. Science, 319(5871):1805–1808, 2008.

[84] Alan A. Madej, Pierre Dubé, Zichao Zhou, John E. Bernard, and Marina Gertsvolf. $^{88}Sr^+$ 445-thz single-ion reference at the 10^{-17} level via control and cancellation of systematic uncertainties and its measurement against the si second. Phys. Rev. Lett., 109:203002, Nov 2012.

[85] HS Margolis, GP Barwood, G Huang, HA Klein, SN Lea, K Szymaniec, and P Gill. Hertz-level measurement of the optical clock frequency in a single 88sr+ ion. Science, 306(5700):1355–1358, 2004.

[86] H.J. Metcalf and P. van der Straten. Laser Cooling and Trapping. Graduate Texts in Contemporary Physics. Springer New York, 2001.

[87] Thomas Middelmann, Stephan Falke, Christian Lisdat, and Uwe Sterr. High accuracy correction of blackbody radiation shift in an optical lattice clock. Phys. Rev. Lett., 109:263004, Dec 2012.

[88] T. L. Nicholson, M. J. Martin, J. R. Williams, B. J. Bloom, M. Bishof, M. D. Swallows, S. L. Campbell, and J. Ye. Comparison of two independent sr optical clocks with 1×10^{-17} stability at 10^3 s. Phys. Rev. Lett., 109:230801, Dec 2012.

[89] TL Nicholson, SL Campbell, RB Hutson, GE Marti, BJ Bloom, RL McNally, W Zhang, MD Barrett, MS Safronova, GF Strouse, et al. Systematic evaluation of an atomic clock at 2×10^{-18} total uncertainty. Nature communications, 6, 2015.

[90] Kenji Numata, Amy Kemery, and Jordan Camp. Thermal-noise limit in the frequency stabilization of lasers with rigid cavities. Phys. Rev. Lett., 93:250602, Dec 2004.

[91] International Bureau of Weights, Measures, Barry N Taylor, and Ambler Thompson. The international system of units (si). 2001.

[92] L. Olschewski. Determination of the nuclear magnetic moments on free ^{43}ca-, ^{87}sr-, ^{135}ba-, ^{137}ba-, ^{171}yb-, and ^{173}yb-atoms by means of optical pumping. Z. Phys. 249: No. 3, 205-27(1972)., Jan 1972.

[93] W. H. Oskay, S. A. Diddams, E. A. Donley, T. M. Fortier, T. P. Heavner, L. Hollberg, W. M. Itano, S. R. Jefferts, M. J. Delaney, K. Kim, F. Levi, T. E. Parker, and J. C. Bergquist. Single-atom optical clock with high accuracy. Phys. Rev. Lett., 97:020801, Jul 2006.

[94] V. D. Ovsiannikov, V. G. Pal'chikov, A. V. Taichenachev, V. I. Yudin, and Hidetoshi Katori. Multipole, nonlinear, and anharmonic uncertainties of clocks of sr atoms in an optical lattice. Phys. Rev. A, 88:013405, Jul 2013.

[95] Nikolaos K Pavlis and Marc A Weiss. The relativistic redshift with $3\times$ 10- 17 uncertainty at nist, boulder, colorado, usa. Metrologia, 40(2):66, 2003.

[96] E. Peik and Chr. Tamm. Nuclear laser spectroscopy of the 3.5 ev transition in th-229. EPL (Europhysics Letters), 61(2):181, 2003.

[97] William D. Phillips. Nobel lecture: Laser cooling and trapping of neutral atoms. Rev. Mod. Phys., 70:721–741, Jul 1998.

[98] N. Poli, Z. W. Barber, N. D. Lemke, C. W. Oates, L. S. Ma, J. E. Stalnaker, T. M. Fortier, S. A. Diddams, L. Hollberg, J. C. Bergquist, A. Brusch, S. Jefferts, T. Heavner, and T. Parker. Frequency evaluation of the doubly forbidden $^1S_0 \rightarrow ^3P_0$ transition in bosonic ^{174}Yb. Phys. Rev. A, 77:050501, May 2008.

[99] S. G. Porsev, Andrew D. Ludlow, Martin M. Boyd, and Jun Ye. Determination of sr properties for a high-accuracy optical clock. Phys. Rev. A, 78:032508, Sep 2008.

[100] S. G. Porsev, Yu. G. Rakhlina, and M. G. Kozlov. Electric-dipole amplitudes, lifetimes, and polarizabilities of the low-lying levels of atomic ytterbium. Phys. Rev. A, 60:2781–2785, Oct 1999.

[101] Sergey G. Porsev and Andrei Derevianko. Hyperfine quenching of the metastable $^3p_{0,2}$ states in divalent atoms. Phys. Rev. A, 69:042506, Apr 2004.

[102] Sergey G. Porsev and Andrei Derevianko. Multipolar theory of blackbody radiation shift of atomic energy levels and its implications for optical lattice clocks. Phys. Rev. A, 74:020502, Aug 2006.

[103] Sergey G. Porsev, Andrei Derevianko, and E. N. Fortson. Possibility of an optical clock using the $6^1S_0 \rightarrow 6^3P_0^o$ transition in ^{171,173}Yb atoms held in an optical lattice. Phys. Rev. A, 69:021403, Feb 2004.

[104] E. L. Raab, M. Prentiss, Alex Cable, Steven Chu, and D. E. Pritchard. Trapping of neutral sodium atoms with radiation pressure. Phys. Rev. Lett., 59:2631–2634, Dec 1987.

[105] W.J. Riley. Handbook of frequency stability analysis. 2008.

[106] M. V. Romalis and E. N. Fortson. Zeeman frequency shifts in an optical dipole trap used to search for an electric-dipole moment. Phys. Rev. A, 59:4547–4558, Jun 1999.

[107] T. Rosenband, D. B. Hume, P. O. Schmidt, C. W. Chou, A. Brusch, L. Lorini, W. H. Oskay, R. E. Drullinger, T. M. Fortier, J. E. Stalnaker, S. A. Diddams, W. C. Swann, N. R. Newbury, W. M. Itano, D. J. Wineland, and J. C. Bergquist. Frequency ratio of al+ and hg+ single-ion optical clocks; metrology at the 17th decimal place. Science, 319(5871):1808–1812, 2008.

[108] M. S. Safronova, S. G. Porsev, and Charles W. Clark. Ytterbium in quantum gases and atomic clocks: van der waals interactions and blackbody shifts. Phys. Rev. Lett., 109:230802, Dec 2012.

[109] Giorgio Santarelli, Claude Audoin, Ala' Makdissi, Philippe Laurent, G John Dick, and André Clairon. Frequency stability degradation of an oscillator slaved to a periodically interrogated atomic resonator. Ultrasonics, Ferroelectrics, and Frequency Control, IEEE Transactions on, 45(4):887–894, 1998.

[110] A. L. Schawlow and C. H. Townes. Infrared and optical masers. Phys. Rev., 112:1940–1949, Dec 1958.

[111] S Schiller, A Görlitz, A Nevsky, JCJ Koelemeij, A Wicht, P Gill, HA Klein, HS Margolis, Gaetano Mileti, U Sterr, et al. Optical clocks in space. Nuclear Physics B-Proceedings Supplements, 166:300–302, 2007.

[112] S. Schiller, A. Grlitz, A. Nevsky, J.C.J. Koelemeij, A. Wicht, P. Gill, H.A. Klein, H.S. Margolis, G. Mileti, U. Sterr, F. Riehle, E. Peik, Chr. Tamm, W. Ertmer, E. Rasel, V. Klein, C. Salomon, G.M. Tino, P. Lemonde, R. Holzwarth, and T.W. Hnsch. Optical clocks in space. Nuclear Physics B - Proceedings Supplements, 166:300 – 302, 2007. Proceedings of the Third International Conference on Particle and Fundamental Physics in SpaceProceedings of the Third International Conference on Particle and Fundamental Physics in Space.

[113] S Schiller, GM Tino, P Gill, C Salomon, U Sterr, E Peik, A Nevsky, A Görlitz, D Svehla, G Ferrari, et al. Einstein gravity explorer–a medium-class fundamental physics mission. Experimental astronomy, 23(2):573–610, 2009.

[114] M Schioppo, RC Brown, WF McGrew, N Hinkley, RJ Fasano, K Beloy, TH Yoon, G Milani, D Nicolodi, JA Sherman, et al. Ultra-stable optical clock with two cold-atom ensembles. arXiv preprint arXiv:1607.06867, 2016.

[115] Monika H. Schleier-Smith, Ian D. Leroux, and Vladan Vuletić. States of an ensemble of two-level atoms with reduced quantum uncertainty. Phys. Rev. Lett., 104:073604, Feb 2010.

[116] R. Shankar. Principles of Quantum Mechanics. Springer US, 2012.

[117] Jon H. Shirley. Modulation transfer processes in optical heterodyne saturation spectroscopy. Opt. Lett., 7(11):537–539, Nov 1982.

[118] A.E. Siegman. Lasers. University Science Books, 1986.

[119] D. Sobel. Longitude: The True Story of a Lone Genius Who Solved the Greatest Scientific Problem of His Time. Bloomsbury Publishing, 2010.

[120] Benjamin K. Stuhl, Brian C. Sawyer, Dajun Wang, and Jun Ye. Magneto-optical trap for polar molecules. Phys. Rev. Lett., 101:243002, Dec 2008.

[121] Matthew D Swallows, Michael Bishof, Yige Lin, Sebastian Blatt, Michael J Martin, Ana Maria Rey, and Jun Ye. Suppression of collisional shifts in a strongly interacting lattice clock. science, 331(6020):1043–1046, 2011.

[122] A. V. Taichenachev, V. I. Yudin, V. D. Ovsiannikov, V. G. Pal'chikov, and C. W. Oates. Frequency shifts in an optical lattice clock due to magnetic-dipole and electric-quadrupole transitions. Phys. Rev. Lett., 101:193601, Nov 2008.

[123] Masao Takamoto, Feng-Lei Hong, Ryoichi Higashi, Yasuhisa Fujii, Michito Imae, and Hidetoshi Katori. Improved frequency measurement of a one-dimensional optical lattice clock with a spin-polarized fermionic 87sr isotope. Journal of the Physical Society of Japan, 75(10):104302, 2006.

[124] Masao Takamoto, Feng-Lei Hong, Ryoichi Higashi, and Hidetoshi Katori. An optical lattice clock. Nature, 435(7040):321–324, 2005.

[125] Masao Takamoto and Hidetoshi Katori. Spectroscopy of the s 0 1- p 0 3 clock transition of s r 87 in an optical lattice. Physical review letters, 91(22):223001, 2003.

[126] Masao Takamoto, Tetsushi Takano, and Hidetoshi Katori. Frequency comparison of optical lattice clocks beyond the dick limit. Nature Photonics, 5(5):288–292, 2011.

[127] Ichiro Ushijima, Masao Takamoto, Manoj Das, Takuya Ohkubo, and Hidetoshi Katori. Cryogenic optical lattice clocks. Nature Photonics, 9(3):185–189, 2015.

[128] R. F. C. Vessot, M. W. Levine, E. M. Mattison, E. L. Blomberg, T. E. Hoffman, G. U. Nystrom, B. F. Farrel, R. Decher, P. B. Eby, C. R. Baugher, J. W. Watts, D. L. Teuber, and F. D. Wills. Test of relativistic gravitation with a space-borne hydrogen maser. Phys. Rev. Lett., 45:2081–2084, Dec 1980.

[129] S. A. Webster, M. Oxborrow, and P. Gill. Vibration insensitive optical cavity. Phys. Rev. A, 75:011801, Jan 2007.

[130] S. A. Webster, M. Oxborrow, S. Pugla, J. Millo, and P. Gill. Thermal-noise-limited optical cavity. Phys. Rev. A, 77:033847, Mar 2008.

[131] P. G. Westergaard, J. Lodewyck, L. Lorini, A. Lecallier, E. A. Burt, M. Zawada, J. Millo, and P. Lemonde. Lattice-induced frequency shifts in sr optical lattice clocks at the 10^{-17} level. Phys. Rev. Lett., 106:210801, May 2011.

[132] Philip G Westergaard, Jerome Lodewyck, and Pierre Lemonde. Minimizing the dick effect in an optical lattice clock. Ultrasonics, Ferroelectrics, and Frequency Control, IEEE Transactions on, 57(3):623–628, 2010.

[133] Guido Wilpers, CW Oates, Scott A Diddams, Albrecht Bartels, Tara M Fortier, WH Oskay, James C Bergquist, SR Jefferts, TP Heavner, TE Parker, et al. Absolute frequency measurement of the neutral 40ca optical frequency standard at 657 nm based on microkelvin atoms. Metrologia, 44(2):146, 2007.

[134] D. J. Wineland and Wayne M. Itano. Laser cooling of atoms. Phys. Rev. A, 20:1521–1540, Oct 1979.

[135] Kazuhiro Yamanaka, Noriaki Ohmae, Ichiro Ushijima, Masao Takamoto, and Hidetoshi Katori. Frequency ratio of ^{199}Hg and ^{87}Sr optical lattice clocks beyond the si limit. Phys. Rev. Lett., 114:230801, Jun 2015.

[136] Ralchenko Yu, AE Kramida, and J Reader. Nist atomic spectra database (ver. 4.1. 0). National Institute of Standards and Technology, Gaithersburg, MD (Available at http://physics. nist. gov/asd3), 2011.

[137] AM Zolot, FR Giorgetta, E Baumann, JW Nicholson, WC Swann, I Coddington, and NR Newbury. Direct-comb molecular spectroscopy with accurate, resolved comb teeth over 43 thz. Optics letters, 37(4):638–640, 2012.